Internal Report
DESY F15-90-01
July 1990

$\omega\omega$ and $\rho^-\rho^-$ Production in Two Photon Interactions at ARGUS

by

G. Tsipolitis

$\omega\omega$ and $\rho^+\rho^-$ Production in Two Photon Interactions at ARGUS

G. Tsipolitis

Physics Department,
McGill University, Montreal

$\omega\omega$ and $\rho^+\rho^-$ Production in Two Photon Interactions at ARGUS

George Tsipolitis

A Thesis submitted to the Faculty
of Graduate Studies and Research
in partial fulfillment of the requirements
for the Degree of Doctor of Philosophy

Physics Department
McGill University, Montreal

στους γονείς μου

Abstract

The reactions $\gamma\gamma \to 2\pi^+2\pi^-2\pi^0$ and $\gamma\gamma \to \pi^+\pi^-\pi^0\pi^0$ have been studied by using the ARGUS detector at the e^+e^- storage ring DORIS II at DESY.

In the $2\pi^+2\pi^-2\pi^0$ final state the production of ω-mesons is observed and in particular the reaction $\gamma\gamma \to \omega\omega$ is seen for the first time. The cross section for $\gamma\gamma \to \omega\omega$ is found to have an enhancement at $\sim 1.9\text{GeV}/c^2$ of about 12 nb. The topological cross sections for the reactions $\gamma\gamma \to 2\pi^+2\pi^-2\pi^0$ and $\gamma\gamma \to \omega\pi^+\pi^-\pi^0$ are also measured.

The production of charged ρ-mesons is observed in the $\pi^+\pi^-\pi^0\pi^0$ final state. The cross section for the reaction $\gamma\gamma \to \rho^+\rho^-$ is measured for the first time. The cross section did not show a threshold enhancement similar to that found in the reaction $\gamma\gamma \to \rho^0\rho^0$ and is about a factor of four smaller. A spin parity analysis of the $\rho^+\rho^-$ system shows that the cross section is dominated by the two amplitudes $J^P = 0^+$ and $J^P = 2^+$ with helicity 2.

Résumé

Les réactions $\gamma\gamma \to 2\pi^+2\pi^-2\pi^0$ et $\gamma\gamma \to \pi^+\pi^-\pi^0\pi^0$ ont été étudiées à l'anneau de stockage e^+e^- DORIS II à DESY grâce au détecteur ARGUS.

La production de mésons ω dans l'état final $2\pi^+2\pi^-2\pi^0$ a été mesurée et, en particulier, la réaction $\gamma\gamma \to \omega\omega$ a été observée pour la première fois.

Une augmentation subite d'environ 12 nb de la section efficace pour $\gamma\gamma \to \omega\omega$ a été observée à une énergie ~ 1.9 GeV/c^2. Les sections efficaces topologiques pour les réactions $\gamma\gamma \to 2\pi^+2\pi^-2\pi^0$ et $\gamma\gamma \to \omega\pi^+\pi^-\pi^0$ ont été aussi mesurées.

La production de mésons ρ chargés a été observée dans l'état final $\pi^+\pi^-\pi^0\pi^0$. La section efficace de la réaction $\gamma\gamma \to \rho^+\rho^-$ a été mesurée pour la première fois. Celle-ci ne montre pas la même augmentation au seuil de production et est 4 fois plus petite que la section efficace de la réaction $\gamma\gamma \to \rho^0\rho^0$. Une analyse de spin-parité a montré que la section efficace est dominée par les deux amplitudes $J^P = 0^+$ et $J^P = 2^+$ avec hélicité 2.

Acknowledgements

None of this work would have been possible without the combined effort of the ARGUS collaboration whose members are listed in Appendix D. Thanks to everybody.

I would especially like to thank my thesis advisor, P. M. Patel for his constant support and fruitful discussions. Ken Mclean, Alf Nilsson and Hermann Kolanoski deserve thanks for the many helpful discussions on two photon physics. I am grateful to D. B. MacFarlane who gave me the opportunity to work on the μ-VDC project which I enjoyed a lot, to Paul Mercure for his help on the McGill VAX and to Dave Gilkinson for his useful tips when I was installing KAL on the McGill VAX. It was a pleasure to work with all the graduate students, post-docs and professors of the Canadian subgroup of ARGUS. Finally, I would like to thank my parents and my sister Domna for their support and encouragement over all these years.

Preface

One of the fundamental philosophical questions is "*what are the constituents of the matter that surrounds us ?*" The first ideas about these fundamental constituents were stated almost 2500 years ago when the Greek philosopher Democritos postulated that matter was constructed from atoms ($\dot{\alpha}\tau o\mu o$ = indivisible). In our days this question is faced by High Energy Physicists. According to the current understanding, matter is built from two types of fundamental fermions, called quarks and leptons, which are assumed to be structureless.

The quarks exist in three colours (Red, Green and Blue) and transform as SU(3) triplets. They are bound together by the strong interactions and they form particles which are called hadrons. The observed spectrum of hadrons postulates that only states which are colour singlets are physically permitted. By combining a quark and an anti-quark one can get the singlet states which are called mesons and by combining three quarks the baryons. These are the only states that have been observed unambiguously in nature.

However, colour singlet states are also conceivable by combining for example two quarks and two anti-quarks or two quarks with a gluon (the carrier of the strong interactions) or two gluons etc. These colour singlets have not been observed and are often classed as *"exotica"*.

Searches for these states try to find particles that do not fit into the standard meson or baryon spectrum. One of the ways to look for *"exotica"* and in particular four-quark states ($q\bar{q}q\bar{q}$) is through the vector meson pair production

in two photon interactions.

The interest in $q\bar{q}q\bar{q}$ state searches in the two photon collisions started with the observation of an unexpected large cross section for the reaction $\gamma\gamma \to \rho^0\rho^0$ around the nominal $\rho\rho$ threshold. This led to speculation of many theoretical approaches varying from the simple explanation of the t-channel factorization to the existence of $q\bar{q}q\bar{q}$-states.

These models also made specific quantitative predictions for the production of other vector-meson pairs produced in two photon interactions. This thesis contributes to the understanding of vector-meson pair production in two photon interactions with the first observation and measurement of the reactions $\gamma\gamma \to \omega\omega$ and $\gamma\gamma \to \rho^+\rho^-$. It is organized as follows: In Chapter 1 a brief review of the kinematics for the two photon interactions is given. Then existing theoretical models and their predictions are discussed. These models provide some background information on what should be observed experimentally. In Chapter 2 the ARGUS detector which is the tool to perform the experimental search is described. Information about the particle identification capabilities, its hardware and its software support are given. In Chapters 3 and 4 details of the analysis of the reactions $\gamma\gamma \to 2\pi^+2\pi^-2\pi^0$ and $\gamma\gamma \to \pi^+\pi^-\pi^0\pi^0$ are discussed. The observation of vector mesons in these final states is presented. In Chapter 5 the experimental results are compared to the theoretical predictions given in Chapter 1.

Contents

List of Figures

List of Tables

Chapter 1

Introduction

The quantized theory of electromagnetism, Quantum Electrodynamics (QED), predicts that interactions occur between the field quanta, the photons. Two photon interactions can only be observed at large photon energies, since for low energy photons, for example photons in the optical range, the cross section is extremely small.

The first theoretical approaches relevant to two-photon physics, advanced in 1960, were the suggestion by F. Low [1] to measure the two photon coupling of the π^0 at storage rings via the reaction $e^\mp e^- \rightarrow e^\mp e^- \pi^0$ and the calculations by Calogero and Zemach [2] of the process $e^-e^- \rightarrow e^-e^-\pi^+\pi^-$. However, only in the seventies, when the electron storage rings were built, did the observation of two photon interactions become possible. The e^+e^- storage rings like DORIS, PEP, PETRA,..., provide very intense photon sources. In the following sections, the kinematics of two photon interactions, the luminosity function and resonance production are briefly reviewed. More details can be found in the review articles of reference [3].

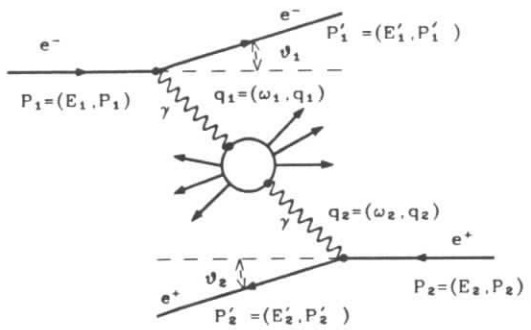

Figure 1.1: The two photon interaction diagram.

1.1 Kinematics

The two photon collisions proceed via the reaction

$$e^+e^- \rightarrow e^+e^-X \tag{1.1}$$

as in the diagram shown in figure 1.1 where X is produced by the two photons, $\gamma\gamma \rightarrow X$.

For inclusive detection of X the kinematics of the reaction 1.1 is completely determined by the four momenta of the incoming and the scattered electron and positron. In the case of unpolarized beams (as in the ARGUS experiment) there is no overall azimuthal dependence, therefore only five variables are needed to specify the $\gamma\gamma$ system at a given beam energy E_{beam}. A convenient set of variables is provided by the energies and the angles, with respect to the beam

axis, of the scattered leptons $(E'_1, E'_2, \theta_1, \theta_2)$ and the angle ϕ between the two lepton scattering planes.

The squared invariant mass of the spacelike photons is

$$q_i^2 = (p_i - p_i')^2 = \tag{1.2}$$
$$2m_e^2 - 2E_{beam}E_i'\left(1 - cos\theta_i\sqrt{1-\left(\frac{m_e}{E_{beam}}\right)^2}\sqrt{1-\left(\frac{m_e}{E_i}\right)^2}\right) .$$

Defining the quantity

$$Q_i^2 = -q_i^2$$

and using the approximation $E_{beam}, E_i \gg m_e$ the above formula reduces to

$$Q_i^2 \simeq 2E_{beam}E_i'(1 - cos\theta_i) = 4E_{beam}E_i'sin^2\left(\frac{\theta_i}{2}\right) \tag{1.3}$$

The center of mass energy of the $\gamma\gamma$ system, denoted by $W_{\gamma\gamma}$, is

$$W_{\gamma\gamma}^2 = (q_1 + q_2)^2 = M_X^2 \tag{1.4}$$

A few general features of the two photon system can be noted. The photons are emitted predominantly at small angles of the order m_e/E_{beam} with respect to the beam axis. This leads to small (space like) momentum transfer to the system X. Thus the Q^2 spectrum will be strongly peaked at zero, which means that most of the photons will be nearly real and the scattered electrons will be close to the beam axis. As a result the two photon system will have a very small transverse momentum which is the main experimental tool used to extract two

photon events from the data. The invariant mass of the system X peaks at small energies because the photon energies follow roughly the bremstrahlung spectrum $\sim 1/E_{beam}$.

1.2 The Luminosity Function

A measurement of reaction 1.1 yields a value for the cross section $e^+e^- \rightarrow e^+e^-X$. In order to extract the cross section of $\gamma\gamma \rightarrow X$, the cross section $\sigma(e^+e^- \rightarrow e^+e^-X)$ is unfolded into $\sigma(e^+e^- \rightarrow \gamma\gamma)$ and $\sigma(\gamma\gamma \rightarrow X)$. A brief description of the calculation of the cross section $\sigma(e^+e^- \rightarrow e^+e^-X)$ is presented below. A detailed calculation can be found in references [4,5].

The expression for the cross section $\sigma(e^+e^- \rightarrow e^+e^-X)$ can be obtained from the diagram shown in figure 1.1. The matrix element can be factorized into three terms, two for the lepton-photon vertices and one for the $\gamma\gamma$ coupling for the system X.

The matrix element has the form

$$\mathcal{M} = \frac{e^4}{q_1^2 q_2^2} \left[\overline{u}\left(p_1', s_1'\right)\gamma^\mu u\left(p_1, s_1\right)\right]\left[\overline{v}\left(p_2', s_2'\right)\gamma^\nu v\left(p_2, s_2\right)\right] \cdot \quad A^X_{\mu\nu} \tag{1.5}$$

where s_i are the spins of the leptons, u and v are the Dirac spinors for a free electron and positron respectively. $A^X_{\mu\nu}$ describes the coupling of the two photons to the final state X. The differential cross section is then

$$d\sigma(e^+e^- \rightarrow e^+e^-X) = \frac{\alpha^2}{64\pi^4 E_{beam}^2 q_1^2 q_2^2}\{\rho_1^{\mu\nu}\rho_2^{\mu'\nu'}\}M^X_{\mu\nu\mu'\nu'}\frac{d^3\vec{p_1}d^3\vec{p_2}}{E_1' E_2'} \tag{1.6}$$

where the density matrices for the photons are given by

$$\rho_i^{\mu\nu} = -\frac{q_i^2 g^{\mu\nu} + 2(p_i'^{\mu}p_i^{\nu} + p_i^{\mu}p_i'^{\nu})}{q_i^2} \tag{1.7}$$

and the tensor describing the production of the state X is

$$M^X_{\mu\nu\mu'\nu'} = 8\pi^2 \int A^X_{\mu\nu}A^X_{\mu'\nu'}\delta(q_1 + q_2 - P_X)d\Gamma_X \tag{1.8}$$

where P_X is the four momentum of the final state X and the integral is over the final state phase space, Γ_X.

The tensor $M^X_{\mu\nu\mu'\nu'}$ has 256 components. By requiring Lorentz invariance and current conservation it can be expressed in terms of 10 independent functions. From time invariance arguments two of these are zero and in the case of unpolarized beams two more vanish.

Working in the helicity basis described in [5], the differential cross section becomes

$$\begin{aligned} d\sigma(e^+e^- \rightarrow e^+e^-X) \;=\; & \frac{\alpha^2\sqrt{(q_1q_2)^2 - q_1^2q_2^2}}{32\pi^4 E_{beam}^2 q_1^2 q_2^2}\left\{\frac{d^3\vec{p_1}d^3\vec{p_2}}{E_1'E_2'}\right\} \\ & \times\left\{4\rho_1^{++}\rho_2^{++}\sigma_{TT} + 2\rho_1^{++}\rho_2^{00}\sigma_{TL}\right. \\ & +2\rho_1^{00}\rho_2^{++}\sigma_{LT} + \rho_1^{00}\rho_2^{00}\sigma_{LL} \\ & +2\mid\rho_1^{+-}\rho_2^{+-}\mid\tau_{TT}cos(2\phi) \\ & \left.-8\mid\rho_1^{+0}\rho_2^{+0}\mid\tau_{TL}cos(\phi)\right\} \end{aligned} \tag{1.9}$$

where σ's and τ's are the cross sections for $\gamma\gamma \rightarrow X$ for transverse (T) and longitudinal (L) photons, and the symbols +,−,0 stand for the photon helicity. But for real photons we only have transverse polarizations, so for $Q_i^2 \rightarrow 0$, all

terms with an L subscript vanish. After integration over the angle between the planes of the two leptons (ϕ), the term τ_{TT} vanishes and the differential cross section for $e^+e^- \to e^+e^-X$ can be approximated as

$$d\sigma(e^+e^- \to e^+e^-X) = \frac{\alpha^2\sqrt{(q_1q_2)^2 - q_1^2q_2^2}}{32\pi^4 E_{beam}^2 q_1^2 q_2^2} 4\rho_1^{++}\rho_2^{++} \times \sigma_{TT}(W_{\gamma\gamma}, q_1^2, q_2^2)\frac{d^3p_1' d^3p_2'}{E_1' E_2'} \quad (1.10)$$

Introducing the "two-photon luminosity function" for transversely polarized photons, $\mathcal{L}_{\gamma\gamma}^{TT}$, this becomes

$$\frac{d^5\sigma(e^+e^- \to e^+e^-X)}{d\omega_1 d\omega_2 d\theta_1 d\theta_2 d\phi} = \frac{d^5\mathcal{L}_{\gamma\gamma}^{TT}}{d\omega_1 d\omega_2 d\theta_1 d\theta_2 d\phi}\sigma_{TT}(W_{\gamma\gamma}, q_1^2, q_2^2) \quad (1.11)$$

where $\omega_i = E_{\gamma_i}/E_{beam}$. The differential luminosity function is defined as

$$\frac{d^5\mathcal{L}_{\gamma\gamma}^{TT}}{d\omega_1 d\omega_2 d\theta_1 d\theta_2 d\phi} = \frac{\alpha^2 E_1' E_2'\sqrt{(q_1q_2)^2 - q_1^2q_2^2}}{16\pi^3 E_{beam}^2 q_1^2 q_2^2} 4\rho_1^{++}\rho_2^{++} \quad (1.12)$$

with

$$\rho_1^{++} = \frac{(2p_1q_2 - q_1q_2)^2}{(q_1q_2)^2 - q_1^2q_2^2} + \frac{1}{2} + 2\frac{m_e^2}{q_2^2}$$

$$\rho_2^{++} = \rho_1^{++}\,(1 \Leftrightarrow 2)$$

The differential luminosity function can be integrated numerically to find its dependence on $W_{\gamma\gamma}$. The resulting function $d\mathcal{L}_{\gamma\gamma}^{TT}/dW_{\gamma\gamma}$, following the exact

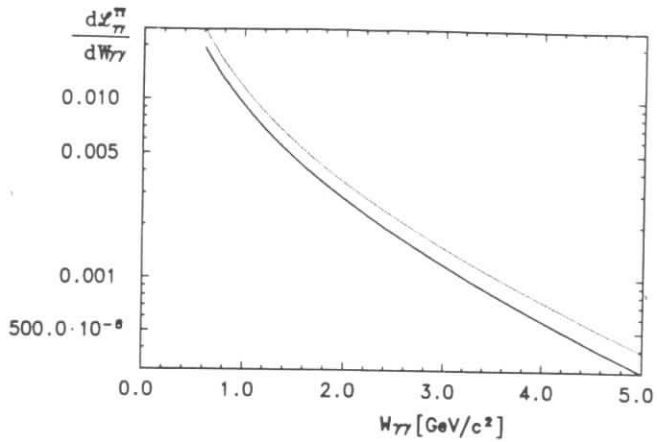

Figure 1.2: $d\mathcal{L}_{\gamma\gamma}^{TT}/dW_{\gamma\gamma}$ as a function of $W_{\gamma\gamma}$. The full line represents the exact calculation and the dotted line the calculation with the Equivalent Photon Approximation (EPA)

calculation given in [4] and [6], for the case of E_{beam}=5 GeV, is plotted in figure 1.2.

Sometimes it is convenient to use *"the Equivalent Photon Approximation"* for $\mathcal{L}_{\gamma\gamma}^{TT}$ given by

$$\frac{d\mathcal{L}_{\gamma\gamma}^{TT}}{dW_{\gamma\gamma}} = \frac{4\alpha^2}{\pi^2 W_{\gamma\gamma}}(ln\eta)^2 f(z) \quad (1.13)$$

where $\eta = E_{beam}/m_e$ when the scattered electron is not detected (no tag mode) and $\eta = \theta_{max}/\theta_{min}$ when it is detected in the polar range between θ_{min} and θ_{max}. The *"Low function"* $f(z)$ is given by [1]

$$f(z) = \left(2+z^2\right)^2 ln\left(\frac{1}{z}\right) - \left(1-z^2\right)\left(3+z^2\right) \tag{1.14}$$

where $z = W_{\gamma\gamma}/2E$.

This approximation is convenient for analytical calculations of cross sections and is used for approximate rate estimates. For not too large z ($z < 0.8$, this formula overestimates the exact luminosity by about 10 % to 20 % but reproduces the shape of the function quite well.

1.3 The Formation of Resonances

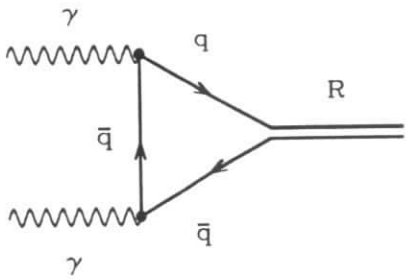

Figure 1.3: Diagram for resonance formation in two photon interactions.

The two-photon cross section for the formation (figure 1.3) of a resonance with a mass M_R, spin J and total width Γ can be written as [5]

$$\sigma(\gamma\gamma \to R) = \frac{32\pi(2J+1)}{h_1 h_2} \cdot \frac{W_{\gamma\gamma}^2}{2\sqrt{X}} \cdot \frac{\Gamma\Gamma_{\gamma\gamma}}{\left(W_{\gamma\gamma}^2 - M_R^2\right)^2 + \Gamma^2 M_R^2} \tag{1.15}$$

where h_1, h_2 are the number of helicity states allowed for the photons and $X = (q_1 \cdot q_2)^2 - q_1^2 q_2^2$. $\Gamma_{\gamma\gamma}$ is the partial $\gamma\gamma$ width of R, and is the quantity measured in two photon production of R. In the limit of resonance formation by (quasi-) real photons ($q_1^2, q_2^2 \to 0$) only two helicity states are allowed for each photon and the formula 1.15 becomes

$$\sigma(\gamma\gamma \to R) = 8\pi(2J+1) \cdot \frac{\Gamma\Gamma_{\gamma\gamma}}{\left(W_{\gamma\gamma}^2 - M_R^2\right)^2 + \Gamma^2 M_R^2} \tag{1.16}$$

The resonance R must have even charge conjugation, C, since it is formed from two photons. Only resonances with spin parity quantum numbers $J^P = 0^\pm, 2^\pm, 3^\pm, 4^\pm \ldots$ can couple to two real photons. Spin 1 mesons do not couple to two real photons as required by the Landau-Yang theorem [Appendix A].

1.4 Motivation for the Experiment

The observation, by several groups, of an unexpectedly large cross section of the reaction $\gamma\gamma \to \rho^0\rho^0$ ref. [8-12] below the nominal $\rho\rho$ threshold and the relatively suppressed upper limits for the reaction $\gamma\gamma \to \rho^+\rho^-$ [13] (figure 1.4) generated great interest in vector meson production in two photon interactions. A large variety of theoretical models dealt with these measurements. Some of these models make specific predictions on phenomena that are yet to be observed. In this thesis, a contribution to the understanding of the vector meson pair production in photon-photon interactions is made by the first observation and measurement of the channels $\gamma\gamma \to \omega\omega$ and $\rho^+\rho^-$. Before this presentation some of the current theories are discussed, as well as some of the present experimental data.

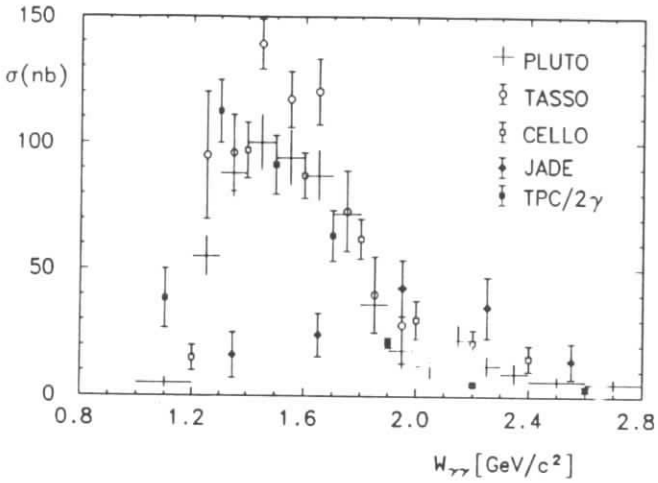

Figure 1.4: Cross section for $\gamma\gamma \to \rho\rho$ from references [8-12,13]. All the data are on the $\gamma\gamma \to \rho^0\rho^0$ channel except those from JADE that are on $\gamma\gamma \to \rho^+\rho^-$.

1.5 Vector Meson Dominance model

The Vector Meson Dominance model (VDM) is the oldest and mos common model applied to the hadronic interactions of photons. The model was introduced in 1960 by Sakurai [14] to explain the large cross sections observed in inelastic electron proton scattering. The model was later used to describe the energy dependence of the e^+e^- annihilation into a virtual photon at low energies. It has also been applied to explain some phenomena observed in two photon interactions. In many models used in two photon physics, the photon is described as a superposition of wave functions with the same quantum numbers

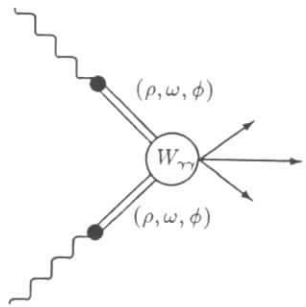

Figure 1.5: Vector Dominance Model

$$| \Psi >= \alpha_1 | \gamma > + \alpha_2 | l^+l^- > + \alpha_3 | q\overline{q} > + \ldots \qquad (1.17)$$

where the first term corresponds to a real photon, the second to a lepton pair and the third to a quark-antiquark pair. The higher order terms contain more than two quarks, and also interference terms.

In the VDM one assumes that the hadronic interactions proceed via one of the vector mesons ($\rho^0, \phi, \omega \ldots$), since these have the same quantum numbers as the photon (figure 1.5).

In two photon interactions the VDM predicts the occurrence of processes like $\gamma\gamma \to \rho^0\rho^0, \rho^0\phi, \phi\phi, \omega\omega, \ldots$ where both photons convert into flavorless vector mesons which then scatter elastically with one pomeron or meson exchange (figure 1.6).

The cross section for such a process is

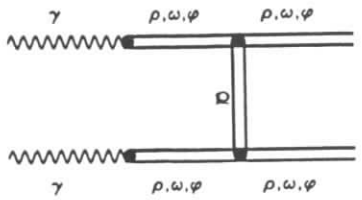

Figure 1.6: One pomeron or pion exchange.

$$\sigma_{\gamma\gamma\to VV'} = (4\pi\alpha)^2 \frac{g_{V\gamma}^2 g_{V'\gamma}^2}{M_V^4 M_{V'}^4} \rho_{VV'} \sigma_{VV'\to VV'} \tag{1.18}$$

where $g_{V\gamma}$ is the coupling of the vector meson V to the photon, M_V is its mass and $\rho_{VV'}$ is the phase space factor

$$\rho_{VV'} = \frac{\left(W_{\gamma\gamma}^2 - (M_V + M_{V'})^2\right)^{\frac{1}{2}} \cdot \left(W_{\gamma\gamma}^2 - (M_V - M_{V'})^2\right)^{\frac{1}{2}}}{W_{\gamma\gamma}^2} \tag{1.19}$$

The coupling $g_{V\gamma}$ can be extracted from the decay of the vector meson to an e^+e^- pair.

For example, a simplified VDM argument leads [15] to

$$\sigma(\gamma\gamma \to \rho\rho) = \left(\frac{\alpha\pi}{\gamma_\rho^2}\right)^2 \cdot \left(\frac{p_\rho^*}{k_\gamma^*}\right)^2 \cdot \sigma(\rho\rho \to \rho\rho) \tag{1.20}$$

where γ_ρ is the equivalent photon coupling constant to the ρ-meson ($\gamma_V = em_V^2/g_{V\gamma}$ and $\frac{\alpha\pi}{\gamma_\rho^2} = 2.85 \cdot 10^{-3}$), p_ρ^* and k_γ^* are the momenta of the ρ-mesons and photons, in the center-of-mass system, respectively

$$\left(k_\gamma^*\right)^2 = \left(\frac{W}{2}\right)^2 \quad \text{and} \quad \left(p_\rho^*\right)^2 = \left(\frac{W}{2}\right)^2 - m_\rho^2 \tag{1.21}$$

The factor $(p^*/k^*)^2$ accounts for the different relative velocities for $\gamma\gamma$ and $\rho\rho$ at fixed invariant mass W. The elastic cross section $\sigma_{\rho\rho\to\rho\rho}$ is not directly measurable but can be estimated from other related processes (like $\pi\pi \to \pi\pi$, $\pi N \to \pi N$, $pp \to pp$, ...) by using, for example an additive quark model. In this framework one expects

$$\sigma_{\rho\rho\to\rho\rho} \simeq \sigma_{\pi\pi\to\pi\pi} \simeq \frac{2}{3}\sigma_{\pi N\to\pi N} \simeq \frac{4}{9}\sigma_{pp\to pp} \tag{1.22}$$

leading to the parametrization [15]

$$\sigma(\gamma\gamma \to \rho\rho) \simeq \left(\frac{p^*}{k^*}\right)^2 \cdot 34\ nb \tag{1.23}$$

The cross section for this simple minded VDM calculation is shown in figure 1.7.

1.6 t-channel Factorization Model

Alexander *et al.* [16] constructed a model using t-channel factorization. They suggest that the $\sigma_{\gamma\gamma\to VV'}$ can be factorized as

$$\sigma_{\gamma\gamma\to VV'} = \sum_i \frac{\sigma_{\gamma p\to Vp}\cdot\sigma_{\gamma p\to V'p}\cdot F^2_{\gamma p}}{\sigma_{pp\to pp}\cdot F_{pp}F_{\gamma\gamma}} \tag{1.24}$$

where the summation is over the pomeron exchange process (diffractive chan-

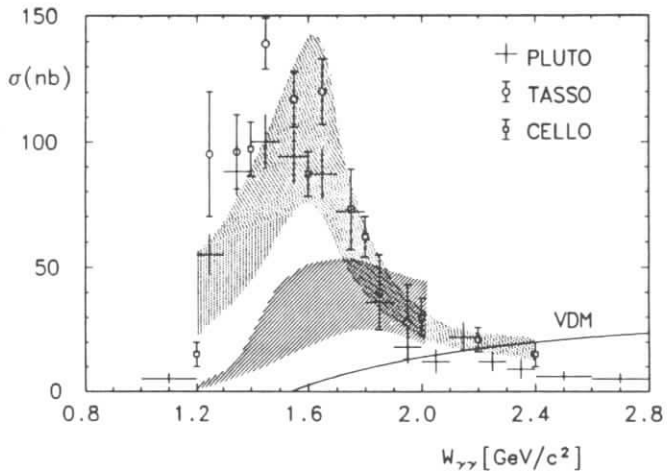

Figure 1.7: Calculation of the cross section for the reaction $\gamma\gamma$ - $\rho^0\rho^0$ according to the VDM and the t-channel factorization models. The VDM expectation is given as a full line; the t-channel factorization model by Alexander *et al.* as a dotted area and by Kolanoski as a hatched area.

nel) and the one pion exchange process (OPE), as in figure 1.6. The F_{ij} represent flux factors due to the different masses involved in the calculation. The photoproduction data, at fixed photon energies in the center of mass system of the final state particles, were used to estimate the cross section for different channels. The predictions of this model are shown in figure 1.7.

Their approach explains the existing data for the reaction $\gamma\gamma \to \rho^0\rho^0$ quite

well. However this result is not unambiguous. Kolanoski [17] has performed the same calculation for this specific channel using a different method for accounting the ρ width. His result is significantly different below the nominal $\rho^0\rho^0$ threshold and is also shown in figure 1.7.

1.7 4-Quark States

The existence of bound states of four quarks ($q\bar{q}q\bar{q}$) is predicted in the MIT bag model [18]. The model assumes that colored quarks and massless colored gluons are confined in the hadrons by the introduction of a constant energy density term into the interaction hamiltonian. In this model the masses of the u and d quarks are set to zero and the s quark mass is tuned to the lowest $q\bar{q}$ and qqq states. The basic parameters of the model are the bag constant or confining pressure $B^{\frac{1}{4}} = 146$MeV, the strange quark mass $m_s = 279$MeV, the gluon coupling constant $\alpha = 0.55$ and a parameter that represents the energy shifts due to zero point fluctuations, $z_0 = -1.84$. Using these parameters which are *"derived"* from the ordinary hadrons, one can extrapolate and estimate the masses of the $q\bar{q}q\bar{q}$ states [18].

If one uses the SU(3) property of a quark pair being in either a symmetric **6** or an antisymmetric $\overline{\mathbf{3}}$ flavor multiplet, and couples the quark-pair to the multiplets of a $\overline{q\bar{q}}$ pair taking into account the Pauli principle, then one can construct the multiplet structure of the $q\bar{q}q\bar{q}$ states (see for example [19], chapter 19).

Using this recipe the following S-wave multiplets arise:

$$\begin{aligned} J^P &= 2^+ : \mathbf{9}, \mathbf{36} \\ J^P &= 1^+ : \mathbf{9}, \mathbf{36}, \mathbf{18}, \mathbf{18}^*, \overline{\mathbf{18}}, \overline{\mathbf{18}}^* \\ J^P &= 0^+ : \mathbf{9}, \mathbf{9}^*, \mathbf{36}, \mathbf{36}^* \end{aligned}$$

Two multiplets with identical overall spin and flavor content are distinguished by an asterisk (applied to the heavier).

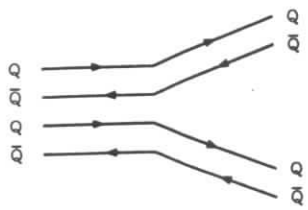

Figure 1.8: OZI-superallowed decay for a $q\bar{q}q\bar{q}$-state.

The four quark state can decay by simply falling apart into two ordinary mesons (figure 1.8). This decay is usually referred to as the Zweig-superallowed mode. A direct and very important consequence is that, if a $q\bar{q}q\bar{q}$ state falls apart, then its decay width is expected to be very large, of the order of several hundred MeV. This makes the detection of such a state very difficult. But, if the decay has a low Q-value, phase space suppression can make the resonance narrow enough to be identified.

Since the $q\bar{q}q\bar{q}$ states can be considered as bound states of meson pairs, two photon interactions, which according to the VDM proceed via two vector mesons, are expected to provide a *"clean"* channel to look for $q\bar{q}q\bar{q}$ states decaying into two vector mesons. According to Landau-Yang's theorem (Appendix A) only $q\bar{q}q\bar{q}$ states with J^P either 0^+ or 2^+ can be produced in two photon interactions.

These ideas have been worked out by two groups [20,21]. In the following, the results obtained by Achasov *et al.* [20] will be presented. Li and Liu [21] use a slightly different formulation, but they arrive at very similar results.

According to the formulation described by Achasov *et al.* the $\gamma\gamma$ width of a

$q\bar{q}q\bar{q}$ state R decaying via two neutral vector mesons is expressed as

$$\Gamma_{R\to\gamma\gamma} = \frac{|\, A(R \to V_0 V_0' \to \gamma\gamma)\,|^2}{16\pi m_R^2} \tag{1.25}$$

with the amplitude A given by

$$A(R \to V_0 V_0' \to \gamma\gamma) = g_{R\gamma\gamma} = g_0 A(V_0 V_0') \frac{e^2}{f_V \cdot f_{V'}} \cdot C \cdot \begin{cases} 1 & V_0 = V_0' \\ \sqrt{2} & V_0 \neq V_0' \end{cases} \tag{1.26}$$

where $A(V_0V_0')$ is the probability of a four quark resonance to be in the V_0V_0' state. C is a term which accounts for the fact that not all the available spin states can turn into massless photons and is $\sqrt{\frac{2}{3}}$ for $J^P = 0^+$ and $\sqrt{\frac{7}{15}}$ for $J^P = 2^+$. The factors 1 and $\sqrt{2}$ are due to Bose statistics, and g_0 is the Zweig-superallowed dimensional coupling constant which is of the order of 10 GeV.

Using these results, the cross section for $\gamma\gamma \to R(q\bar{q}q\bar{q}) \to VV'$ is expressed as :

$$\sigma(\gamma\gamma \to R(q\bar{q}q\bar{q}) \to VV') = \frac{(2J+1)\cdot\rho_{VV'}}{32\pi W_{\gamma\gamma}^2} \left| \frac{g_{R\gamma\gamma} g_{RVV'}}{D(a, m_R, W_{\gamma\gamma})} \right|^2 \tag{1.27}$$

where $\rho_{VV'}$ is the phase space factors for the two vector mesons, as in 1.19, $g_{R\gamma\gamma}$ is the coupling of the two photons to the resonance R, $g_{RVV'}$ is the coupling of the resonance to the two vector mesons

$$g_{RVV'} = g_0 A(VV') \tag{1.28}$$

D is the inverse of a Breit-Wigner resonance propagator

$q\bar{q}q\bar{q}$	I	$\rho^+\rho^-$	$\rho^0\rho^0$	$K^{*+}K^{*-}$	$K^{*0}\overline{K}^{*0}$	$\omega\omega$	$\omega\phi$	$\rho^0\phi$	$\omega\rho^0$	$\phi\phi$
$C^0(\underline{9})$	0	$\sqrt{\frac{1}{2}}$	$\frac{1}{2}$	0	0	$-\frac{1}{2}$	0	0	0	0
$C^S(\underline{9})$	0	0	0	$\frac{1}{2}$	$\frac{1}{2}$	0	$-\frac{1}{2}$	0	0	0
$C^S_\pi(\underline{9})$	1	0	0	$-\frac{1}{2}$	$\frac{1}{2}$	0	0	$\sqrt{\frac{1}{2}}$	0	0
$E(\underline{36})$	2	$-\sqrt{\frac{1}{3}}$	$\sqrt{\frac{2}{3}}$	0	0	0	0	0	0	0
$C_\pi(\underline{36})$	1	0	0	0	0	0	0	0	1	0
$C^0(\underline{36})$	0	$\sqrt{\frac{1}{6}}$	$\frac{1}{2\sqrt{3}}$	0	0	$\frac{\sqrt{3}}{2}$	0	0	0	0
$C^S_\pi(\underline{36})$	1	0	0	$\frac{1}{2}$	$-\frac{1}{2}$	0	0	$\sqrt{\frac{1}{2}}$	0	0
$C^S(\underline{36})$	0	0	0	$\frac{1}{2}$	$\frac{1}{2}$	0	$\sqrt{\frac{1}{2}}$	0	0	0
$C^{SS}(\underline{36})$	0	0	0	0	0	0	0	0	0	1

Table 1.1: The flavour structure of the four-quark-states.

$$D(a, m_R, W_{\gamma\gamma}) = m_R^2 - W_{\gamma\gamma}^2 - i\,(a m_R \Gamma_R(m_R) + W_{\gamma\gamma}\Gamma_R(W_{\gamma\gamma})) \qquad (1.29)$$

The width $\Gamma_R(W_{\gamma\gamma})$ is the sum of the partial widths $\Gamma_{RVV'}$ of all the meson pairs that contribute to the decay of the resonance R

$$\Gamma_R(W_{\gamma\gamma}) = \sum_{VV'} \frac{g^2_{RVV'}}{16\pi W_{\gamma\gamma}} \cdot \rho_{VV'}(s) \cdot \begin{cases} 1 & V \neq V' \\ \frac{1}{\sqrt{2}} & V = V' \end{cases} \qquad (1.30)$$

In the case of the ρ-meson which has a large width, the flux factor is weighted by the resonance shape of the meson. The parameter a in 1.29 is the only free parameter of the model and takes into account all the contributions from the non-Zweig-superallowed decays to the width of the $q\bar{q}q\bar{q}$ resonance.

In addition, the MIT bag model predicts several resonances with similar masses which contribute to the same channel. Their contribution to the reactions $\gamma\gamma \to VV'$ is shown in Table 1.1.

Using the Achasov formulas [20, (1985)], the cross sections for several $\gamma\gamma \to VV'$ processes have been calculated and are shown in figure 1.9.

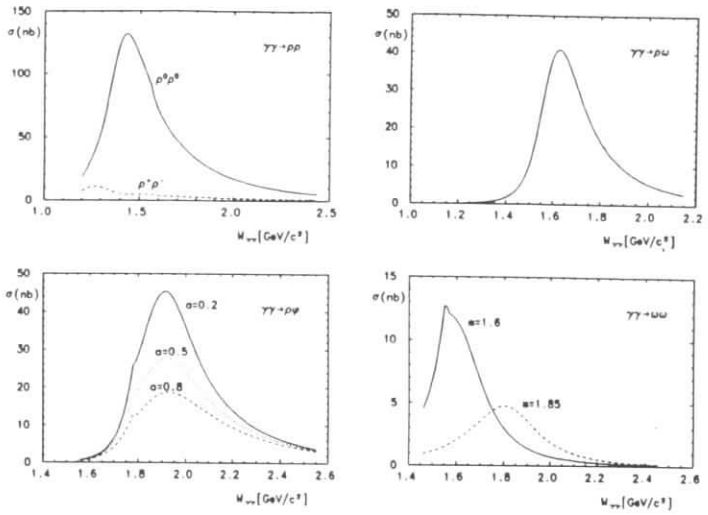

Figure 1.9: Expectations for the cross sections of $q\bar{q}q\bar{q}$-states decaying in various vector meson pairs according to the formulation given by Achasov *et al.* in reference [20, (1985)].

The model predicts a cross section for the reaction $\gamma\gamma \to \rho^0\rho^0$ of the order of 100 nb whereas the predicted cross section for the reaction $\gamma\gamma \to \rho^+\rho^-$ is much smaller. This is a result of the interference between the isoscalars $C^0(\mathbf{36}, 2^+)$ and $C^0(\mathbf{9}, 2^+)$ and the isotensor $E(\mathbf{36}, 2^+)$, which are degenerate in mass. As first pointed out by Li and Liu [21, (1982)], a resonance with definite isospin 0 or 2 yields different ratios of the cross sections between neutral and charged decay modes. This is obvious if one writes down the isotopic structure of the two ρ-meson wave functions :

$$|\rho^0\rho^0> = \sqrt{\frac{1}{3}}\,|0> + \sqrt{\frac{2}{3}}\,|2> \quad (1.31)$$

$$|\rho^+\rho^-> = \sqrt{\frac{2}{3}}\,|0> - \sqrt{\frac{1}{3}}\,|2> \quad (1.32)$$

where $|0>$, $|2>$ are the isospin states. For I=0 $\sigma_{\gamma\gamma\to\rho^0\rho^0}/\sigma_{\gamma\gamma\to\rho^+\rho^-}$=1/2 and for I=2 the ratio equals to 2.

1.8 Glueballs

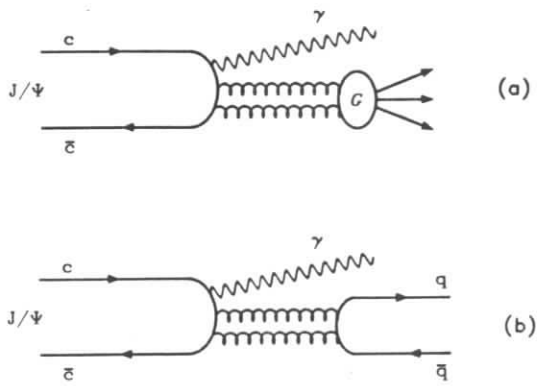

Figure 1.10: Diagrams for the decays a) $J/\Psi \to \gamma Glueball$ and b) $J/\Psi \to \gamma Meson$

The MIT bag model [22] predicts, in addition to the 4-quark states, introduced in section 1.6, the existence of bound states of gluons, the so called gluonium states and often referred to as glueballs. Several of these states are predicted,

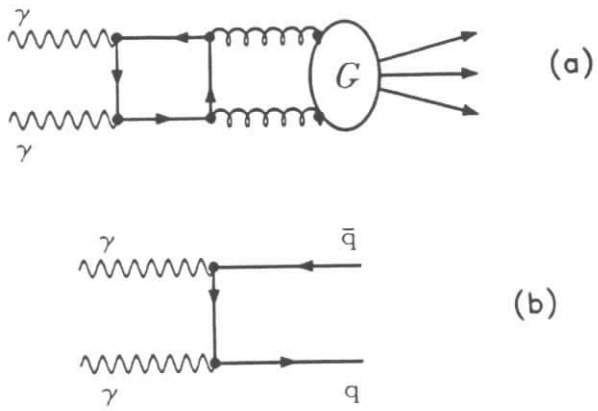

Figure 1.11: Diagrams for the reactions a) $\gamma\gamma \to Glueball$ and b) $\gamma\gamma \to Meson$

with masses less than 2 GeV, and width of the order of hundreds of MeV due to the strong coupling to the hadrons. The glueballs are expected to have the same quantum numbers as the ordinary hadrons. This makes it difficult to distinguish a glueball from a meson.

Radiative J/Ψ decays are suggested as a good source of glueballs. These decays proceed via the lowest QCD diagram shown in figure 1.10.

In this diagram the $c\bar{c}$ pair of the J/Ψ annihilates into a photon and two gluons. The coupling of the two gluons to the $c\bar{c}$ pair is of the order of α_s^2. In the case in which an ordinary meson is produced we have another factor α_s^2 due to the additional coupling of the gluons to the quarks of the meson. From that we can conclude that the ratio of the widths of a glueball G and a meson M (assuming the same properties for the glueball and the meson) is

$$\frac{\Gamma(J/\Psi \to \gamma G)}{\Gamma(J/\Psi \to \gamma M)} = \frac{1}{\alpha_s^2} \tag{1.33}$$

On the other hand, in the case of two photon collisions, the formation of a glueball proceeds via a quark loop with coupling proportional to $\alpha^2\alpha_s^2$, whereas the $q\bar{q}$-meson has a coupling proportional to α^2 because of its direct creation (figure 1.11.). Therefore, for two photon interactions we have

$$\frac{\Gamma(\gamma\gamma \to G)}{\Gamma(\gamma\gamma \to M)} = \alpha_s^2 \tag{1.34}$$

1.9 Related Measurements from Oth :r Experiments

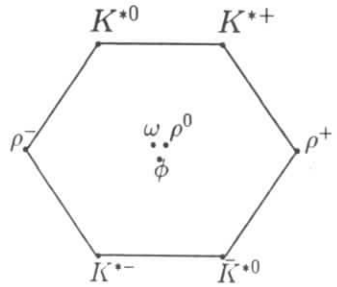

Figure 1.12: Vector meson nonet for the lowest mass state..

Vector meson pair production has been extensively studied in radiative J/Ψ decays as well as in the two photon interactions. In the following, existing measurements for the processes $J/\Psi \to \gamma VV'$ and $\gamma\gamma \to VV'$ are presented, where

V, V' are vector mesons from the lowest mass vector meson nonet (figure 1.12). Combined measurements of the two processes can give useful information for the existence of glueballs (see section 1.8).

1.9.1 Radiative J/Ψ Decays.

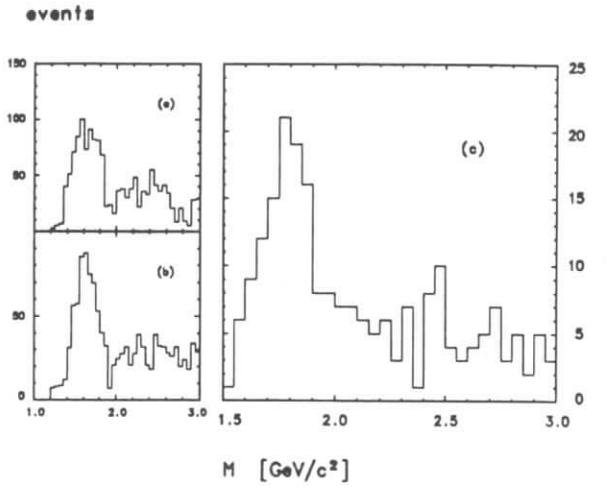

Figure 1.13: Mass spectra of the two vector mesons for the decays a) $J/\Psi \to \gamma\rho^0\rho^0$ b) $J/\Psi \to \gamma\rho^+\rho^-$ and c)$J/\Psi \to \gamma\omega\omega$.

Most of the data on vector meson pair production in radiative J/Ψ decays come from the MARK III and DM2 collaborations.

The reaction $J/\Psi \to \gamma\rho\rho$ has been observed by both collaborations [24] in the neutral and the charged modes, with structures around 1.5, 1.8 and 2.1 GeV/c^2 (figure 1.13). A spin parity analysis showed that these tentative states have $J^P = 0^-$.

Mass [GeV/c^2]	VV'	J^P
~ 1.5	$\rho\rho$	0^-
~ 1.8	$\rho\rho$	0^-
~ 2.1	$\rho\rho$	0^-
< 2.0	$\omega\omega$	0^-
~ 2.2	$\phi\phi$	0^-
< 2.0	$K^{*0}\overline{K}^{*0}$	0^-

Table 1.2: States decaying into VV' observed in radiative decays $J/\Psi \to \gamma VV'$

The measurement of the reaction $J/\Psi \to \gamma\omega\omega$ showed an $\omega\omega$ peak below 2 GeV/c^2 (figure 1.13), also having $J^P = 0^-$.

The decays $J/\Psi \to \gamma\omega\phi$, $J/\Psi \to \gamma\phi\phi$ and $J/\Psi \to \gamma K^{*0}\overline{K}^{*0}$ show structures with $J^P = 0^-$ as well. Table 1.2 summarizes these results. Common to all these reactions is the result that the measured branching ratios are of the order 10^{-3}. A summary of all these results and an attempt to explain the data can be found in the review article on the J/Ψ decays by Köpke and Wermes [26].

1.9.2 Vector Meson Pair Production in Two Photon Interactions

The two photon interaction experiments do not have the luxury of high statistics data samples as in the case of the J/Ψ studies. We have to deal with very small data samples measured in terms of tens to hundreds of events.

The channel studied the most is $\gamma\gamma \to \rho^0\rho^0$. It was observed for the first time by the TASSO collaboration [8, (1980)] at PETRA. The measurement was confirmed by MARK II [9] at SPEAR and CELLO [10] at PETRA. The main point of these measurements is the surprising large cross section far below the nominal $\rho\rho$ threshold (figure 1.4). In all these analyses fits were performed to the $2\pi^+2\pi^-$ spectra assuming that they are an incoherent mixture of $\rho^0\rho^0, \rho^0\pi^+\pi^-$ and non-resonant $2\pi^+2\pi^-$. In 1982, the TASSO group performed a spin-parity analysis of the $\rho^0\rho^0$ system by using the maximum likelihood technique that is

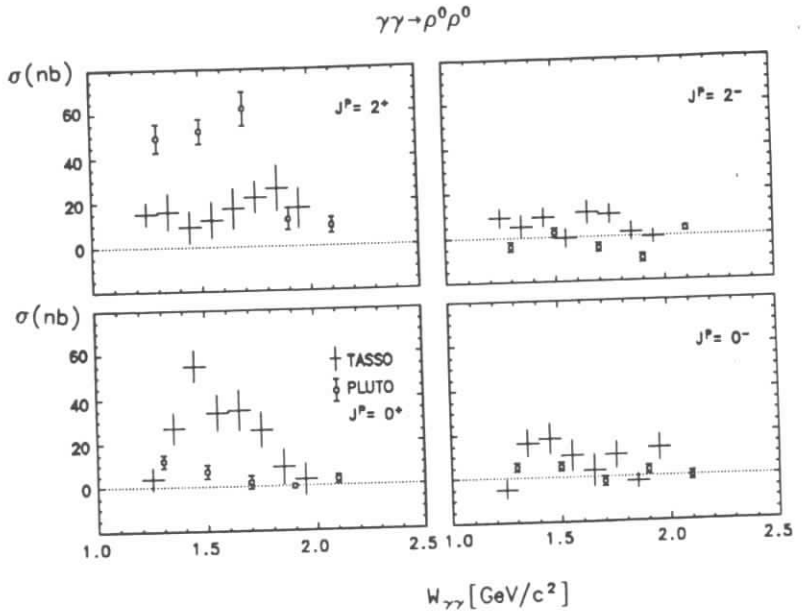

Figure 1.14: Existing results on the $\gamma\gamma \to \rho^0\rho^0$ spin-parity analysis. The crosses represent the measurement by TASSO [8] and the circles the measurement by PLUTO [11].

Channel	$W_{\gamma\gamma}[GeV/c^2]$	σ[nb] (95% CL)	Experiment
$\phi\rho$	2.0-2.2	<35	TASSO [27]
	2.2-2.4	<12	
	2.4-2.6	<8	
	2.6-3.0	<2	
	3.0-3.4	<1	
	3.4-4.2	<0.5	
$\phi\phi$	2.2-2.4	<67	TASSO [27]
	2.4-2.6	<7	
	2.6-3.4	<2	
	3.4-4.2	<1	
	4.2-6.0	<0.5	
$K^{*0}\overline{K}^{*0}$	1.8-2.0	<55	TASSO [27]
	2.0-2.4	<18	
	2.4-2.8	<10	
	2.8-3.5	<8	
$\omega\omega$	1.6-1.9	<15	PLUTO [28]
	1.9-2.2	<18	
	2.2-2.5	<20	
$\omega\rho$	1.6-1.9	<18	PLUTO [28]
	1.9-2.2	<10	
	2.2-2.5	<20	

Table 1.3: Upper limits for the cross sections $\gamma\gamma \to VV'$.

described later in the $\rho^+\rho^-$ analysis section. Recently PLUTO [11] and TPC/2γ [12] have also published a spin parity analysis of the $\rho^0\rho^0$ system. A comparison of all these angular analysis is shown in figure 1.14. The results are rather inconclusive, the only point that one can make being that positive parity states dominate the cross section.

The upper limits for the reaction $\rho^+\rho^-$ by JADE [13] (figure 1.4) showed that charged $\rho\rho$ production is suppressed. This made things even more interesting since the four-quark state models predicted just this kind of suppression (see section 1.6).

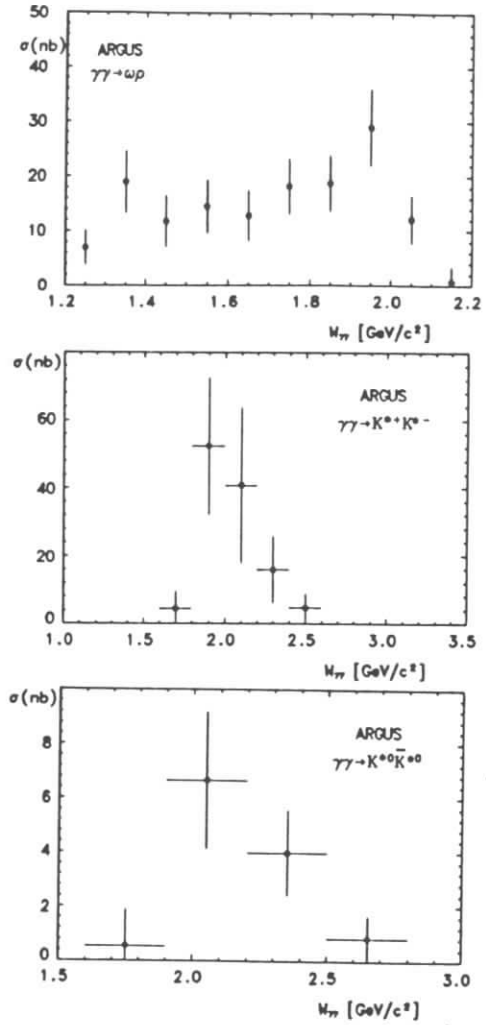

Figure 1.15: Cross sections for vector meson pair production from ARGUS [29,30,32] (excluding the results presented in later sections of this thesis).

Channel	$W_{\gamma\gamma}[GeV/c^2]$	σ[nb]	$q\bar{q}q\bar{q}$-model
$\phi\rho$	1.9-2.1	<1.1 (95% CL)	~ 28 nb
$\phi\omega$	1.9-2.5	<1.7 (95% CL)	~ 1 nb
$\phi\phi$	2.2-2.5	<7.1 (95% CL)	~ 4 nb

Table 1.4: Upper limits for the cross sections $\gamma\gamma \to \phi\rho$, $\gamma\gamma \to \phi\omega$ and $\gamma\gamma \to \phi\phi$ from ARGUS [30,31].

The upper limits for vector meson pair production in two photon interactions existing before the ARGUS measurements are listed in Table 1.3. ARGUS has made measurements of five vector meson pairs produced in two photon interactions. For the remaining three, limits have been derived and they are shown in Table 1.4. Figure 1.15 shows the ARGUS results for the vector pair production in two photon collisions. In this thesis, the first observation of the channels $\gamma\gamma \to \omega\omega$ and $\rho^+\rho^-$ is discussed in detail.

Chapter 2

The ARGUS Detector

2.1 Introduction

The ARGUS detector is located in one of the two interaction regions (figure 2.1) at the DORIS II e^+e^- storage ring at the Deutsches Elektronen SYnchrotron (DESY), situated in Hamburg, West Germany.

The ARGUS detector [34] is a magnetic solenoidal spectrometer which was designed [35] as a universal tool to analyze final states from electron-positron interactions at energies around 10 GeV, and in particular to study the Υ-system, both above and below the $B^0\overline{B}^0$ threshold, charmed meson systems, τ-lepton physics and two photon interactions.

These studies require good charged tracking capabilities with good momentum resolution and charged particle identification, as well as good neutral energy measurement. These criteria were fulfilled by constructing a detector that was finely segmented, with components of the greatest possible resolution and minimal multiple scattering and by maintaining regular calibration.

Starting from the interaction point outwards, ARGUS consists of a Vertex Drift Chamber immediately outside the beam pipe, the main Drift Chamber, the Time of Flight system, the Shower Counters and finally a set of muon chambers

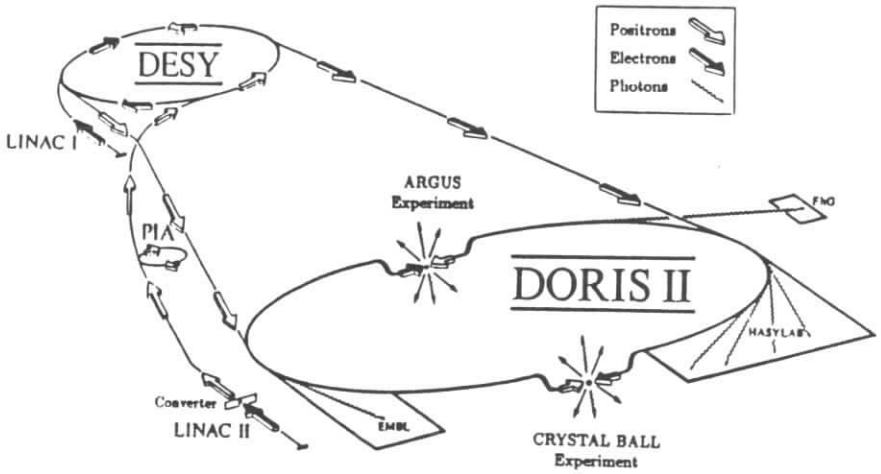

Figure 2.1: The DESY/DORIS II Accelerator Complex

(figure 2.2). Thirteen copper coils provide the 8 kG solenoidal magnetic field which is contained by an iron flux return yoke. The effect of the ARGUS magnetic field on the beams is compensated for by coils extending along the beam pipe into the detector.

Charged particles can be identified both by the measurement of specific ionization, dE/dx, in the main drift chamber and by the measurement of their velocity by the Time-of-Flight system. The momentum measurement is done with the drift chamber while the vertex drift chamber improves the vertex reconstruction. Discrimination between electrons and hadrons is performed mainly by the shower counters, which also allow the measurement of photons with energy as low as 50 MeV. Three layers of wire chambers identify muons. The magnet coils, the flux return iron yoke and the shower counters serve as absorbers.

The components of the ARGUS detector are discussed in more detail in the following pages.

2.2 DORIS

The DORIS II (acronym for DOppel RIng Speicher) storage ring [33] provides the experiment with electron and positron beams that interact within the detector. The layout of the accelerators is shown in figure 2.1. The electrons are supplied to the system by a small linear accelerator LINAC I which accelerates them up to 55 MeV. The electron beam is then injected into the DESY synchrotron. The positrons are produced by bombarding a tungsten target with electrons from LINAC II. Because the positron production rate is low, they are accumulated in a small storage ring called PIA (Positron Intensity Accumulator). When enough positrons have been saved, they are also transferred into the DESY synchrotron. The electrons and positrons are then accelerated at the requested energy between 4.5 and 5.5 GeV and they are injected into DORIS. In

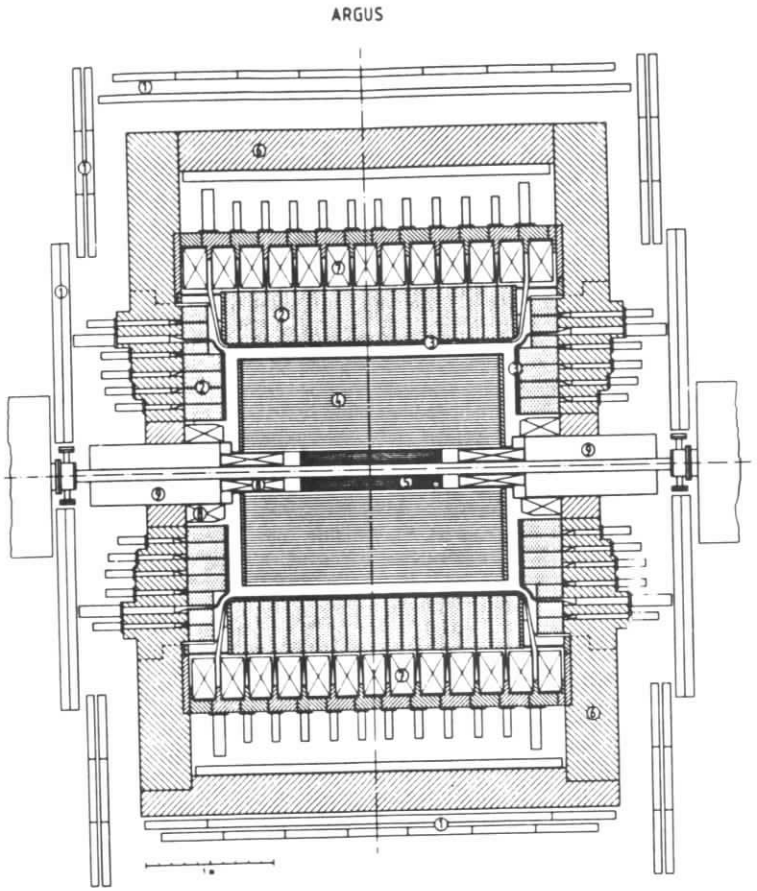

Figure 2.2: The ARGUS detector. 1) Muon chambers, 2) Shower counters, 3) Time of flight counters, 4) Drift chamber, 5) Vertex chamber, 6) Iron yoke, 7) Solenoid coils, 8) Compensation coils 9) Mini beta quadrupole .

DORIS, electrons and positrons are circulated in the same beam pipe in single bunches with currents of about 30 mA per beam and crossing period at the two interaction points of 1 μs. Typical run periods are of the order of one hour at which point the beams are replenished. The beam sizes at the interaction points have a standard deviation of about 80 μm in y, 500 μm in x and 2.5 cm in z, (the coordinate system is defined with z along the beam axis and x in the plane of the storage ring pointing to the center), if they are assumed to have Gaussian distributions.

The luminosity of a storage ring is given by :

$$\mathcal{L} = \frac{I^+ I^-}{4\pi e^2 f \sigma_x \sigma_y} \tag{2.1}$$

where I^+, I^- are the currents of the positron and the electron beams in Amperes respectively, e is the electron charge, f is the revolution frequency and σ_x, σ_y are the beam sizes in the x-y plane in cm. The luminosity for the DORIS ring with typical running conditions is about $10^{31} cm^{-2} s^{-1}$ and the integrated luminosity delivered to the detector per day about 800 nb^{-1}.

2.3 The main Drift Chamber

The heart of the ARGUS detector is the main Drift Chamber (DC) [36]. It measures the drift times of charged particles passing through its active volume and the specific ionization deposited along the track length. These measurements lead to good momentum and spatial resolution and good particle identification. The drift chamber is also used as a component of the second level trigger.

The chamber has a cylindrical geometry with an inner diameter of 30 cm, an outer diameter of 172 cm and a length of 2 m. The materials used were chosen to minimize the multiple scattering of particles coming from the interaction

point. The inner wall is made of 3.3 mm thick carbon-fibre epoxy, the outer one of 6 mm thick aluminum. The end plates are rigid enough to support the $\sim$ 31200 N tension of the wires and are made of 30 mm thick Al.

There are 5940 sense and 24588 potential wires arranged in 36 concentric layers, comprising a total of 5940 drift cells. Each drift cell is 18 mm by 18.8 mm with a 30 μm diameter gold-plated tungsten sense wire surrounded by 76 μm Cu-Be field shaping wires. The potential wires are under a tension of 1.1 N and the sense wires are under a tension of 0.7 N. In order to allow measurements of the z coordinate every second layer is at an alternating positive and negative stereo angle (with a stereo angle sequence of $0°, +\alpha, 0°, -\alpha$ and so on). The stereo angle α increases with the radius r as $\sqrt{r}$ from 40 mrad in the innermost layer to 80 mrad in the outermost layer, see figure 2.3.

The chamber operates at a pressure of 1035 mbar in an environment of 97 % propane (C_3H_8), 3 % methylal ($CH_2(OCH_3)_2$) and 0.2% water vapor. The water was added after discharges occurred in one of the chamber's sectors. After the addition of water the chamber cured itself and it has been operating smoothly since. The cathode wires, together with the chamber housing, are kept at a ground potential.

In order to maintain stable operation, the drift chamber is monitored and calibrated on a regular basis. Pulser runs, during which a pulse of known amplitude is fed through each ADC, are done once a day during the data collecting periods so that the calibration constants for the dE/dx measurements can be updated. In addition, daily trim runs are performed on the TDC's to maintain their time resolution and so the spatial accuracy of the chamber is maintained. Off line analysis calculates the distance of the track for each wire, by using the drift-time relation. The resolution of the drift chamber for Bhabha tracks is 190 μm and for multihadrons 220 μm (figure 2.4).

For fast particles (p > 1 GeV/c) the momentum resolution is dominated

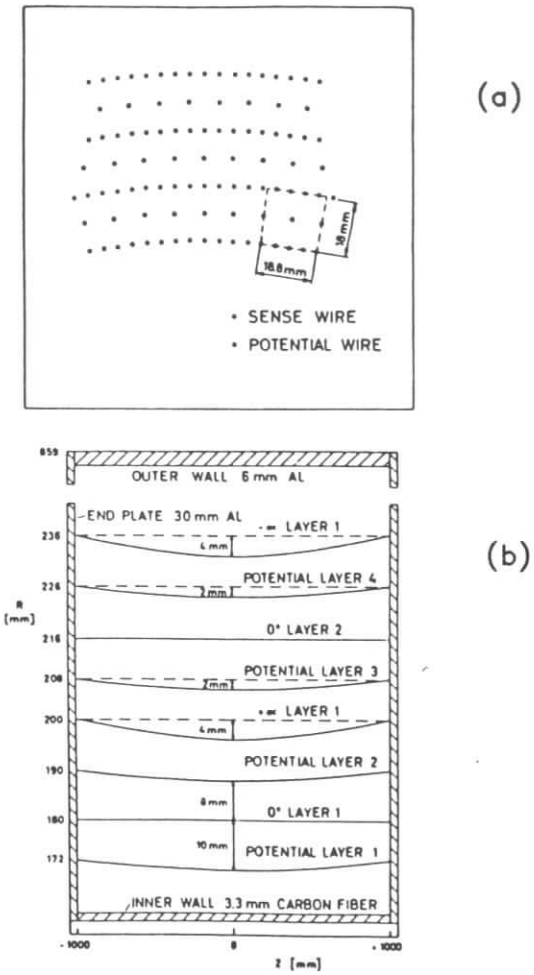

Figure 2.3: Cross sections of the Drift Chamber. a) perpendicular b) parallel to the beam axis.

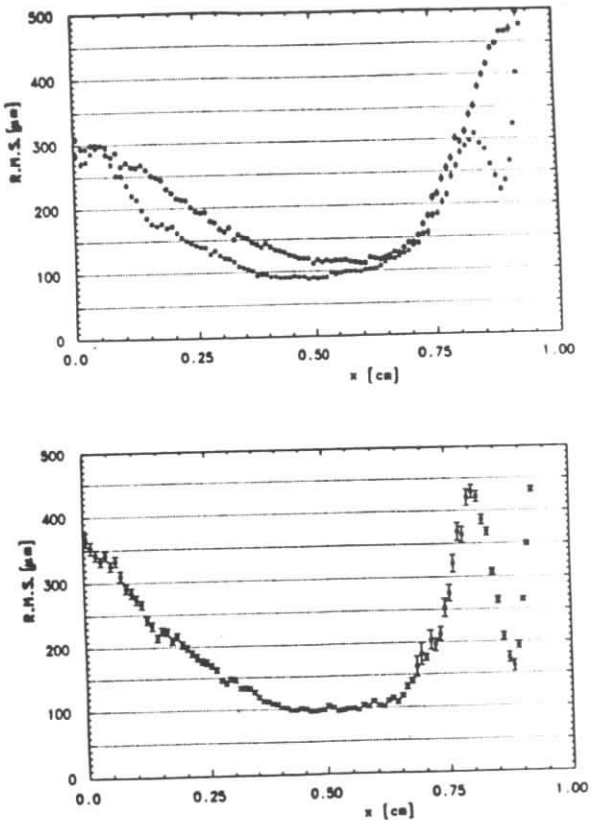

Figure 2.4: Spatial resolution of the drift chamber as a function of the distance between the track and the sense wire. a) for electron tracks from Bhabha events b) for hadron tracks. Squares are for chamber operating with water additive and circles without.

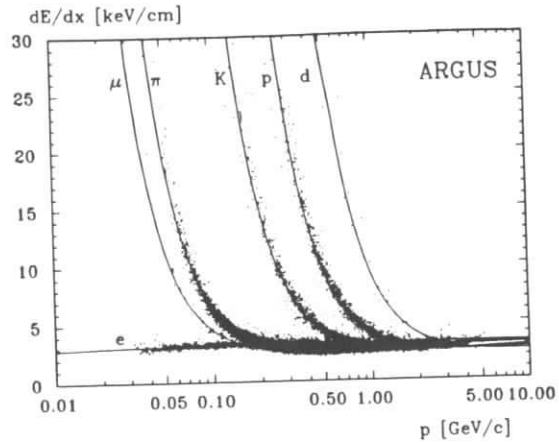

Figure 2.5: Specific energy loss versus the momentum of the particle.

by the errors of the track measurement and is given by the expression :

$$\frac{\sigma(P_T)}{P_T} = 0.009 \cdot P_T \text{ [GeV/c]} \tag{2.2}$$

For momenta below 1 GeV/c the momentum resolution is dominated by multiple scattering and can be expressed as

$$\frac{\sigma(P_T)}{P_T} = \sqrt{0.01^2 + (0.009 \cdot P_T \text{ [GeV/c]})^2} \tag{2.3}$$

The polar angle resolution is $\sigma(cot(\theta))$=0.004. The DC covers 96 % of the 4π solid angle. Figure 2.5 shows a plot of the dE/dx versus the momentum of a particle. The separation between π-K and p-K is larger than 3σ for momenta bellow 700 GeV/c and 1200 GeV/c respectively (figure 2.5).

2.4 The Vertex Drift Chamber

The ARGUS Vertex Drift Chamber (VDC) [37] allows precise measurement of a charged particle's trajectory position very close to the interaction point and so enhances the spatial resolution of the primary vertex position and the secondary vertices of particles as K^0's and Λ's. It also provides the necessary resolution to perform the lifetime measurements of charmed particles and τ-leptons.

The chamber is 1 m long, has an inner radius of 5 cm and outer of 28 cm. In order to reduce multiple scattering the inner and outer cylindrical walls are made of a carbon fibre epoxy composite (0.9 and 1.3 mm thick). The end plates are made of 2 cm thick G10 fibre glass. Brass feed throughs use a broached groove to hold the wires with a precision of 5 μm.

There are 594 gold plated tungsten sense wires with a diameter of 20 μm and 1412 Cu-Be field wires with diameters of 127 μm. They are arranged in a close packed hexagonal cell pattern to maximize the number of hits per track (figure 2.6).

The inscribed radius of a drift cell is 4.5 mm. This small cell size allows the maintenance of large efficiencies in this high track density region of the detector without resorting to the complexities and expense of multihit electronics. All the wires are parallel to the z axis so the chamber provides information only in the x-y plane.

The vertex chamber operates at a potential of –3.5 kV applied to the field wires in a pure CO_2 environment at a pressure of 1.5 bar. To prevent aging

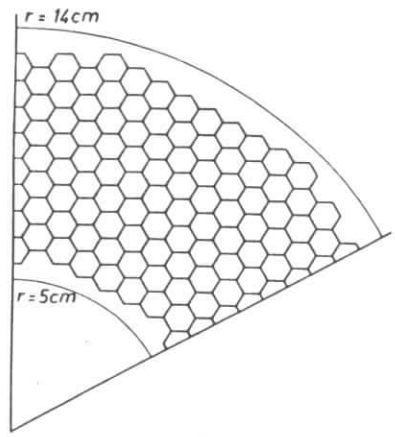

Figure 2.6: The hexagonal cell pattern of the vertex drift chamber. The sense wires are located in the center of the hexagon and the field wires on the corners.

effects (polymer deposit build up on the wires) 0.3 % water vapor is added to the VDC gas. The spatial resolution for the VDC as determined from Bhabha scattering events is shown in figure 2.7. There is a plateau with about 50 μm resolution for one third of the total drift length. For about half of the cell the resolution is better than 100 μm. Towards the sense wire the resolution deteriorates due to ionization statistics to the linear rise of the drift velocity with the electric field in CO_2. At the outer ends of the drift cell the non-circular isochrones lead to worse resolution. For the reconstruction of multihadron events the resolution has to be scaled by a factor 1.4 due to the large fraction of low momentum tracks which suffer multiple scattering.

The VDC adds 8 more layers of information to that of the main drift chamber. This leads to a great improvement of the precision on the measured parameters of charged tracks. The momentum resolution for 5 GeV/c muons

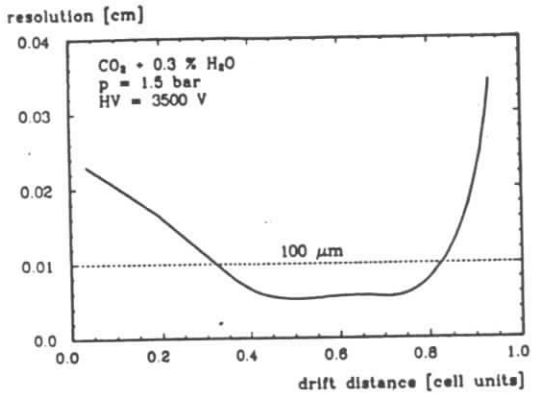

Figure 2.7: VDC resolution as a function of the drift distance.

improved from $\frac{\sigma(P_T)}{P_T} = 0.9\% \cdot P_T$ to $0.6\% \cdot P_T$. By studying the distance of closest approach between the two tracks in the Bhabha scattering events, it was found that single high momentum electron tracks can be extrapolated to the vertex with a precision better than 100 μm. The reconstruction efficiency for secondary vertices from K_s^0 and Λ decays was improved by about 60 %.

2.5 The Time of Flight System

The ARGUS Time of Flight system (TOF) [38] consists of 160 scintillation counters surrounding the drift camber. The barrel part contains 64 counters and each of the two end caps 48. They are all NE-110 type plastic scintillators. Each barrel counter is 218 cm long, 9.3 cm wide, 2 cm thick and it is read by two photomultipliers (RCA 8575), one on each end. They cover 75 % of the full solid angle. The end cap counters are wedge shaped with height 48 cm, inner

width 5.1 cm and outer width 11.4 cm. They are viewed by one photomultiplier each and cover 17 % of the full solid angle. The scintillation light travels along wave guides to photomultipliers that operate in a field free region. The analogue signals from the phototubes are split in a ratio 1:4. Eighty percent of the signal, is used to trigger a discriminator whose logical signal after being delayed by 250 ns, stops the TDC. Twenty percent of the signal, after being delayed by 250 ns, is fed to a charge sensitive ADC. The charge measurement is used for the off line correction for the time measurement by the TDC. The time of flight of a particle (ie. the time it takes to travel from the interaction point to the TOF counter) may be extracted from the measured TDC values.

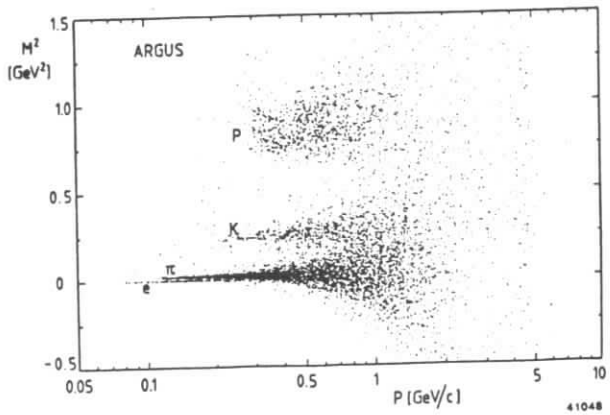

Figure 2.8: Mass squared from TOF measurements as a function of the momentum of the particle for hadron tracks.

The identification of a particle by the Time of Flight information is per-

formed by measuring its velocity β and determining its rest mass according to

$$\frac{1}{\beta} = \frac{c \cdot TOF}{l} = \sqrt{1 + \left(\frac{mc^2}{pc}\right)^2} \Rightarrow m^2 = p^2 \cdot \left(\frac{1}{v^2} - \frac{1}{c^2}\right) \tag{2.4}$$

and the mass resolution is then

$$\sigma(m^2) = 2 \cdot \left(\frac{p}{l}\right)^2 \cdot TOF \cdot \sigma(TOF) \tag{2.5}$$

which for 220 ps TOF resolution leads to 3 standard deviation π/K separation up to 0.7 GeV/c and K/p separation up to 1.2 GeV/c. A scatter plot of TOF m^2 versus p illustrating the particle separation is shown in figure 2.8.

2.6 The Electromagnetic Shower Counters

Another important component of the ARGUS detector is the electromagnetic calorimeter [39]. The ARGUS shower counters serve several purposes.

- They measure the energy of the electrons and the energy and direction of the photons.
- They provide on-line and off-line measurements of the luminosity.
- They help in the separation of electrons from muons and hadrons by the shape and the amount of energy deposited on the counters.
- They are used for the construction of the total energy trigger.

The shower counter system consists geometrically of two parts. The cylindrical barrel calorimeter which measures particles with $|\cos(\theta)| < 0.75$ and the endcap calorimeter that measures particles with $0.75 \leq |\cos(\theta)| < 0.96$. The whole calorimeter covers 96 % of the full solid angle. The barrel section consists of 1280 counters arranged in 20 rings of 64 counters each. Each of the endcaps has 240 counters divided in five rings of increasing radius with 32, 40, 48, 56 and 64 counters respectively. All counters are of alternating 5 mm scintillator - 1 mm lead. (The lead is 1.5 mm plate for the end cap calorimeter). The overall length of each counter corresponds to 12.5 radiation lengths and its width is 1 (0.9) Molliére radius for the barrel (endcap) counters.

Two types of counter shapes have been used (plane-parallel and wedge shaped) to fit in the cylindrical geometry. One shower counter module consists of two counters (one of each type) and each counter is read out by a wavelength shifter bar located between the two counters. The wavelength shifters are shielded with aluminized mylar to eliminate cross talk. The light from the wave length shifters is guided to phototubes operating in a region outside the magnetic field. Each shower counter is connected to a quartz fibre light guide to allow laser calibration pulses to reach the phototubes. The calorimeter is supported by a frame made of non-magnetic stainless steel and is located inside the magnet so the material between the interaction point and the counters is minimal.

The signals from the photomultipliers are fed into Split-Delay-Summing (SDS) units, which delay the signals by 240 ns and sum the signals from groups of 8 or 14 counters. The SDS signals are used as a part of the fast trigger (see section 2.9.1). In addition the signals from the photomultipliers are digitized and passed to the online computer provided the trigger conditions are satisfied.

The absolute energy calibration of each shower counter module is done using electrons and positrons from Bhabha scattering events. The Bhabha events are

very well defined from the beam energy. The impact points of the tracks on the shower counters are derived from the drift chamber track reconstruction.

In order to define the energy resolution for high energies, QED processes ($e^+e^- \rightarrow e^+e^-, \gamma\gamma$) were used. At low energies, measurement of the widths of the invariant mass distribution of π^0's and η's provided the resolution. The results obtained can be parametrized by the expression

$$\frac{\sigma(E)}{E} = \sqrt{(0.072)^2 + \frac{(0.065)^2}{E[GeV]}} \tag{2.6}$$

for the barrel region and by

$$\frac{\sigma(E)}{E} = \sqrt{(0.075)^2 + \frac{(0.076)^2}{E[GeV]}} \tag{2.7}$$

for the endcaps. From the study of the reaction $e^+e^- \rightarrow \gamma\gamma$ the angular resolution is also determined to be 37 mrad. Finally the detection efficiency is of the order of 98 % for 50 MeV photons.

2.7 The Muon chambers

There are three layers of muon chambers [40]. The first layer is inside the magnet yoke and has 3.3 absorption lengths between it and the interaction point, and has a lower momentum cutoff for muons of 700 MeV/c. It covers 43 % of the full solid angle. The two layers outside the yoke cover 87 % of 4π and are separated from the first layer with an additional 1.8 absorption lengths of material. These two outer layers have a 93 % overlap and a lower momentum cutoff of 1100 MeV/c.

Each chamber consists of eight proportional tubes glued together. Each tube is made of aluminium with internal cross section of 56 x 56 mm^2 and 2 mm wall thickness. The tubes operate with a gas mixture of 92 % Argon and 8 % propane at a high voltage of 2.35 kV. Offline analysis from cosmic muons showed that the muon chamber efficiency is (97.8 $\pm$ 0.01) %.

2.8 DATA Flow

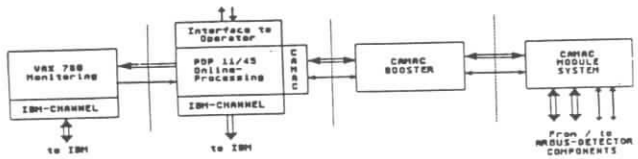

Figure 2.9: The data-flow diagram.

The data flow diagram is shown in figure 2.9. The triggered events are passed to a CAMAC system which digitizes them. It consists of three branches, one for the main drift chamber, a second one for all the remaining detector components and a third one which contains the equipment for monitoring the detector performance. Then the events are transferred to a PDP 11/45 computer via a LeCroy CAMAC Booster (CAB) which reduces the processing time to 3 ms/event. The PDP 11/45 supervises the readout. It is also used to start and stop runs, and run the calibration programs such as the laser monitor for the shower counters and the TOF system.

Assembled events are afterwards sent via a pair of DR11-W parallel ports

to a VAX 11/780 computer which has as its primary task the monitoring of the detector performance by filling histograms of various quantities of interest. This way problems with the detector can be easily spotted and cured.

Finally the VAX sends the data to the DESY main frame IBM computer (an IBM 3089Q main frame and an IBM 3090 vector processor) via a PADAC serial link. In the case of a failure of the IBM link system, the VAX disk is capable of storing several hours worth of data which can be transferred later on the IBM.

2.9 The ARGUS Trigger

The bunch crossing frequency of DORIS II is 1 MHz so the detector electronics have 1 μs to decide whether to accept an event or not and be ready to get the next event. This decision is made at two trigger levels. In a first stage a fast pretrigger discriminates background from "good" candidates within 300 ns. A slower second stage trigger, the " Little Track Finder ", makes the final decision for the event.

2.9.1 The Fast Pretrigger

The fast pretrigger uses only the TOF and shower counter information. For the trigger conditions the TOF and the shower counter planes are divided into two hemispheres separated by the z=0 plane.

The output signals from the shower counter phototubes are summed by the Split-Delay-units (SDS). Each SDS unit sums the output of two neighboring raws of counters (22 counters) along the z-axis in one hemisphere. The end caps are divided into 16 sectors each, with 14 counters for each of the 8 wedge sectors and 8 counters for each of the filler sectors (figure 2.10). The end cap

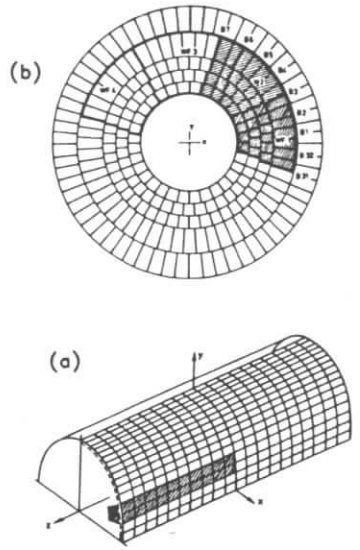

Figure 2.10: Basic Trigger unit (shaded) a) barrel b) endcaps.

information is used only for the total energy trigger and the online luminosity monitor. For all the other triggers only the barrel signals are used.

The TOF counters require coincidence of the signals of the two phototubes. The end cap TOF counters are used only for the online luminosity monitor.

There are 6 fast pretriggers using the information of the SDS units and the TOF counters :

- The total energy trigger (ETOT) uses only the shower counter information and requires the total energy deposition in either hemisphere to be greater than 700 MeV. The total energy deposition also gives online information

for the background and the rate of this signal correlated to the bunch crossing gives information for the running condition of the storage ring.

- The High Energy SHower trigger (HESH) searches for events with single particles that carry a large portion of the total energy. It sums the SDS units in each hemisphere in groups of five units with one unit overlap between neighboring groups. In total there are 16 HESH trigger groups, each covering about 70° in azimuth. The event is accepted if one HESH group exceeds a preset threshold which corresponds to about 1 GeV.

- The Charged Particle PreTrigger (CPPT) requires at least one track in each hemisphere without any requirement for azimuthal angular correlation. A track is defined by the coincidence of an overlapping TOF and a shower counter group. Three SDS units (six rows of shower counters) form one shower counter CPPT group, while four TOF counters make a TOF CPPT group (figure 2.11). Each CPPT group has one SDS unit in common with its neighbor. There are 16 CPPT groups per hemisphere. The CPPT trigger requires a hit in any of its TOF counters in coincidence with a minimum energy deposition of 50 MeV in the three SDS groups of the CPPT group for each of the hemispheres.

- The Coincidence MATRIX trigger (CMATRIX) requires a coincidence of two CPPT groups with at least 90° azimuthal separation but not necessarily in opposite z hemispheres. The CMATRIX units are flexible and can easily be changed to expand or contract the angular separation.

- The Cosmic trigger accepts cosmic muons that travel close to the beam pipe by requiring a coincidence between two opposite groups of four barrel TOF counters. This trigger is made in order to test and calibrate various detector components when the storage ring is not operating. The cosmic trigger is turned off during the normal data taking.

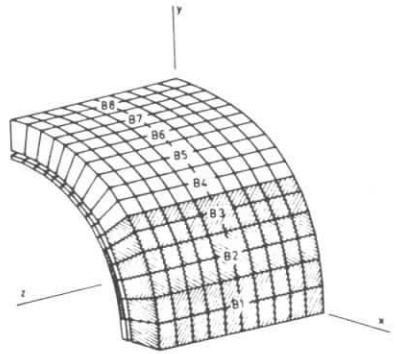

Figure 2.11: The CPPT group.

- Another trigger is the random trigger which gives a random gate with a rate of 0.1 Hz to all the electronics. This trigger helps to monitor the random noise.

The total trigger rate is about 100 Hz and must be in coincidence with the bunch crossing signal and the "trigger ready" signal given by the online computer. For the proper operation all the trigger components are checked 3-4 times a day by programmable test signals with adjustable heights to all the SDS units and to all the Split-and-Delay units of the TOF system.

2.9.2 The Second Level Trigger (LTF)

The Little Track Finder (LTF) is a second level trigger [41] and it is started by the fast pretrigger. It uses the information from the main drift chamber and the TOF counters looking for tracks in circular paths passing through the

interaction point. The LTF is designed so that it will introduce the minimum possible dead time into the data taking process. A fast hardware procedure would be too inflexible whereas a flexible software procedure would be too slow. As a compromise the LTF was built as a table-driven Emitter-Coupled-Logic (ECL) device that is connected between the main trigger logic and the CAMAC system.

Each primary trigger initializes the LTF and the hits of the DC and the TOF system are transferred online into bitwise addressable memories. Another memory is preloaded with a list of all possible tracks (2000 masks in total). The entries of the hit memories are compared with the mask lists. Each time a match between the two is found a count is incremented until a certain threshold is reached. If all the masks have been compared and the track counter does not pass the preset threshold, a fast clear is distributed to the readout system and the event is skipped. Suitable ordering of the masks helps the system to skip useless cycles.

The operation of the LTF depends on the number of hits in the DC. The measured mean operation time of the LTF during normal detector running is about 20 μs. The LTF introduces about 0.2 % dead time into the detector operation for an average pretrigger rate of 100 Hz and has a track finding efficiency about 97 % which mainly depends on the DC efficiency.

During normal running conditions 2 LTF tracks are required with each of the CPPT and CMATRIX petriggers, and 1 LTF track with the HESH pretrigger. For running periods with high background rate the LTF threshold is raised by one track for the CPPT and CMATRIX pretriggers. The LTF requirement reduces the final trigger rate to about 10 Hz.

2.10 Luminosity Monitoring

Bhabha scattering is used for online luminosity monitoring. The luminosity, $\mathcal{L}$, can be determined by the expression:

$$\frac{dN_{Bhabha}}{dt} = \mathcal{L} \cdot \sigma_{Bhabha} \tag{2.8}$$

N_{Bhabha} is determined online by requiring a coincidence between a shower counter and the TOF group in front of it. The grouping is similar to that of the CPPT in the barrel region. The energy deposit in the shower counters is required to have a minimum of 1 GeV. A Bhabha count is recorded if there is a coincidence signal with the same criteria in the opposite group in the other end cap. By using (2.8) the counts are converted to luminosity.

A more precise luminosity measurement is done off-line by fully reconstructed Bhabha events in the barrel region.

2.11 Event Reconstruction

When the raw data reach the IBM they consist of the ADC and TDC hit information of the various detector components. The raw data must be reconstructed into the kinematic variables of the event, such as particle tracks, momenta, vertices, χ^2's for different particle hypotheses etc. This task is accomplished by an analysis program.

2.11.1 Drift Chamber reconstruction and Pattern recognition

A charged particle transversing a homogeneous magnetic field follows a helical trajectory. The magnetic field is parallel to the z-direction, so the trajectories

of charged particles can be described by a circle in the x-y plane in a dition to their motion on the z-direction. It is convenient to describe these orbits by a set of 5 parameters.

- κ : the curvature of the helix
- d_0 : the distance of closest approach of the track to the innermost hit wire in the DC, measured in the x-y plane.
- z_0 : the z-coordinate of the above distance
- ϕ_0 : the azimuthal angle of the track
- $cot\theta$: the cotangent of the angle of the track with respect to the z-axis

The track reconstruction follows a two step procedure. In the first step a search for tracks in the x-y plane defines the parameters κ, d_0 and ϕ_0 by using the paraxial wires. In a second step the information of the stereo wires is used to the find $cot\theta$ and z_0 and finally make the three dimensional reconstruction of the track.

At the start of the search for tracks in the x-y plane (1st step) the program looks for neighboring pairs of hits and adds a third hit (since 3 points define a circle) to determine the curvature κ from the wire position. A single triplet of hits does not yet contain any information as to whether the hits are coming from a track candidate or not. As a minimal requirement a matching fourth hit must be found. For this the initial triplet is extended by combining a fourth hit to the original three. The curvature of the newly formed triplet is calculated. If the difference in κ between the initial and the new triplet is sufficiently small the four hits are assumed to form a track candidate, with the new curvature taken as the average of the two calculated curvatures. The track candidate is then extended by adding a fifth hit with two of the previously found hits and

so on. In reality the procedure is more complicated since we do not have points to fit but circles which represent isochrones around the hit wires. The particle's trajectory is then a segment of a large circle tangential to these small circles. In this case the left-right ambiguity must be taken into account. The actual space-time relation, rather than the wire positions, are used.

Once we find κ, the track projection is described by a circle which must match two pairs of points far from one another. From that the ϕ_0 and d_0 may be defined. An additional cut which requires that there must be at least two tracks with $d_0 < 1.5cm$ has to be fulfilled for the event to be accepted.

After the two-dimensional pattern recognition is complete, the parameters z_0 and $cot\theta$ remain to be found. This is done by using the stereo wire information. The x-y pattern recognition constrains the track to the surface of a cylinder parallel to the z-axis. Neglecting the drift times, the intersection of the cylinder with the stereo wires gives a sequence of z-values. A procedure similar to the one described above reconstructs the track in the z-direction after the drift times and the left-right ambiguity are included. An event is accepted if there are at least two tracks with $z_0 < 8cm$ in addition to having $d_0 < 1.5cm$. A minimum of 4 z-wires and 3 stereo wires are needed to determine a track.

After the drift chamber analysis has been done, the vertex chamber information is added. For the vertex chamber the pattern recognition uses the track parameters from the main DC fit. The tracks are traced back into the VDC and hits on these "roads" are assigned to the track. The track parameters are updated after the track fit procedure is repeated with the additional information.

2.12 Particle Identification

The charged particle identification in ARGUS is done by using the specific energy loss due to ionization in the drift chamber (dE/dx measurement) and the Time-of-Flight measurement. These, in combination with the momentum measurement from the drift chamber, allow the mass reconstruction of the particle.

To identify leptons there are other independent methods. Muons with momentum greater than 700 MeV/c are identified by the muon counters and electrons by the energy deposited in the electromagnetic calorimeter. The shower counters also provide a powerful tool for the antiproton identification due to the enormous energy deposit produced by the strong annihilation process.

The specific ionization loss of a particle of charge $z_{inc}e$ transversing a medium is given by the Bethe-Bloch formula

$$\frac{dE}{dx} = \frac{D \cdot Z_{med} \cdot \rho_{med}}{A_{med}} \left[\frac{z_{inc}}{\beta}\right]^2 \times \left[ln\left(\frac{2m_e\gamma^2\beta^2c^2}{I}\right) - \beta^2 - \frac{\delta}{2} - \frac{c}{Z_{med}}\right](1+\nu) \qquad (2.9)$$

where $D = 4\pi N_A r_e^2 m_e c^2 = 0.3070$ MeV $\cdot\, cm^2/g$, Z_{med} and A_{med} are the charge and mass numbers of the medium, ρ_{med} the density of the medium and I, δ, c and ν are phenomenological functions [42].

From this formula it is obvious that the dE/dx depends on the velocity of the incident particle. Combined with the momentum of the particle, this provides information about the mass of the particle.

In the reconstruction software, five particle hypotheses are used: *electrons*, *muons*, *pions*, *kaons* and *protons*. For each particle hypothesis, the theoretically expected dE/dx^{th} is compared with the measurement by orming a χ^2

$$\chi_i^2(dE/dx) = \frac{\left(\frac{dE}{dx} - \frac{dE}{dx_i^{th}}\right)^2}{\sigma_{dE/dx}^2 + \sigma_{th}^2} \qquad (i = e, \mu, \pi, K, p) \qquad (2.10)$$

where dE/dx is the measured specific ionization energy loss, dE/dx_i^{th} the theoretically expected one for particle i, σ_{th} the uncertainty of the theoretical dE/dx due to the uncertainty of the momentum measurement and $\sigma_{dE/dx}$ the uncertainty of the measured dE/dx.

Equivalently, in the case of the time of flight measurement, a χ^2 is formed for each of the above particle hypotheses

$$\chi_i^2(TOF) = \frac{\left(\frac{1}{\beta} - \frac{1}{\beta_i^{th}}\right)^2}{\sigma_{TOF}^2 + \sigma_{th}^2} \qquad (i = e, \mu, \pi, K, p) \qquad (2.11)$$

where β is the velocity of the particle as measured by the time of flight system, β_i^{th} the expected velocity for the particle i knowing its momentum, σ_{TOF} and σ_{th} are the uncertainties of the measured and expected velocities.

The TOF and dE/dx χ^2's are then combined into one χ^2

$$\chi_i^2 = \chi_i^2(\frac{dE}{dx}) + \chi_i^2(TOF) \qquad (2.12)$$

which is used to form a likelihood function

$$L_i = exp(\frac{-\chi_i^2}{2}) \qquad (i = e, \mu, \pi, K, p) \qquad (2.13)$$

out of which the normalized likelihoods λ_i are constructed

$$\lambda_i = \frac{w_i \cdot L_i}{\sum_k w_k \cdot L_k} \qquad (i = e, \mu, \pi, K, p) \tag{2.14}$$

where w_i are the relative production rates introduced from a priori knowledge of the particle abundance. The analysis presented in this thesis used 1:1:5:1:1 for $w_e : w_\mu : w_\pi : w_K : w_p$.

The dE/dx and TOF measurements can give good identification for hadrons up to ~ 1 GeV/c and for electrons up to ~ 230 MeV/c. For electrons the identification is considerably improved by adding the shower counter information into a likelihood similar to the one described above. The normalized likelihood for the electrons has the form

$$\lambda_e = \frac{w_e \cdot \prod_i P_i^e(x)}{\sum_k w_k \cdot \prod_i P_i^k(x)} \tag{2.15}$$
$$i = dE/dx, TOF, SC \qquad k = e, \mu, \pi, K, p$$

where $P_i^k(x)$ is the probability that a track with measured parameters x be identified as a particle of type k by the device i, and w_k is the relative production rate as above. The likelihood λ_e takes values between 0 and 1 and has an electron selection efficiency greater than 90 % for all momenta above 500 MeV/c.

For muons another likelihood is defined by adding the information of the muon chambers. The normalized likelihood for the muons has the form

$$\lambda^\mu = \frac{w^\mu \cdot \prod_i P_i^\mu(x)}{\sum_k w^k \cdot \prod_i P_i^k(x)} \tag{2.16}$$
$$i = dE/dx, TOF, SC, \mu C \qquad k = e, \mu, \pi, K, p$$

The μ-π misidentification probability is (2.2 $\pm$ 0.2) % per pion and the μ-K (1.9 $\pm$ 0.5) % per kaon.

2.13 The KAL Program

For the physics analysis a specially designed program, KAL (Kinematical Analysis Language), is used. The main frame of KAL is written in FORTRAN77. KAL processes events in a mini DST format and may be used to perform the tasks required for the physics analysis, such as the identification of a particle, making the invariant mass combinations, calculating kinematical quantities for different particle systems and also making histograms of these quantities. The user is not required to write FORTRAN code but rather uses KAL statements. This way the user is more focused on the physics analysis rather than programming.

The first step of KAL is particle identification, during which the program calculates the different likelihood hypotheses (see section 2.12) for each track the *a priori* relative particle abundance supplied by the user. To make the invariant mass combinations a statement is used to select the desired particle combinations and then all the kinematical quantities of the composite particle are available. KAL also has the possibility to interface with a FORTRAN subroutine supplied by the user according to his needs.

2.14 Monte Carlo simulation

In order to estimate the detector acceptance a Monte Carlo simulation was developed. The detector simulation program, SIMARG [43], is based on the CERN program GEANT [44]. SIMARG reads a generated event and follows each track in the detector by simulating the interactions using theoretical models. For electromagnetic interactions the EGS program [45] is used and for the hadronic interactions routines from the program GHEISHA [46]. The dE/dx simulation is made by using energy loss spectra as measured in a smaller pro-

totype of the actual chamber. This way the dE/dx simulation is completely independent of the different theoretical models for the energy loss spectrum. The final dE/dx values are converted to ADC channels. The simulation of the drift times is made according to the measured time-space relations and the final result is given in TDC units. Finally the event is written to the output file in raw data format. This file also contains the generated event information. The full detector Monte Carlo simulation has the following essential steps :

- Generate an event [see section 3.6].
- Pass the event through SIMARG and write the digitized output.
- Process the event through the reconstruction program, applying efficiencies and smearing according to the resolution of the various detector components.
- Pass the event through a trigger simulation program.

2.14.1 The Trigger Simulation

For events with low multiplicity, asymmetric topology or low visible energy, it is essential to know the trigger conditions accurately in the acceptance calculation. For this purpose a program was developed, which processes the reconstructed Monte Carlo events and simulates the ARGUS trigger conditions (section 2.9).

The ARGUS history is divided into several trigger periods according to the different thresholds, logic and LTF efficiencies. In a first step the program calculates the integrated luminosity for each of these trigger periods according to the user's requirements. Then, it sums the shower counter pulse heights for each trigger element and determines the LTF masks from the drift chamber TDC hits. Next, the program loops over all the trigger periods and simulates

which triggers are set in each period. This loop is usually repeated several times to minimize the fluctuations. At the end, the program returns a trigger weight for each event. This information can be either dumped on a separate file or included in the Monte Carlo event bank, according to the needs of the user.

For each trigger period and trigger type, the trigger thresholds were determined from the data, by using the actual trigger information and the calibrated pulse heights. A 2 % smearing was introduced in the threshold shapes to account for the uncertainty in the deposited energy determination.

The LTF efficiency is defined as the probability for a charged particle to be assigned one or more LTF tracks if it hits a TOF counter. Bhabha events, when the ETOT trigger is set, are ideal to determine the LTF efficiency since they don't require an LTF signal. The LTF finding algorithm uses a drift chamber efficiency of 100 % and, in order to reproduce the experimentally observed efficiency, the program discards masks randomly.

The trigger simulation reproduces well the actual trigger efficiencies. For example the CPPT thresholds were determined from events with an ETOT trigger set, leading to a CPPT efficiency for dimuon events of 95 %. The corresponding trigger simulation agrees within 1 %. Another check was done by comparing Monte Carlo events simulating the reaction $\Upsilon(2S) \rightarrow \Upsilon(1S)\pi^+\pi^-$ with the $\Upsilon(1S)$ decay invisible to the detector and data for the reaction $\Upsilon(2S) \rightarrow \Upsilon(1S)\pi^+\pi^-$, with the $\Upsilon(1S) \rightarrow e^+e^-$, where one of the electrons set the ETOT trigger. To calculate the efficiency, the fraction of events where the pions set a trigger in the data was compared with the trigger simulation for the Monte Carlo events. The two numbers were identical.

To calculate the systematic error introduced by the trigger program, the thresholds were varied simultaneously by $\pm 10\%$. The systematic error was found for $\gamma\gamma \rightarrow 2\pi^+2\pi^-2\pi^0$ events to be about 5 % and for $\gamma\gamma \rightarrow \pi^+\pi^-2\pi^0$ events 5.5 %. The program is developed in such a way that it can be used by

non-experts. Appendix C describes the routines with which the user can supply his requirements to the program.

Chapter 3

Data Analysis

3.1 Data Samples

The results presented in the following chapters are based on data collected in the period from 1983 to 1986. The data correspond to three data taking periods named within the collaboration as experiments 2,4 and 5.

Running Period	Integrated luminosity $[pb^{-1}]$
Experiment 2	62.8
Experiment 4	69.9
Experiment 5	101.6
Total	234.3

Table 3.1: Integrated luminosity collected with the ARGUS detector in the different running periods.

The integrated luminosity for each period is summarized in Table 3.1. The data for experiment 2 were taken without the VDC, whereas for experiments 4 and 5 the VDC was installed in the detector. These reconstructed data sets, the DST's, were divided in two sections, the multihadron events (MUHA) and the two-prong events (TWOP). The multihadron selection criteria are

- at least three reconstructed tracks in the main drift chamber with total energy deposited in the calorimeter greater than 1.7 GeV.
- at least three tracks that are within 1.5 cm of the primary vertex in the $x-y$ plane and within 8.0 cm along the z-axis.

These criteria select about 5% and 30% of the total $2.7 \cdot 10^7$ reconstructed events as MUHA-candidates respectively. For the two-prong events the selection criteria are:

1. there are exactly two tracks with opposite charge;
2. these tracks have to point to the main vertex within 1.5 cm in the $x-y$ plane and 6 cm in the z-axis;
3. the angle between the two tracks must be less than 165°;
4. one track must have shower energy less than 1.5 GeV, or momentum less than 3.0 GeV and shower energy less than 4.0 GeV;
5. $|\theta| > 30°$ where θ is the angle of the track with the z-axis

The criteria 3-5 reject the Bhabha events. After these selection criteria about $3.1 \cdot 10^6$ two-prong events remained.

3.2 Event Selection

In the following sections, the event selection for the two channels studied in this thesis is described. In the case of the non-tagged events one measures only the final state X and not the scattered electrons. The two-photon events have a unique feature that makes them easier to distinguish from annihilation events. The total transverse momentum, P_T^{tot}, of the final state X peaks at low values. The P_T^{tot} is defined as $P_T^{tot} = |\sum \vec{P}_{Ti}|$, where the sum runs over each individual

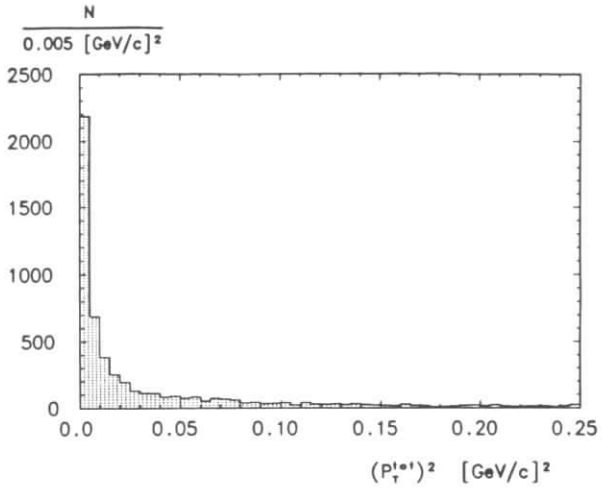

Figure 3.1: $(P_T^{tot})^2$ for Monte Carlo generated events of the type $\gamma\gamma \to \pi^+\pi^-\pi^0\pi^0$.

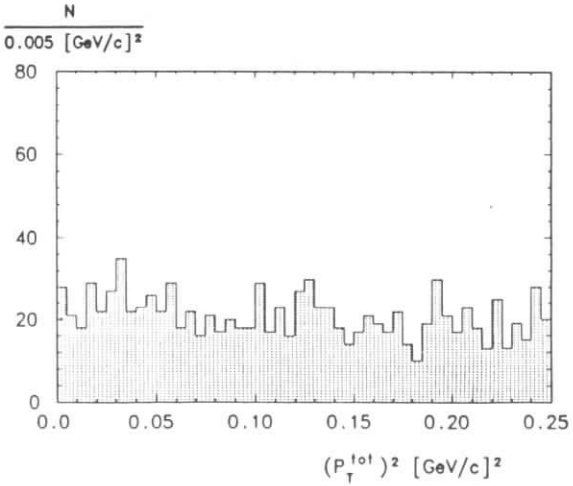

Figure 3.2: $(P_T^{tot})^2$ for events containing five charged tracks in the data.

particle i of the final state. The $(P_T^{tot})^2$ distribution peaks strongly at zero as one can see in figure 3.1 where the $(P_T^{tot})^2$ for Monte Carlo generated events of the type $\gamma\gamma \to \pi^+\pi^-\pi^0\pi^0$ is plotted. In reality there is some background in this distribution from incompletely reconstructed events and events with τ-pairs. The $(P_T^{tot})^2$ distribution for incompletely reconstructed events from the data is shown in figure 3.2. This background can be parametrized by a straight line. A cut on the P_T^{tot} distribution enhances the two photon events in a data sample and suppresses the background.

3.3 The Reaction $\gamma\gamma \to 2\pi^+2\pi^-2\pi^0$

Candidate events for the reaction $\gamma\gamma \to 2\pi^+2\pi^-2\pi^0$ were selected from the multihadron (MUHA) data samples and had to fulfil the following criteria:

- four charged particles with zero net charge which fit to a common event vertex
- these particles had to be identified as pions by requiring the pion likelihood ratio (see section 2.12) for each one of them to be greater than 5%
- exactly four photons had to be detected by the electromagnetic calorimeter with minimum energies 50 MeV for experiments 2 and 5 and 70 MeV for experiment 4. The different cut for the minimum energy of the photons for experiment 4 was motivated from the fact that this cut gave a better signal to background ratio for the ω-meson peak in the study of the $\omega\omega$ production which is described in later sections.
- any two photons with an invariant mass between 60 and 220 MeV/c^2 were considered as π^0 candidates. To suppress combinatorial background the two photons had to have opening angles less than 90°. The invariant mass

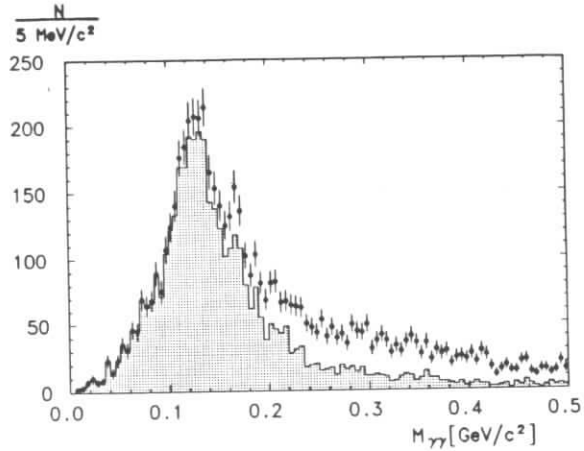

Figure 3.3: Invariant mass of the two photons for $\gamma\gamma \to 2\pi^+2\pi^-2\pi^0$ events. The dots represent the invariant mass of all photon pairs and the histogram of the pairs with opening angle less than 90° for data.

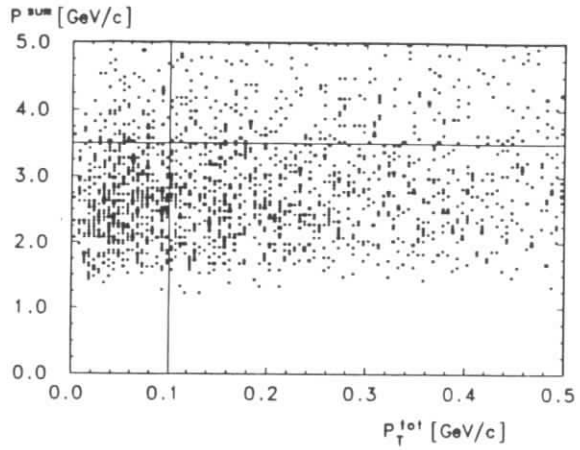

Figure 3.4: P_T^{tot} versus the scalar momentum sum for event candidates for the reaction $\gamma\gamma \to 2\pi^+2\pi^-2\pi^0$.

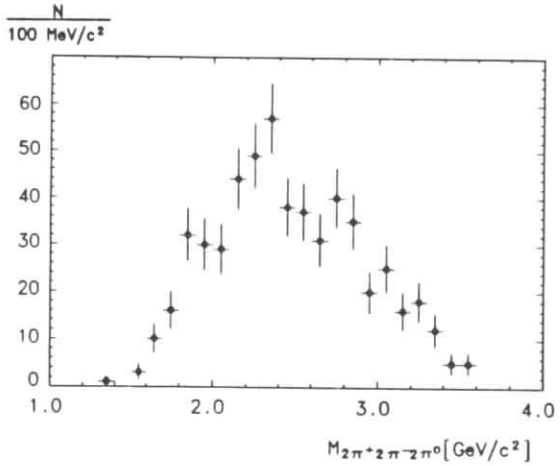

Figure 3.5: Invariant mass of $2\pi^+2\pi^-2\pi^0$

of the two photons with and without the opening angle cut is shown in figure 3.3 as open and shaded histogram respectively for data. Finally the π^0 candidates were subjected to 1-C fit to the nominal π^0 mass.

- at least two π^0 candidates were required in an event. The π^0 candidates were not allowed to have common decay photons.

- the total transverse momentum, $P_T^{tot} = \mid \sum \vec{P}_{Ti} \mid$, had to be less than 100 MeV/c and the sum of the scalar momenta $P_{sum} = \sum \mid \vec{P}_i \mid$ less than 3.5 GeV/c. The P_T^{tot} versus the P_{sum} scatter plot is shown in figure 3.4.

After these selection criteria, 553 candidate events for the reaction $\gamma\gamma \to 2\pi^+2\pi^-2\pi^0$ remain. The invariant $2\pi^+2\pi^-2\pi^0$ mass distribution is shown in figure 3.5.

3.4 The Reaction $\gamma\gamma \to \pi^+\pi^-\pi^0\pi^0$

Candidate events for the reaction $\gamma\gamma \to \pi^+\pi^-\pi^0\pi^0$ were selected from the two-prong data sets by imposing the following selection criteria :

- Two oppositely charged particles had to originate from a common event vertex. No other charged particles were allowed in the detector.

- The two charged particles had to be identified as pions with likelihood ratios larger than 5%.

- Exactly four photons were required with minimum energies of 50 MeV.

- At least two π^0 candidates were required. The π^0 candidates were defined as combinations of two photons with invariant masses between 60 and 220 MeV/c^2 and opening angle between the two photons smaller than 90° in order to reduce combinatorial background. The π^0 candidates were

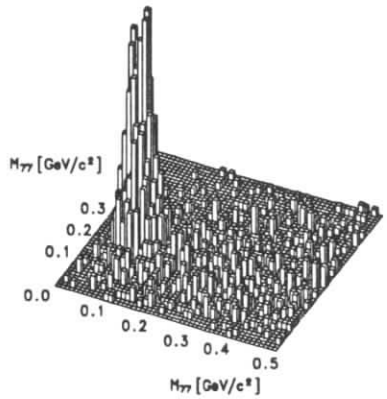

Figure 3.6: Invariant mass of two photons versus the invariant mass of the remaining photons for the $\gamma\gamma \to \pi^+\pi^-\pi^0\pi^0$ data.

constrained to the π^0 mass by a kinematical fit. The scatter plot of the invariant mass of any two photons versus the invariant mass of the remaining two photons is shown in figure 3.6. An enhancement of events is clearly discernible in the $\pi^0\pi^0$ region. This indicates the existence of events with two π^0-mesons.

- The total transverse momentum of an event was required to be $P_T^{tot} \leq$ 100 MeV/c and the scalar momentum sum $P_{sum} \leq$ 3.5 GeV/c. The scatter plot of the P_T^{tot} versus P_{sum} is shown in figure 3.7.

1290 events survived these selection criteria and their invariant mass is shown in figure 3.8.

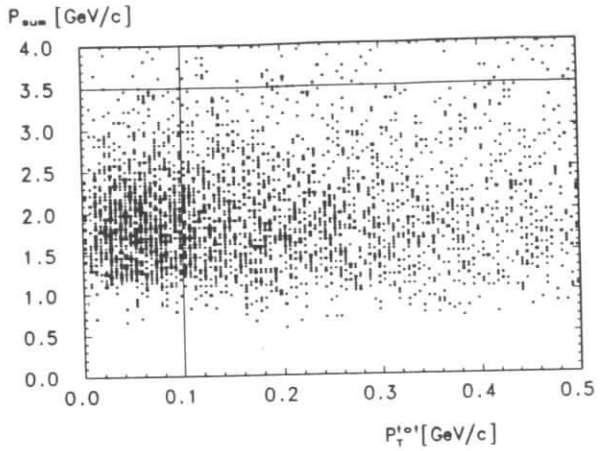

Figure 3.7: P_T^{tot} versus the scalar momentum sum for events candidates for the reaction $\gamma\gamma \to \pi^+\pi^-\pi^0\pi^0$.

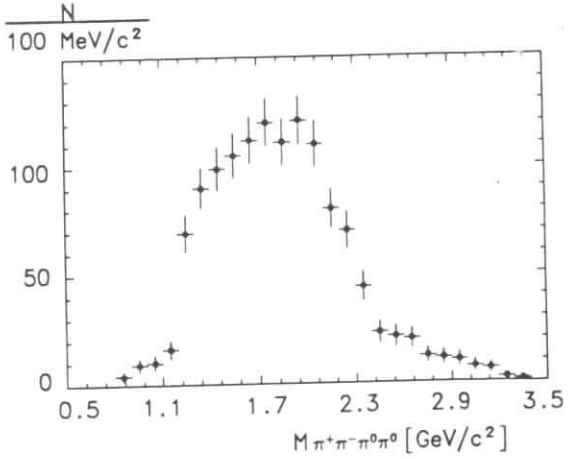

Figure 3.8: Invariant mass of $\pi^+\pi^-\pi^0\pi^0$.

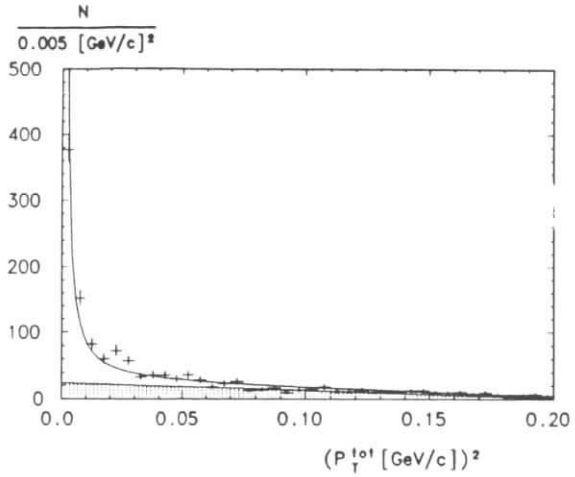

Figure 3.9: $(P_T^{tot})^2$ for $2\pi^+2\pi^-2\pi^0$ (data). The fit is described in the text and the shaded area represents the estimated background.

3.5 Backgrounds

Both reactions have the same type of background events, therefore the background studies are presented together. The main backgrounds for both reactions are:

- incompletely reconstructed events which are events where the missing momentum is carried by undetected particles.
- events of the type $e^+e^- \to \tau^+\tau^-$, where the two τ's decay to one and three prongs respectively and may contribute to the background for the reaction $\gamma\gamma \to 2\pi^+2\pi^-2\pi^0$. If they both decay to one prong they may contribute to the background for the reaction $\gamma\gamma \to \pi^+\pi^-\pi^0\pi^0$. In both cases the missing momentum is carried by the undetected neutrinos.

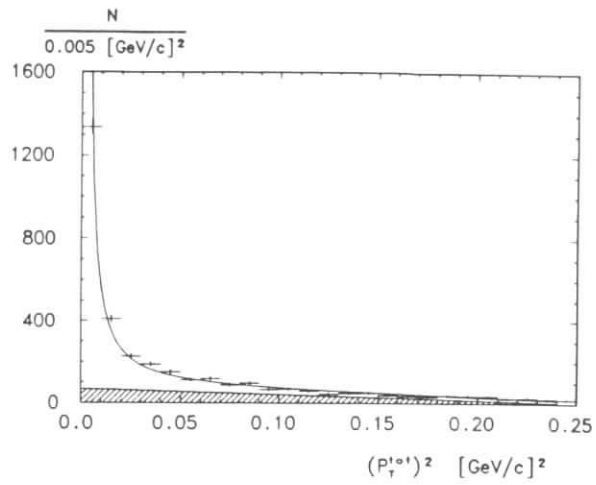

Figure 3.10: $(P_T^{tot})^2$ for $\pi^+\pi^-\pi^0\pi^0$ (data). The shaded area represents the estimated background.

These backgrounds can be estimated by studying the $(P_T^{tot})^2$ distribution. For this purpose the $(P_T^{tot})^2$ distribution for Monte Carlo generated events was fitted with a function of the form $A(1 + B/x + C/x^2)$. This way the constants B and C are determined. Then the data are fitted to this distribution with B and C fixed from Monte Carlo and including an additional linear term to parametrize the background. The $(P_T^{tot})^2$ distribution for the data with the corresponding fits is shown in figure 3.9 for the reaction $\gamma\gamma \to 2\pi^+2\pi^-2\pi^0$, and in figure 3.10 for the reaction $\gamma\gamma \to \pi^+\pi^-\pi^0\pi^0$. With this procedure 27 events are estimated to be background for the reaction $\gamma\gamma \to 2\pi^+2\pi^-2\pi^0$ and 53 events for the reaction $\gamma\gamma \to \pi^+\pi^-\pi^0\pi^0$. Incompletely reconstructed events are the main contribution to these numbers.

Another background source is noise in the electromagnetic calorimeter that fakes photons. The noise in the calorimeter was estimated by studying the

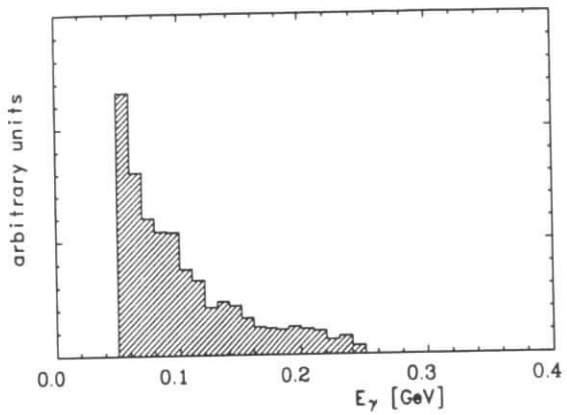

Figure 3.11: The energy distribution of random noise in the calorimeter.

reaction $\Upsilon(1S) \to l^+l^-$, where $l = e, \mu$ and by counting the fake photons in the calorimeter. The $\Upsilon(1S)$ was tagged by the pions from the transition $\Upsilon(2S) \to \pi^+\pi^-\Upsilon(1S)$. The noise distribution is shown in figure 3.11. This random noise was included in the Monte Carlo simulation.

For the final state $2\pi^+2\pi^-2\pi^0$, noise in the calorimeter could fake an event in the following ways:

- a real two photon interaction event of the type $\gamma\gamma \to 2\pi^+2\pi^-\pi^0$ with an additional two noise photons in the calorimeter that fake a second π^0. To estimate this background Monte Carlo events of the type $\gamma\gamma \to 2\pi^+2\pi^-\pi^0$ were generated and, while simulating the random noise, we tried to reconstruct the $2\pi^+2\pi^-2\pi^0$ final state. This study showed that this kind of background is negligible;

- events coming from the reaction $\gamma\gamma \to 2\pi^+2\pi^-2\pi^0$ itself, where one photon escapes detection and is replaced by a simultaneous noise photon in the calorimeter. Monte Carlo analysis estimated this background to contribute 36 events.

Another possible background to the $2\pi^+2\pi^-2\pi^0$ production is events of the type $\gamma\gamma \to 2\pi^+2\pi^-3\pi^0$ where one π^0 escapes detection. Since no evidence for this reaction was found in the data, it is concluded that this background is negligible.

Similarly, the noise contribution to the background was studied for the reaction $\gamma\gamma \to \pi^+\pi^-\pi^0\pi^0$. Background from the reaction $\gamma\gamma \to \pi^+\pi^-\pi^0$ where two noise photons fake an additional π^0 was found to be negligible. The absence of events of the type $\gamma\gamma \to \pi^+\pi^-\pi^0\pi^0\pi^0$ showed that the background from this channel, where one of the π^0's is undetected, is negligible too. In the case of real $\pi^+\pi^-\pi^0\pi^0$ events where one photon is lost and replaced by a fake photon in the calorimeter the background is 59 events.

3.6 Monte Carlo Event Generation

One of the goals of this thesis is to measure the cross sections for the two-photon production of six and four pions respectively. The data sets, after application of the selection criteria, provide the number of observed events N as a function of $W_{\gamma\gamma}$. The number of measured events N in a range $\Delta W_{\gamma\gamma}$ corresponding to an integrated e^+e^- luminosity $\mathcal{L}_{\rm int}$, is

$$N(W_{\gamma\gamma}) = \mathcal{L}_{\rm int} \int_{\Delta W_{\gamma\gamma}} \mathcal{A}\, d\sigma_{e^+e^- \to e^+e^- X} \tag{3.1}$$

where $\mathcal{A}$ is the detector acceptance for the final state X in the $W_{\gamma\gamma}$ bin. By using formula 1.12 this expression can be rewritten as:

$$N(W_{\gamma\gamma}) = \mathcal{L}_{\rm int} \int_{\Delta W_{\gamma\gamma}} \mathcal{A} \cdot \sigma_{\gamma\gamma \to X} \cdot \frac{d\mathcal{L}^{TT}_{\gamma\gamma}}{dW_{\gamma\gamma}} \cdot dW_{\gamma\gamma} \tag{3.2}$$

Assuming that the interval, $\Delta W_{\gamma\gamma}$ we choose is such that the cross section is to first order constant over the whole interval, it can be expressed as

$$\sigma_{\gamma\gamma\to X}(W_{\gamma\gamma}) = \frac{N(W_{\gamma\gamma})}{\mathcal{L}_{int}\cdot\int_{\Delta W_{\gamma\gamma}}\mathcal{A}\cdot\frac{d\mathcal{L}^{TT}_{\gamma\gamma}}{dW_{\gamma\gamma}}dW_{\gamma\gamma}} \tag{3.3}$$

Therefore, if we evaluate the integral we can measure the cross section for the reaction $\gamma\gamma \to X$. The luminosity function $\mathcal{L}^{TT}_{\gamma\gamma}$ can be calculated analytically while the acceptance function $\mathcal{A}$ is unknown. The usual way to solve this integral is by Monte Carlo methods. For the analysis described in this thesis the Monte Carlo simulation is divided in four major steps. First, events simulating the reactions $\gamma\gamma \to 2\pi^+2\pi^-2\pi^0$, $\omega\omega$, $\omega\pi^+\pi^-\pi^0$, $\pi^+\pi^-\pi^0\pi^0$ were generated according to the exact QED expression presented in section 1.2 for collisions between transverse photons. The ω-meson decay was generated according to the matrix element for the decay of a vector meson to $\pi^+\pi^-\pi^0$. As a second step these events were passed through SIMARG (see section 2.14) and the full trigger simulation (see section 2.14.1). Then the events were reconstructed and had to satisfy the same selection criteria as the data. The events were generated assuming a constant cross-section of 1 nb leading to the sensitivity function $\mathcal{S}$ defined as :

$$\mathcal{S}(W_{\gamma\gamma}) = \mathcal{L}_{int}\cdot\int_{\Delta W_{\gamma\gamma}}\mathcal{A}\cdot\frac{d\mathcal{L}^{TT}_{\gamma\gamma}}{dW_{\gamma\gamma}}dW_{\gamma\gamma} \tag{3.4}$$

which represents the number of expected events in the $\Delta W_{\gamma\gamma}$ interval per nb. The cross section $\sigma(\gamma\gamma \to X)$ is then given by

$$\sigma_{\gamma\gamma\to X}(W_{\gamma\gamma}) = \frac{N(W_{\gamma\gamma})}{\mathcal{S}(W_{\gamma\gamma})}\ [nb] \tag{3.5}$$

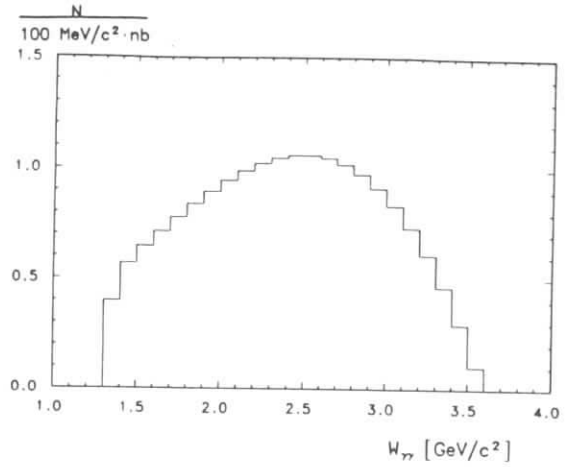

Figure 3.12: Sensitivity for $\gamma\gamma \to 2\pi^+2\pi^-2\pi^0$.

The sensitivity curves for the reactions $\gamma\gamma \to 2\pi^+2\pi^-2\pi^0$ and $\gamma\gamma \to \pi^+\pi^-\pi^0\pi^0$ are shown in figures 3.12 and 3.13 respectively. The sensitivities for the other channels studied in this thesis are shown in the relevant sections.

3.7 Topological Cross Sections

At the end we have to deal with 490 events of the type $\gamma\gamma \to 2\pi^+2\pi^-2\pi^0$ and 1178 events of the type $\pi^+\pi^-\pi^0\pi^0$. After the raw mass spectra (figures 3.5 and 3.8) are corrected for the estimated background, they are divided by the sensitivity for the corresponding reaction and hence the "topological" cross section for each reaction is obtained. The result is shown in figure 3.14 for the reaction $\gamma\gamma \to 2\pi^+2\pi^-2\pi^0$ and in figure 3.15 for the reaction $\gamma\gamma \to \pi^+\pi^-\pi^0\pi^0$. The term topological cross section means that the cross section is not corrected for any production of possible meson resonances that might be produced in an

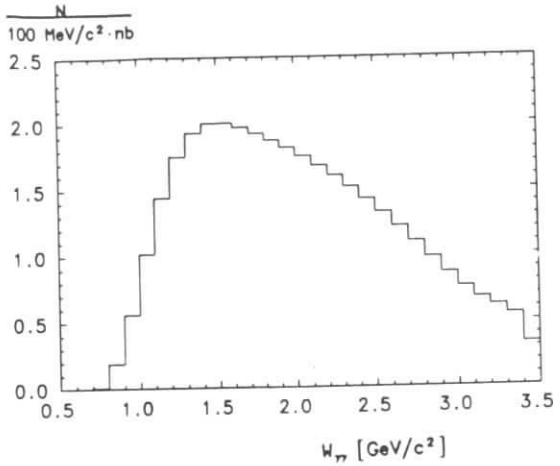

Figure 3.13: Sensitivity for $\gamma\gamma \to \pi^+\pi^-\pi^0\pi^0$.

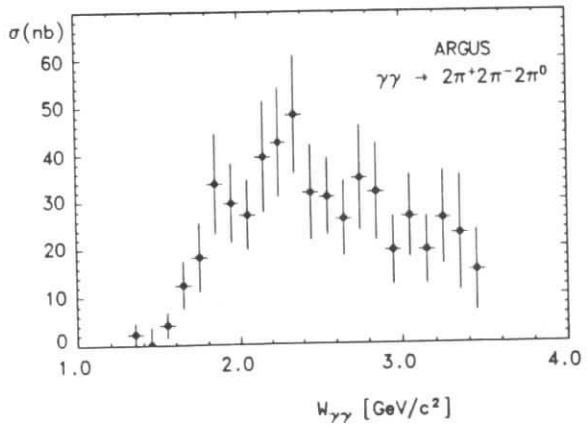

Figure 3.14: Topological cross section for $\gamma\gamma \to 2\pi^+2\pi^-2\pi^0$

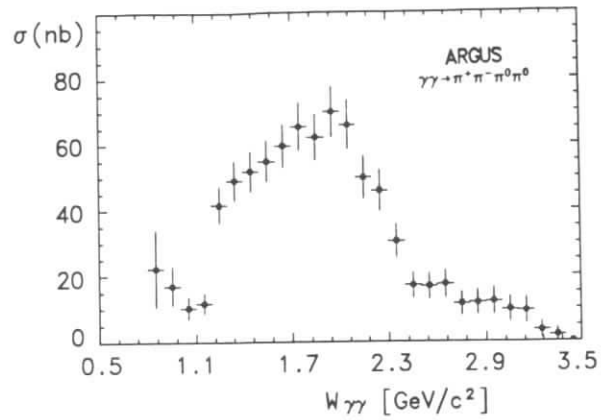

Figure 3.15: Topological cross section for $\gamma\gamma \to \pi^+\pi^-\pi^0\pi^0$

intermediate stage before we observe the final six (four) pions.

For the reaction $\gamma\gamma \to 2\pi^+2\pi^-2\pi^0$ the topological cross section starts at about 1.3 GeV/c^2 and rises smoothly to a maximum of ~45 nb at $W_{\gamma\gamma}$ ~2.4 GeV/c².

The topological cross section for the reaction $\gamma\gamma \to \pi^+\pi^-\pi^0\pi^0$ rises smoothly till about 70 nb at $W_{\gamma\gamma}$ ~2 GeV/c^2 and then drops rapidly for higher $W_{\gamma\gamma}$. For four pion masses less than 1 GeV/c^2 there is an enhancement, possibly due to the expected production of the $a_0(980)$ decaying into $a_0 \to \eta\pi^0$.

The systematic uncertainty for the topological cross sections is 13.5 %. This is found by adding in quadrature the following contributions. Acceptance calculation 11 % from uncertainties in the two photon generator and the full detector simulation, luminosity measurement 3 %, trigger simulation uncertainty 5 % and background estimation 5 %.

Chapter 4

Vector Meson Production

4.1 Introduction

In the following sections the observation of ω and ρ in the multipion subsystems for the two final states is described. The observation of correlated ω's in the $2\pi^+2\pi^-2\pi^0$ and ρ's in the $\pi^+\pi^-\pi^0\pi^0$ final states is also presented. The width of these meson resonances motivated the use of different analysis methods in order to extract the $\omega\omega$ and $\rho^+\rho^-$ contributions in the event samples. The ω-meson is narrow, allowing the recoil mass technique to be used for the $\omega\omega$ analysis, whereas for the $\rho^+\rho^-$, since ρ is very wide, the fractions of the different states that contribute to the measured $\pi^+\pi^-\pi^0\pi^0$ cross section were extracted by using a maximum likelihood method.

4.2 The $2\pi^+2\pi^-2\pi^0$ Final State

4.2.1 Mass Resolution

In order to study the production of ω-mesons we need to know the 3-pion mass resolution of the spectrometer. This was determined by studying the 3-pion

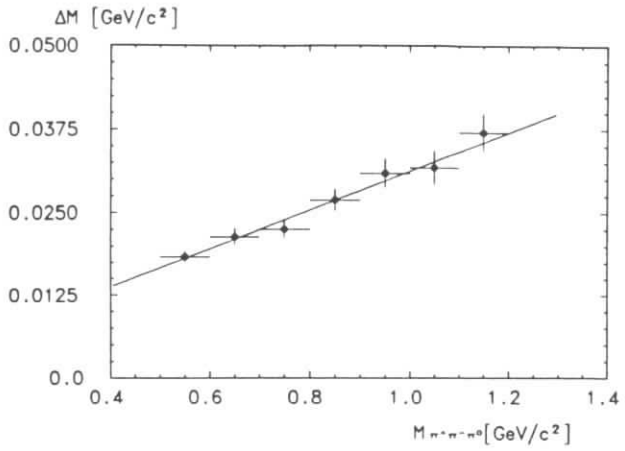

Figure 4.1: Mass resolution for three pions as a function of the invariant mass of the three pion system in $2\pi^+2\pi^-2\pi^0$ final state.

system with Monte Carlo generated events. The resulting mass resolution is shown in figure 4.1 as a function of the three pion mass. The resolution of the spectrometer for the ω-meson region is about 20 MeV/c^2.

4.2.2 ω-Meson Production

To investigate the ω-meson production in the $2\pi^+2\pi^-2\pi^0$ final state an additional constraint was applied to the events that survived the selection criteria presented in section 3.3. Since we have to deal with four photons in the final state, we can have up to three π^0-pair combinations. When the event had more than one π^0-pair candidate, the one that resulted in the lowest P_T^{tot} was chosen. This cut was motivated by the fact that the two photon events have low P_T^{tot}. Tests with Monte Carlo generated events showed that the efficiency of this cut

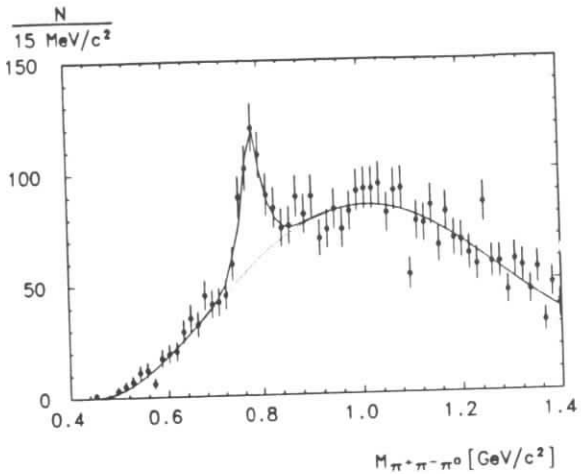

Figure 4.2: Invariant $\pi^+\pi^-\pi^0$ mass spectrum. The fit consists of a Breit-Wigner distribution with the parameters of the $\omega(783)$ meson, convoluted with a gaussian to describe the mass resolution of the detector, and a third order polynomial background (8 entries per event).

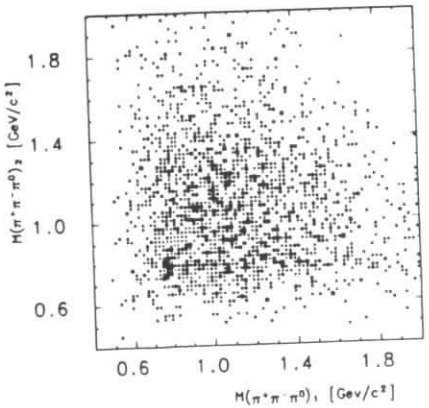

Figure 4.3: Scatter plot of the mass of one $\pi^+\pi^-\pi^0$ combination versus the mass of the remaining $\pi^+\pi^-\pi^0$ combination (4 entries per event).

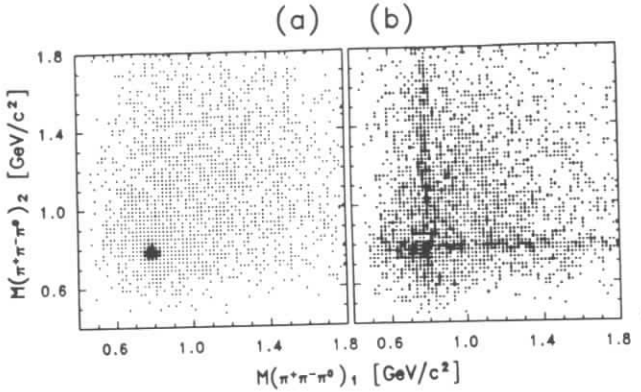

Figure 4.4: Scatter plot of the mass of one $\pi^+\pi^-\pi^0$ combination versus the mass of the remaining $\pi^+\pi^-\pi^0$ combination (4 entries per event) a) for $\omega\omega$ b) for $\omega\pi^+\pi^-\pi^0$ Monte Carlo generated events.

for assigning the correct photons to a π^0 is more than 95 %.

The invariant mass distribution of all $\pi^+\pi^-\pi^0$ combinations is shown in figure 4.2. A prominent peak at the position of the ω-meson can be seen. The mass distribution was fitted with a Breit-Wigner distribution with the $\omega(783)$ meson parameters [42] convoluted with a gaussian describing the mass resolution of the spectrometer, and a third order polynomial to describe the background.

The fit gives 263 ± 30 entries in the ω peak. The scatter plot of the invariant mass of only one $\pi^+\pi^-\pi^0$ combination versus the invariant mass of the other $\pi^+\pi^-\pi^0$ combination is shown in figure 4.3. Each event contributes four entries to this plot. A clear enhancement is seen in the $\omega\omega$ region. However, this enhancement can be due either to $\omega\omega$ production or to the overlap of two independent ω bands, as is demonstrated by Monte Carlo generated events in figure 4.4.

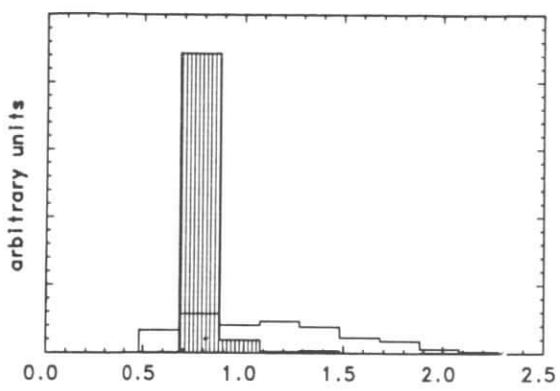

Figure 4.5: Invariant mass of the $\pi^+\pi^-\pi^0$ system recoiling against an ω meson for $\omega\omega$ (shaded histogram) and $\omega\pi^+\pi^-\pi^0$ (open histogram) Monte Carlo generated events.

To investigate whether this enhancement is due to a real $\omega\omega$ production, a recoil mass technique was used. In this technique one extracts the invariant mass of the three pions recoiling against an ω. For this purpose the number of ω-mesons was determined as a function of the invariant mass of the remaining $\pi^+\pi^-\pi^0$ combination. The $\omega\omega$ signal would manifest itself as an enhancement in the bin between 680 and 880 MeV/c^2 of the recoiling $\pi^+\pi^-\pi^0$ invariant mass. This is demonstrated with Monte Carlo generated events of the type $\gamma\gamma \to \omega\omega$ and $\gamma\gamma \to \omega\pi^+\pi^-\pi^0$ (figure 4.5), where the different features of the recoil mass of the two reactions can be seen.

The recoil $\pi^+\pi^-\pi^0$ invariant mass for the data is shown in figure 4.6. To estimate the expected distribution for events with only one ω, Monte Carlo generated $\gamma\gamma \to \omega\pi^+\pi^-\pi^0$ events were used with the total $W_{\gamma\gamma}$ distribution modified to agree with the observed $2\pi^+2\pi^-2\pi^0$ distribution. The resulting non-

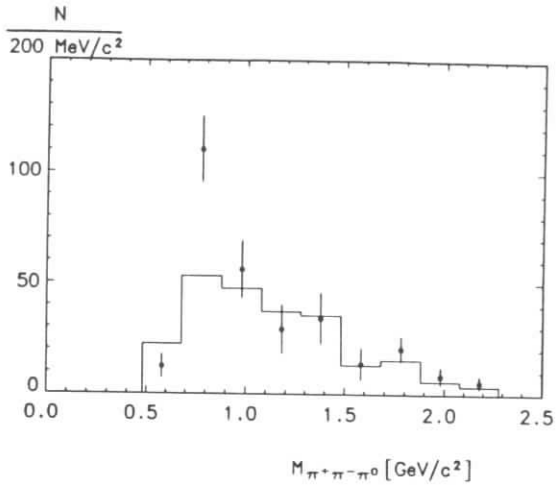

Figure 4.6: Invariant mass of the $\pi^+\pi^-\pi^0$ system recoiling against an ω meson. The data points are shown with error bars. The non-resonant three pion mass distribution, as expected from $\omega\pi^+\pi^-\pi^0$ Monte Carlo events, is shown as a histogram.

resonant $\pi^+\pi^-\pi^0$ mass from Monte Carlo is also shown in figure 4.6, normalized to the data at masses above 1.1 GeV/c^2. A clear excess of $\omega\omega$ events is seen in the data. Two other methods were used to determine the background from $\omega\pi^+\pi^-\pi^0$ in order to estimate the systematic uncertainty :

- Monte Carlo $\gamma\gamma \to 2\pi^+2\pi^-2\pi^0$ generated events
- wrong-sign combinations like $\pi^\pm\pi^\pm\pi^0$ in the data.

All three methods are in good agreement. The subtraction of the non-resonant background leaves in an excess of $(57 \pm 16 \pm 3)$ ω-mesons due to $\omega\omega$ events. The second error gives the systematic uncertainty. Thus, ($29 \pm 8 \pm 2$) $\gamma\gamma \to \omega\omega$ events are observed. This is the first evidence for $\omega\omega$ production in two-photon interactions.

4.2.3 Cross Section for $\gamma\gamma \to \omega\omega$

To derive the cross section for the reaction $\gamma\gamma \to \omega\omega$, events containing at least two different $\pi^+\pi^-\pi^0$ combinations with masses between 680 and 880 MeV/c^2 were selected. The shape of the background was estimated from wrong-sign combinations, requiring at least two $\pi^+\pi^-\pi^0$ mass combinations to be in the $\omega\omega$ region. This background was normalized so that 29 events remain after its subtraction from the data (figure 4.7). The sensitivity curve for $\gamma\gamma \to \omega\omega$ as derived from Monte Carlo simulation is shown in figure 4.8.

A possible background source would be real $\omega\omega$ events, where one photon was lost and an additional fake photon appears in the calorimeter. This was checked with Monte Carlo generated events of the type $\gamma\gamma \to \omega\omega$ using the noise simulation algorithm and was found to be negligible.

After correcting the 6 pion mass distribution of the 29 events for acceptance and BR($\omega \to \pi^+\pi^-\pi^0$), the cross section for $\gamma\gamma \to \omega\omega$ was derived and is shown in figure 4.9.

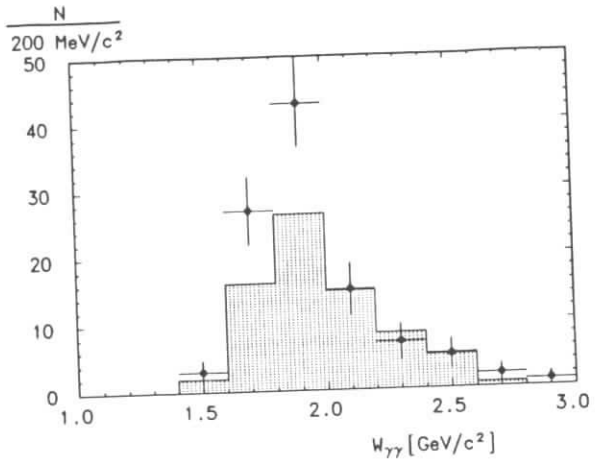

Figure 4.7: Mass distribution of the $2\pi^+2\pi^-2\pi^0$ for events with at least one candidate in the $\omega\omega$ region of the scatter plot of the figure 4.3 (open histogram). The hatched histogram shows the expected background from wrong sign combinations.

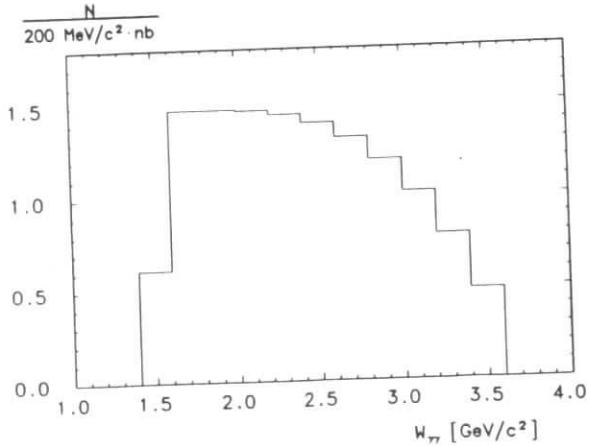

Figure 4.8: The sensitivity curve for $\gamma\gamma \to \omega\omega$

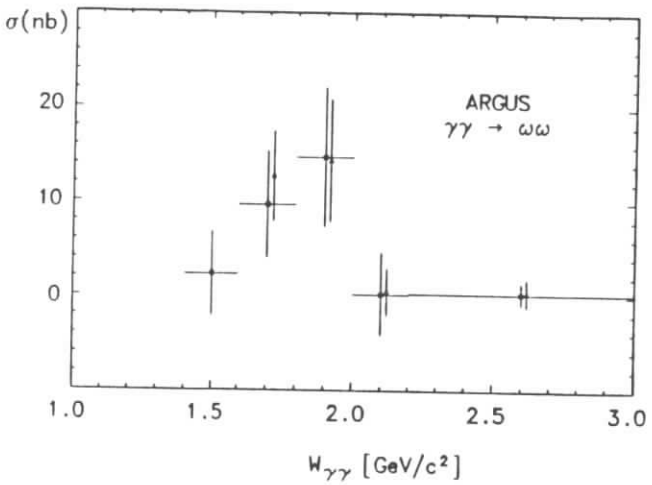

Figure 4.9: Cross section for the reaction $\gamma\gamma \to \omega\omega$ The cross section derived using background shape from wrong sign combinations is shown with dots and the one derived with the recoil mass technique in different $W_{\gamma\gamma}$ bins is shown with triangles.

A cross check for the derived cross section was made by applying the recoil mass technique in different $W_{\gamma\gamma}$ ranges. Again, after correcting for acceptance and BR($\omega \to \pi^+\pi^-\pi^0$) the cross section was derived and is shown in figure 4.9. The two results are in perfect agreement.

The $\omega\omega$ cross section shows an enhancement of about 12 nb $W_{\gamma\gamma}$ ~1.9 GeV/c^2, whereas for $W_{\gamma\gamma}$ greater than 2 GeV/c^2 the $\omega\omega$ production is suppressed.

The systematic uncertainty for the measured cross section of the reaction $\gamma\gamma \to \omega\omega$ is 25 %. The main contribution comes from the acceptance calculation which was done for isotropic $\omega\omega$ production. However, if the $\omega\omega$ final state is produced with a definite spin parity, it would result in a 17.5 % uncertainty in the acceptance calculation. From the different methods used for calculating the $\omega\omega$ cross section, the uncertainty is 15 %. In addition to that, there is a 4.5 % uncertainty resulting from the $\pi^+\pi^-\pi^0$ invariant mass fits, 5 % from the estimation of the total number of $\omega\omega$ events, 5 % from the trigger simulation and 3 % from luminosity measurement.

4.2.4 The Reaction $\gamma\gamma \to \omega\pi^+\pi^-\pi^0$

In the previous section we found that 57 out of 263 ω's are from the reaction $\gamma\gamma \to \omega\omega$. The rest come from any other channel that would have a final state of the type $\omega\pi^+\pi^-\pi^0$. In order to find the cross section of this final state, the distribution of the number of ω mesons is plotted as a function of the total $2\pi^+2\pi^-2\pi^0$ invariant mass (figure 4.10). This distribution was derived by fitting the corresponding $\pi^+\pi^-\pi^0$ mass spectra and determining the number of ω mesons in different 6 pion mass bins. With this procedure a total of 249 $\pm$ 33 ω mesons were found, which is in good agreement with the total number of the 263 $\pm$ 30 ω's found by fitting the $\pi^+\pi^-\pi^0$ invariant mass spectrum for the

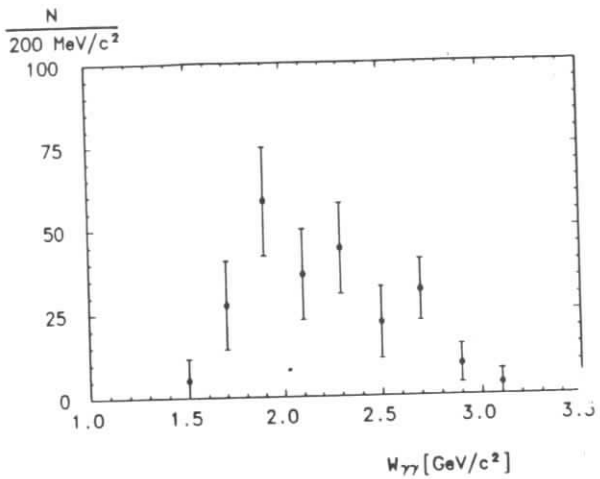

Figure 4.10: Number of ω-mesons as a function of the $2\pi^+2\pi^-2\pi^0$ invariant mass.

whole $W_{\gamma\gamma}$ range. After subtracting the $\omega\omega$ events, which contribute to this plot with two entries per event, the distribution of number of ω mesons as a function of $W_{\gamma\gamma}$ for events with only one ω meson in the final state remains.

The only significant background process to the reaction $\gamma\gamma \to \omega\pi^+\pi^-\pi^0$ is when one photon escapes detection at the same time as noise in the calorimeter fakes a photon. Monte Carlo studies show that the expected background of this type amounts to 11.5 events.

The sensitivity for the reaction $\gamma\gamma \to \omega\pi^+\pi^-\pi^0$ is shown in figure 4.11.

Finally, to derive the cross section the distribution of the number of ω mesons is divided by the sensitivity and corrected for the 11.5 background events as well as for the BR($\omega \to \pi^+\pi^-\pi^0$). The resulting cross section is shown in figure 4.12. The cross section for the reaction $\gamma\gamma \to \omega\pi^+\pi^-\pi^0$ does not show any structure within the present statistics. It is a smooth distribution that reaches a maximum of about 20 nb at $W_{\gamma\gamma} \sim 2.3GeV/c^2$.

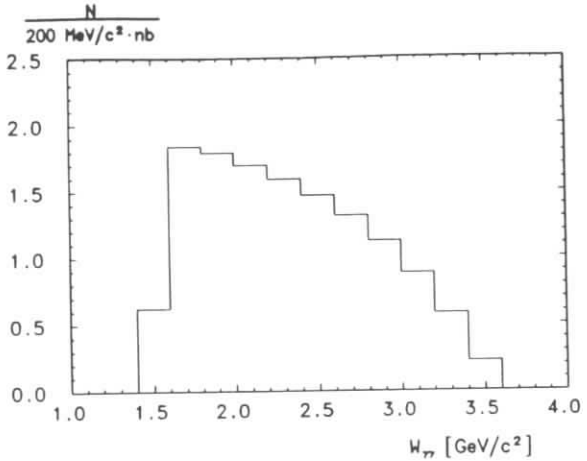

Figure 4.11: The sensitivity curve for $\gamma\gamma \to \omega\pi^+\pi^-\pi^0$

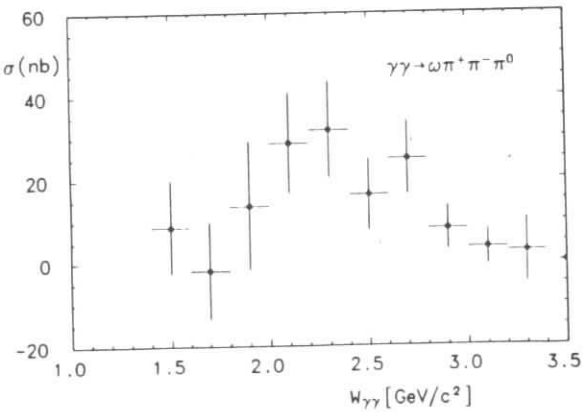

Figure 4.12: Cross section for $\gamma\gamma \to \omega\pi^+\pi^-\pi^0$ as a function of $W_{\gamma\gamma}$.

The systematic uncertainty on the measured cross section for the reaction $\gamma\gamma \to \omega\pi^+\pi^-\pi^0$ is 14 %. The acceptance calculation contributes 11 %, the luminosity measurement 3 %, the estimation of the number of ω-mesons from the $\pi^+\pi^-\pi^0$ invariant mass fits 4.5 % and the background estimation 5 %.

4.3 The $\gamma\gamma \to \pi^+\pi^-\pi^0\pi^0$ Final State

4.3.1 ρ-meson Production

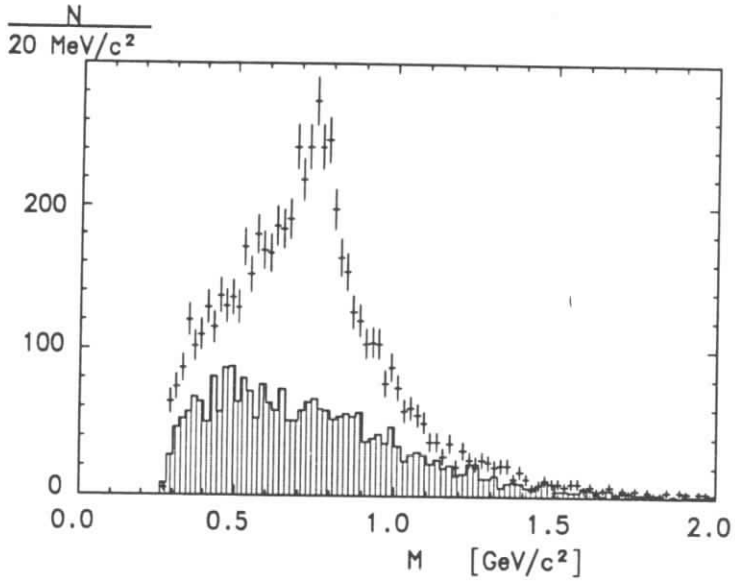

Figure 4.13: The invariant mass of $\pi^\pm\pi^0$ combinations is shown as crosses (4 entries per event). A clear enhancement can be seen in the ρ-meson region whereas in the invariant mass of the "wrong" sign combinations ($\pi^{+(0)}\pi^{-(0)}$, shaded histogram, 2 entries per event) no signal is observed.

The production of charged ρ-mesons is demonstrated in figure 4.13 where the invariant mass of the two pion combinations is shown. The evidence for events with two correlated ρ-mesons is demonstrated in the scatter plots of figure 4.14 where the invariant mass of the $\pi^+\pi^0$ and of the $\pi^-\pi^0$ combinations is plotted on two axes respectively, in different $W_{\gamma\gamma}$ ranges. The "wrong" sign combinations ($m_{\pi^+\pi^-}$ and $m_{\pi^0\pi^0}$) are also presented in figure 4.14 for the same $W_{\gamma\gamma}$ regions. The clear enhancement in the $\rho^+\rho^-$ region indicates the presence of $\gamma\gamma \to \rho^+\rho^-$ in the data.

4.3.2 The 3-parameter Fit

For the $\rho^+\rho^-$ analysis, as in the case of the $\omega\omega$ analysis, the two π^0's resulting the smallest P_T^{tot} of the event were chosen. In order to determine quantitatively the $\rho^+\rho^-$ contribution, some assumptions had to be made. As a first step (referred to as the 3-parameter fit) the following two assumptions were made :

1. The observed final state $\pi^+\pi^-\pi^0\pi^0$ is an *incoherent* sum of the three final states $\rho^+\rho^-$, $\rho^\pm\pi^\mp\pi^0$, and the non-resonant $\pi^+\pi^-\pi^0\pi^0$.

2. Each final state is produced with *isotropically* distributed (decay) particles.

The first point (1) means that no interference effects between the three final states are considered. As for the second point (2), $\rho^+\rho^-$ and $\rho^\pm\pi^\mp\pi^0$ are the simplest possible states with a ρ-meson. Other states, for example, $a_2^\pm\pi^\mp$ and $a_1^\pm\pi^\mp$, are also conceivable. An attempt was made to include events of these two final states in the fitting procedure. This influenced only the $\rho\pi\pi$ fractions while the $\rho^+\rho^-$ and the non-resonant $\pi^+\pi^-\pi^0\pi^0$ contributions remained unchanged. No significant signals of either a_2 or a_1 are however observed in the data, so they were not included in the final analysis.

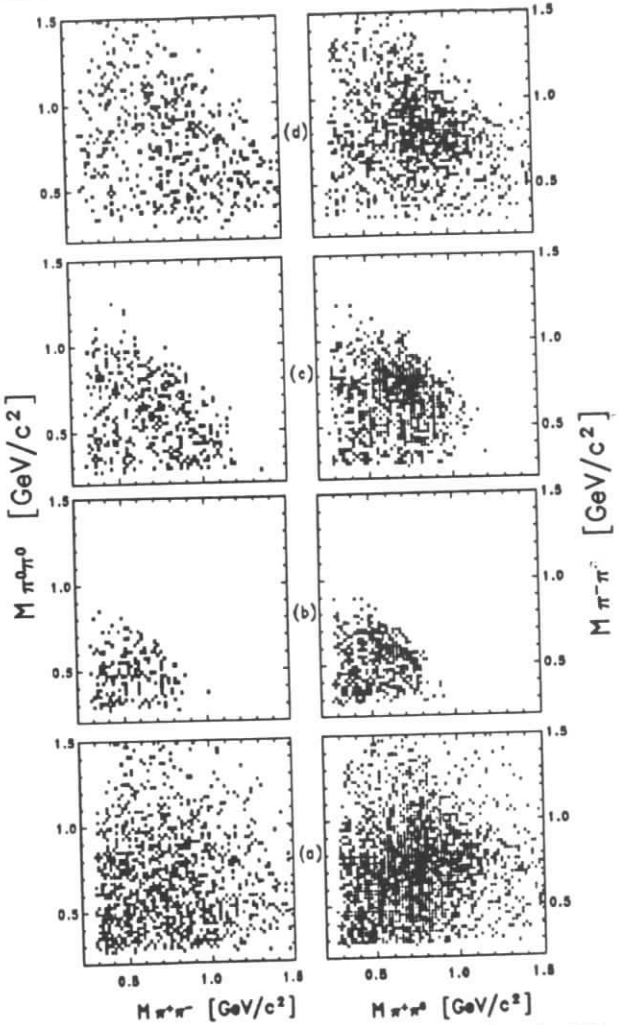

Figure 4.14: Scatter plots of two-pion mass distributions in different $W_{\gamma\gamma}$ regions. The first column corresponds "wrong" sign combinations ($m_{\pi^+\pi^-}$ vs. $m_{\pi^0\pi^0}$) and the second column to the to the "right" sign combinations ($m_{\pi^+\pi^0}$ vs. $m_{\pi^-\pi^0}$). a) all $W_{\gamma\gamma}$ b) $W_{\gamma\gamma} < 1.4\ GeV/c^2$, c) $1.4 < W_{\gamma\gamma} < 1.8\ GeV/c^2$ and d) $1.8\ GeV/c^2 < W_{\gamma\gamma}$.

It should be noted that the isotropic $\rho^0\pi^0\pi^0$ production via two photon interactions is forbidden due to the following arguments. Since we deal with two photon interactions the C-parity is +1. The existence of four pions in the final state requires G-parity +1. The C and the G parity of the final state can be written as

$$C = (-1)^{l+s}$$

$$G = (-1)^{l+s+I}$$

From this, one can conclude that the isospin I of the final state is even. The presence of ρ^0 with I=1 requires that the $\pi^0\pi^0$ system has also I=1, which is impossible.

One argument holds, however, for retaining $\rho^\pm\pi^\mp\pi^0$: Conservation of C-parity requires that the $\rho^\pm\pi^\mp\pi^0$ system has a component with odd orbital angular momentum, which is not fulfilled for isotropic production and decay. But if the detector acceptance for the correct spin-parity assignment(s) of any system is not much different from that for the isotropic case, then ignoring angular dependence should make no difference. If not, the resulting cross-sections might in reality be quite different. In the case of the $\rho^+\rho^-$ system, the detector acceptance for the isotropic case represents a mean of the acceptances for the six different J^P cases considered (section 4.4). Therefore, this is likely to be valid for the $\rho^\pm\pi^\mp\pi^0$ system as well. Hence, as a first approximation, an isotropic state is the most reasonable choice. With these two assumptions, a maximum likelihood procedure was used to derive the three contributions.

The procedure, as well as the formalism, is similar to the one used in the TASSO analysis of the $\rho^0\rho^0$ channel [8, (1982)].

The differential cross section for the reaction $\gamma\gamma \to \pi^+\pi^-\pi^0\pi^0$ for fixed $W_{\gamma\gamma}$, was parametrized by

$$\frac{d\sigma}{d\xi} = C \cdot W_4(W_{\gamma\gamma}) \cdot \mid g_i(\xi) \mid^2 \qquad (i = \rho\rho, \rho 2\pi, 4\pi) \tag{4.1}$$

where C is a constant, W_4 the $\pi^+\pi^-\pi^0\pi^0$ phase space, and g_i the matrix element for the final states i. The symbol ξ represents the set of seven variables needed to describe the cross section

$$\xi = (m_{12}^2, m_{34}^2, \vec{\zeta}) = (m_{12}^2, m_{34}^2, \theta_\rho^{12}, \theta_\pi^{12}, \phi_\pi^{12}, \theta_\pi^{34}, \phi_\pi^{34}) \tag{4.2}$$

where the numbers 1,...,4 refer to the four pions using the convention: $\pi_1^+\pi_2^0\pi_3^-\pi_4^0$. The variable m_{ij} denotes the invariant mass of two pions i and j; θ_ρ^{ij} the production angle of the system ij in the $\gamma\gamma$ center-of-mass system; and θ_π^{ij} and ϕ_π^{ij} the polar and azimuthal angles of the pions in the ij center-of-mass system.

In the first step, the three parameter fit, the $\rho^+\rho^-$ system was assumed to be produced isotropically so the angular dependence of ξ is removed and the symmetrized matrix element $g_{\rho\rho}$ is

$$g_{\rho\rho} = \frac{1}{\sqrt{2}}(BW(m_{12})BW(m_{34}) + BW(m_{14})BW(m_{23})) \tag{4.3}$$

where BW denotes the Breit-Wigner amplitude [47]

$$BW(m) = \frac{\sqrt{\frac{m_\rho \Gamma_\rho m}{p^*}}}{\pi(m_\rho^2 - m^2 - im_\rho\Gamma_\rho)} \tag{4.4}$$

$$\Gamma_\rho = \Gamma_0 \left(\frac{p^*}{p_0^*}\right)^3 \frac{2p_0^{*2}}{p_0^{*2} + p^{*2}} \tag{4.5}$$

$$p^* = \frac{1}{2}\sqrt{m^2 - 4m_\pi^2} \quad , \quad p_0^* = \frac{1}{2}\sqrt{m_\rho^2 - 4m_\pi^2} \tag{4.6}$$

$$m_\rho = 770 \text{ MeV} \quad , \Gamma_0 = 150 \text{ MeV}.$$

The $\rho^\pm\pi^\mp\pi^0$ matrix element is

$$g_{\rho 2\pi} = \frac{1}{2}(BW(m_{12}) + BW(m_{34}) + BW(m_{14}) + BW(m_{23})) \tag{4.7}$$

and for the phase space

$$g_{4\pi} = 1. \tag{4.8}$$

In order to extract the fractions λ_i, of the different contributions in the data, each event was assigned a probability P_i to result from process i . Then the probability for the whole data sample was maximized by varying the three parameters λ_i, using the maximum likelihood function

$$\Lambda = \prod_n \sum_i \lambda_i P_i(\xi_n) \tag{4.9}$$

with the constraint that

$$\sum \lambda_i = 1 \tag{4.10}$$

The product runs over all the events n, and the quantity $P_i(\xi)$ is the normalized probability of the accepted event n with measured variables ξ.

Finally the fit maximizes the quantity

$$\sum_n \left[ln \left(\sum_i \lambda_i \frac{\mid g_i(\xi) \mid^2}{\int A(\xi) d\sigma(\xi)} \right) - \sum_i \lambda_i \right] \tag{4.11}$$

where $A(\xi)$ is the detector acceptance. The sensitivity for each of the three hypotheses is shown in figure 4.15.

The cross sections derived from the 3-parameter fit are shown in figure 4.16 and are also listed in Table 4.1.

The cross section for the reaction $\gamma\gamma \to \rho^+\rho^-$ is about a factor 4 smaller than the $\rho^0\rho^0$ cross section in the range 1.2 to 2.0 GeV/c^2. The cross sections for the reactions $\gamma\gamma \to \rho\pi\pi$ and $\gamma\gamma \to$ non resonant $\pi^+\pi^-\pi^0\pi^0$ do not show any structure and they have a mean value of about 20 nb each.

In figure 4.17 the $\pi^\pm\pi^0$ invariant mass distributions for the data (crosses) are compared with the Monte Carlo expectations (histogram) using the fractions derived from the fit. The agreement between the two is excellent.

If the contribution of the $\rho\pi\pi$ is neglected in the fitting procedure then its contribution divides equally into the $\rho^+\rho^-$ and the non-resonant $\pi^+\pi^-\pi^0\pi^0$ fractions.

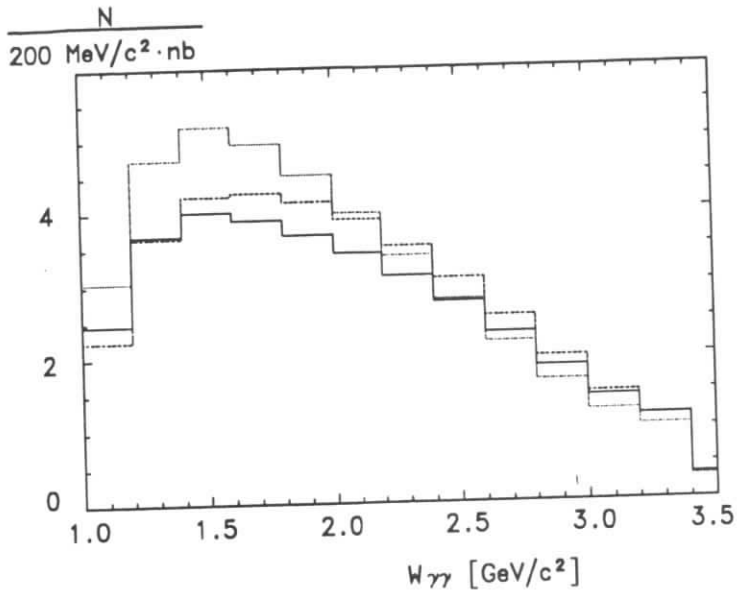

Figure 4.15: Sensitivity curves for the final states a)$\rho^+\rho^-$ (dotte : histogram), b)$\rho^\pm\pi^\mp\pi^0$ (dashed histogram) and c) non-resonant $\pi^+\pi^-\pi^0\pi^0$(f· ll histogram).

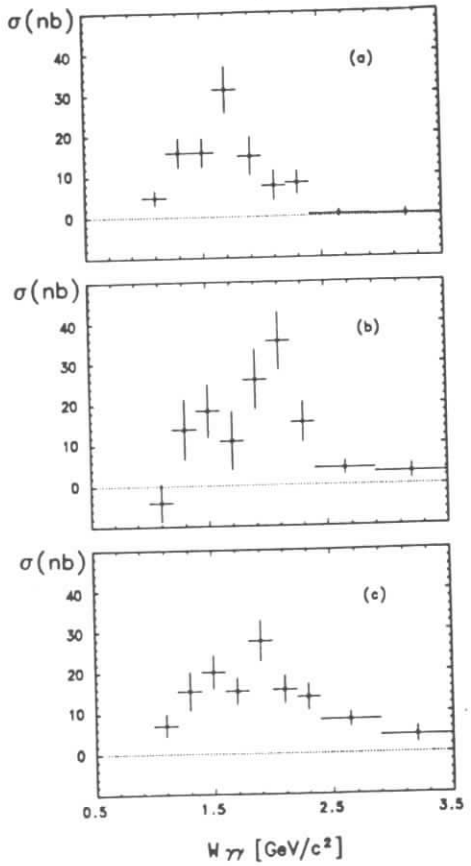

Figure 4.16: Cross sections resulted from the 3-parameter fit. a) $\gamma\gamma \to \rho^+\rho^-$, b) $\gamma\gamma \to \rho^\pm\pi^\mp\pi^0$ and c) $\gamma\gamma \to \pi^+\pi^-\pi^0\pi^0$ (non-resonant).

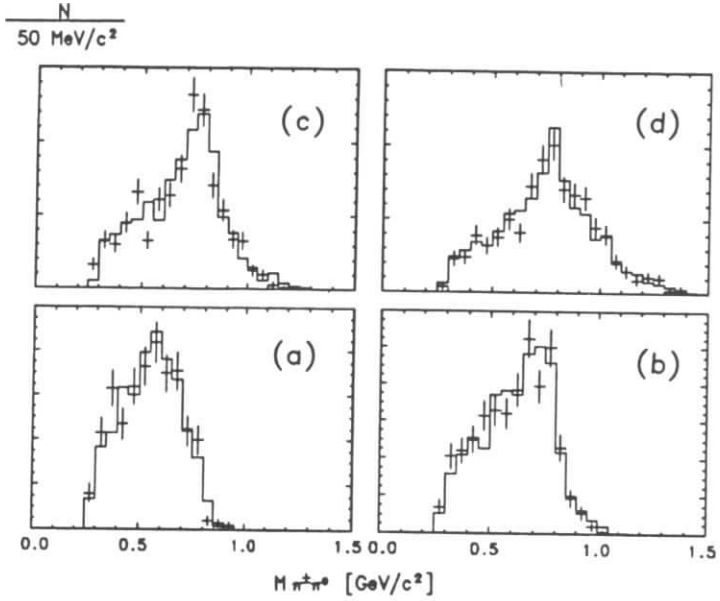

Figure 4.17: Comparison of the $\pi^{\pm}\pi^0$ invariant mass distributions in the data (crosses) with the Monte Carlo expectations (histogram) using the fractions derived from the the 3-parameter fit. The comparison is made in four $W_{\gamma\gamma}$ bins. a) $1.2 \leq W_{\gamma\gamma} \leq 1.4$ GeV/c², b) $1.4 \leq W_{\gamma\gamma} \leq 1.6$ GeV/c², c) $1.6 \leq W_{\gamma\gamma} \leq 1.8$ GeV/c², d) $1.8 \leq W_{\gamma\gamma} \leq 2.0$ GeV/c².

cross section for different states (nb)			
$W_{\gamma\gamma}$ (GeV/c^2)	$\rho^+\rho^-$	$\rho^{\pm}\pi^{\mp}\pi^0$	non res. 4π
1.0 – 1.2	4.78 ± 1.77	-4.14 ± 4.59	7.03 ± 2.66
1.2 – 1.4	15.80 ± 3.45	13.88 ± 7.31	15.50 ± 4.58
1.4 – 1.6	15.82 ± 3.46	18.43 ± 6.48	20.14 ± 4.06
1.6 – 1.8	31.26 ± 5.65	14.88 ± 4.59	26.10 ± 7.27
1.8 – 2.0	14.88 ± 4.59	26.10 ± 7.27	27.68 ± 4.94
2.0 – 2.2	7.59 ± 3.60	35.50 ± 7.06	15.65 ± 3.30
2.2 – 2.4	8.22 ± 2.71	15.41 ± 4.85	13.85 ± 3.07
2.4 – 2.9	0.53 ± 0.87	4.06 ± 1.57	8.25 ± 1.74
2.9 – 3.5	0.38 ± 1.10	3.08 ± 1.81	4.30 ± 1.90

Table 4.1: Cross section in nb for $\rho^+\rho^-$ (different J^P states), $\rho\pi\pi$ and non resonant $\pi^+\pi^-\pi^0\pi^0$.

4.4 Angular Correlations

By studying angular correlations of the production and decay of a final state one obtains information about its spin parity. The spin parity analysis of the $\rho^+\rho^-$ system will shed more light on the different theoretical approaches to vector meson pair production in two photon interactions.

In order to study the angular correlations in the reaction $\gamma\gamma \to \rho^+\rho^-$ only states with spin J=0 and J=2 were considered. Spin-1 states are excluded by the Landau-Yang's theorem (Appendix A) since we deal with untagged events. The analysis is also restricted to the lowest angular momenta L between the two ρ's that are allowed by parity conservation, L=0 and L=1. This seems justified since the $\rho^+\rho^-$ production is observed reasonably close to the threshold. The parity of the state is given by $P = (-1)^L$. The matrix element for the ρ decay is derived in Appendix B.

The fact that the initial state consists of two photons gives two additional constraints

- spin-2 states with helicity $J_z = \pm 1$ are not allowed due to helicity conservation.

- The state $J^P = 2^-$ can only be produced with helicity $J_z = 0$ because :

  the state $\left(J^P, J_z\right) = (2^-, \pm 2)$ requires L=1, S=1 and S_z=1.
  However, S=1, S_z=1 require that at least one of the two photons has helicity 0. This is unphysical for real photons.

For $J^P = 2^+$ both J_z=0 and 2 contribute with, in principle, arbitrary relative strength. Assuming, however, that in the initial $\gamma\gamma$ state the lowest multipole dominates and that the matrix elements do not depend on the $\gamma\gamma$ helicity, J_z=2 and J_z=0 will be produced in the ratio 6:1. This can be easily seen in the Clebsh-Gordan coefficients for the decomposition

$$|\,2, \pm 2\,> \;=\; |\,1,\,1\,>|\,1,\,1\,> \;+\; |\,1,\,-1\,>|\,1,\,-1\,>$$

$$|\,2,\,0\,> \;=\; \sqrt{1/6}\,|\,1,\,-1\,>|\,1,\,1\,> \;+\; \sqrt{1/6}\,|\,1,\,1\,>|\,1,\,-1\,>$$

The dominance of helicity 2 is expected from other theoretical arguments and is seen in the data on the photon production of tensor mesons. See for example [3].

The decay of a state with spin-parity J^P into two vector mesons is in general determined by different amplitudes depending on the spin component J_z of the initial state, the orbital angular momentum L and the total spin S of the final state. The spatial properties of each amplitude can be represented by a sum of products of spherical harmonics, one for the $\rho^+\rho^-$ orbital angular momentum and one for each of the ρ decays.

$$\Psi^{J^P,J_z,L,S}(\vec{\zeta}) \propto \sum_{L_z,s_{\rho^+},s_{\rho^-}} \alpha^{J^P,J_z}_{L,L_z,S_{12},S_{34}} \left[Y_L^{L_z}(\theta_\rho^{12},\phi_\rho^{12}) Y_1^{S_{12}}(\theta_\pi^{12},\phi_\pi^{12}) \times Y_1^{S_{34}}(\theta_\pi^{34},\phi_\pi^{34})\right] \qquad (4.12)$$

where the numbering of the pions is the same as in section 4.3. The coefficients $\alpha^{J^P,J_z}_{L,L_z,S_{12},S_{34}}$ are defined as

$$\alpha^{J^P,J_z}_{L,L_z,S_{12},S_{34}} = \,< S_{12}, S_{12z}\; S_{34}, S_{34z} \mid S, S_z >< S, S_z\; L, L_z \mid J, J_z > \qquad (4.13)$$

L	L_z	S_{12}	S_{34}	J^P, J_z, S					
				$0^+,0,0$	$0^-,0,1$	$2^+,0,2$	$2^+,2,2$	$2^-,0,1$	$2^-,0,2$
0	0	1	-1	1		1			
0	0	0	0	-1		2			
0	0	-1	1	1		1			
0	0	1	1				1		
1	1	0	-1		1			1	-1
1	1	-1	0		-1			-1	-1
1	0	1	-1		-1			2	
1	0	-1	1		1			-2	
1	-1	0	1		-1			-1	1
1	-1	1	0		1			1	1

Table 4.2: The coefficients $\alpha^{J^P,J_z}_{L,L_z,S_{12},S_{34}}$ entering the angular distributions of the different spin-parity (J^P, J_z, S) states of the $\rho^+\rho^-$ system (not normalized).

The coefficients $\alpha^{J^P,J_z}_{L,L_z,S_{12},S_{34}}$ are shown in Table 4.2. L, L_z are the quantum numbers of the $\rho^+\rho^-$ angular momentum; the corresponding spherical harmonics depend on the ρ^{12} production angles $\theta_\rho^{12}, \phi_\rho^{12}$ defined in the $\gamma\gamma$ center-of-mass system. Since we deal with no tag events the angle ϕ_ρ^{12} is integrated out. It is convenient to define the angular distribution in the so called "$\gamma\gamma$ *helicity*" system. This is the $\gamma\gamma$ center of mass system with the z axis pointing along the $\gamma\gamma$ direction and the x axis in the production plane of ρ^{12}; in this system ϕ_ρ^{12}=0. S is the total spin of the $\rho^+\rho^-$ system. The decay angles θ_π^{ij} and ϕ_π^{ij} are the polar and azimuthal angles of the charged pion in the ij center-of-mass system.

The amplitudes $\Psi(\mathbf{J^P}, \mathbf{J_z}, \mathbf{L}, \mathbf{S})$ for the different J^P states are expressed as:

$$\Psi(0^+,0,0,0) \propto\; Y_0^0(\zeta_1)\left(Y_1^1(\zeta_2)Y_1^{-1}(\zeta_3) - Y_1^0(\zeta_2)Y_1^0(\zeta_3) + Y_1^{-1}(\zeta_2)Y_1^1(\zeta_3)\right) \qquad (4.14)$$

$$\begin{aligned}\Psi(0^-,0,1,0) \propto\ & Y_1^1(\zeta_1)\left(Y_1^0(\zeta_2)Y_1^{-1}(\zeta_3) - Y_1^{-1}(\zeta_2)Y_1^0(\zeta_3)\right) \\ & -Y_1^0(\zeta_1)\left(Y_1^1(\zeta_2)Y_1^{-1}(\zeta_3) - Y_1^{-1}(\zeta_2)Y_1^1(\zeta_3)\right) \\ & +Y_1^{-1}(\zeta_1)\left(Y_1^1(\zeta_2)Y_1^0(\zeta_3) - Y_1^0(\zeta_2)Y_1^1(\zeta_3)\right)\end{aligned} \tag{4.15}$$

$$\Psi(2^+,2,0,2) \propto\ Y_0^0(\zeta_1)Y_1^1(\zeta_2)Y_1^1(\zeta_3) \tag{4.16}$$

$$\begin{aligned}\Psi(2^+,0,0,2) \propto\ & Y_0^0(\zeta_1)\left(Y_1^1(\zeta_2)Y_1^{-1}(\zeta_3) + Y_1^{-1}(\zeta_2)Y_1^1(\zeta_3)\right. \\ & \left. + 2Y_1^0(\zeta_2)Y_1^0(\zeta_3)\right)\end{aligned} \tag{4.17}$$

$$\begin{aligned}\Psi(2^-,0,1,1) \propto\ & Y_1^1(\zeta_1)\left(Y_1^0(\zeta_2)Y_1^{-1}(\zeta_3) - Y_1^{-1}(\zeta_2)Y_1^0(\zeta_3)\right) \\ & +2Y_1^0(\zeta_1)\left(Y_1^1(\zeta_2)Y_1^{-1}(\zeta_3) - Y_1^{-1}(\zeta_2)Y_1^1(\zeta_3)\right) \\ & +Y_1^{-1}(\zeta_1)\left(Y_1^1(\zeta_2)Y_1^0(\zeta_3) - Y_1^0(\zeta_2)Y_1^1(\zeta_3)\right)\end{aligned} \tag{4.18}$$

$$\begin{aligned}\Psi(2^-,0,1,2) \propto\ & Y_1^1(\zeta_1)\left(-Y_1^0(\zeta_2)Y_1^{-1}(\zeta_3) - Y_1^{-1}(\zeta_2)Y_1^0(\zeta_3)\right) \\ & +Y_1^{-1}(\zeta_1)\left(Y_1^1(\zeta_2)Y_1^0(\zeta_3) + Y_1^0(\zeta_2)Y_1^1(\zeta_3)\right)\end{aligned} \tag{4.19}$$

The $\rho^+\rho^-$ matrix element introduced in equation (4.3) is extended by including the angular part Ψ and becomes:

$$\begin{aligned}g_{\rho\rho}^{J^P,J_z} = \ & \frac{1}{\sqrt{2}}\left(BW(m_{12})BW(m_{34})\Psi^{J^P,J_z}(\vec{\zeta}_{1234})\right. \\ & \left. + BW(m_{14})BW(m_{23})\Psi^{J^P,J_z}(\vec{\zeta}_{1432})\right)\end{aligned} \tag{4.20}$$

where BW denotes the Breit-Wigner amplitude for the ρ (section 4.4). The six J^P amplitudes were assumed to be produced *incoherently*. Note that a total of 8 final states is taken into account, the six J^P amplitudes of the $\rho^+\rho^-$ system together with the isotropic $\rho\pi\pi$ and non-resonant $\pi^+\pi^-\pi^0\pi^0$ final states.

The fitting procedure is basically the same as the one described in section 4.3 for the three parameter fit the only difference being that now we have to deal with eight parameters λ_i.

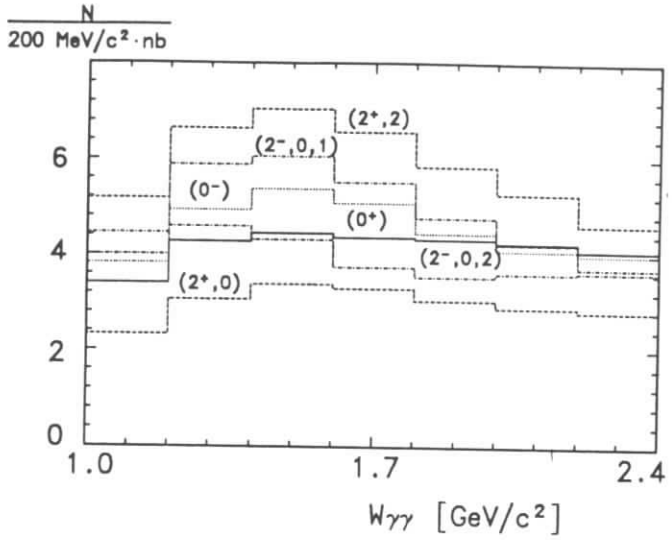

Figure 4.18: Sensitivities for differents J^P assignments for the reaction $\gamma\gamma \to \rho^+\rho^-$.

The sensitivity curves for each of the J^P states are shown in figure 4.18.

The cross sections resulting from the 8-parameter fit are shown in figure 4.19 and are summarized in Table 4.3.

cross section for different states (nb)				
$W_{\gamma\gamma}$ (GeV/c^2)	$0^+,0$	$0^-,0$	$2^+,2$	$2^+,0$
1.2 – 1.4	3.01 ± 3.27	2.71 ± 1.39	11.88 ± 3.59	-3.49 ± 2.22
1.4 – 1.6	13.80 ± 3.70	1.52 ± 1.47	2.59 ± 3.01	-0.32 ± 2.64
1.6 – 1.8	9.40 ± 3.75	3.56 ± 1.53	10.17 ± 3.57	1.71 ± 2.52
1.8 – 2.0	6.43 ± 3.65	0.27 ± 1.48	11.51 ± 3.61	-2.57 ± 2.99
2.0 – 2.2	3.05 ± 2.97	-1.86 ± 1.77	9.01 ± 2.32	-2.77 ± 4.88

$W_{\gamma\gamma}$ (GeV/c^2)	$2^-,0$ $S=1$	$2^-,0$ $S=2$	$\rho^\pm\pi^\mp\pi^0$	non res. 4π
1.2 – 1.4	-1.02 ± 1.55	-2.74 ± 1.89	10.86 ± 7.16	15.96 ± 4.79
1.4 – 1.6	-1.30 ± 1.49	-2.78 ± 1.99	22.85 ± 6.35	17.72 ± 3.67
1.6 – 1.8	-0.88 ± 1.73	5.81 ± 2.04	11.38 ± 5.77	14.25 ± 2.99
1.8 – 2.0	-2.25 ± 2.08	1.58 ± 1.94	16.61 ± 7.52	28.13 ± 4.37
2.0 – 2.2	-1.47 ± 2.12	-1.65 ± 2.43	35.31 ± 7.44	15.09 ± 3.22

Table 4.3: Cross section in nb for $\rho^+\rho^-$ (different J^P states), $\rho\pi\pi$ and non resonant $\pi^+\pi^-\pi^0\pi^0$ from **the 8 parameter fit**.

cross section for different states (nb)				
$W_{\gamma\gamma}$ (GeV/c^2)	$0^+,0$	$2^+,2$	$\rho^\pm\pi^\mp\pi^0$	non res. 4π
1.2 – 1.4	-1.54 ± 2.91	13.09 ± 2.93	9.81 ± 6.21	15.74 ± 4.57
1.4 – 1.6	12.40 ± 3.19	1.42 ± 2.24	23.76 ± 6.05	17.13 ± 3.82
1.6 – 1.8	12.34 ± 3.51	9.44 ± 2.91	20.28 ± 6.10	14.82 ± 2.99
1.8 – 2.0	7.87 ± 3.05	8.73 ± 2.67	15.97 ± 6.57	28.29 ± 4.48
2.0 – 2.2	0.71 ± 2.34	6.57 ± 2.81	25.70 ± 6.79	15.82 ± 3.35

Table 4.4: Cross section in nb for $\rho^+\rho^-$ (different J^P states), $\rho\pi\pi$ and non resonant $\pi^+\pi^-\pi^0\pi^0$ from **4-parameter fit**.

The $\gamma\gamma \to \rho^+\rho^-$ cross section is dominated by two amplitudes, $J^P = 0^+$ and $J^P = 2^+$ helicity 2. The $J^P = 0^+$ contribution reaches a maximum of about

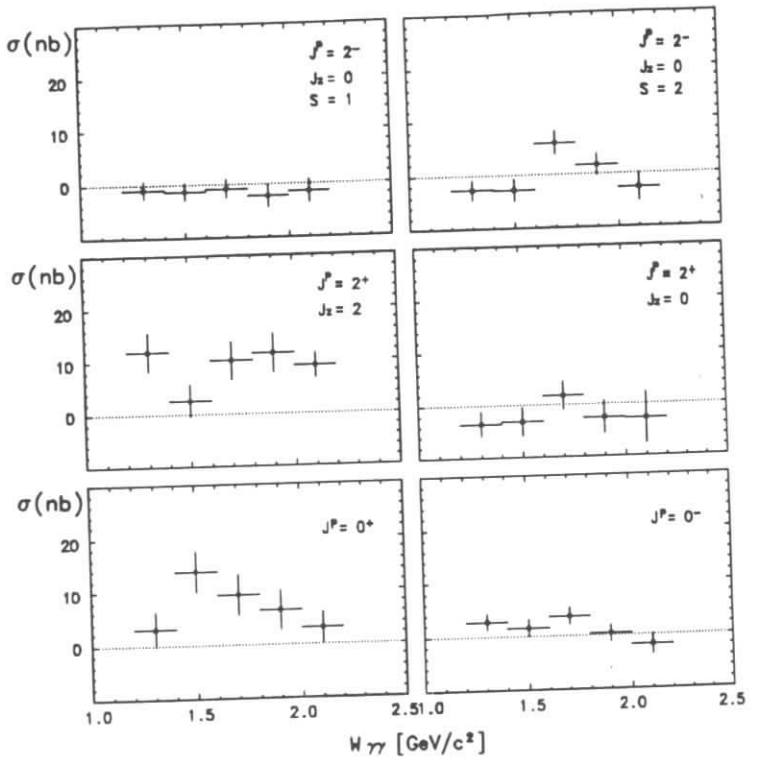

Figure 4.19: Cross sections for the reaction $\gamma\gamma \to \rho^+\rho^-$ for different J^P hypotheses.

14 nb at $W_{\gamma\gamma} \sim 1.5$ GeV/c^2 whereas the $J^P = 2^+$ helicity 2 about 11 nb at $W_{\gamma\gamma} \sim 1.8$ GeV/c^2. All the other amplitudes have negligible contribution.

As a test of consistency of the 3-parameter and the 8-parameter fit the cross sections for the reaction $\gamma\gamma \to \rho\pi\pi$ and $\gamma\gamma \to$ non-resonant $\pi^+\pi^-\pi^0\pi^0$ are compared in figure 4.20. In both cases the agreement is excellent. Since only the $J^P = 0^+$ and $J^P = 2^+$, $J_z = 2$ are the dominant contributions an attempt was made to fit with only four parameters. The result is summarized in Table 4.4.

4.5 Maximum Likelihood Tests

The maximum likelihood technique was tested extensively on Monte Carlo generated events. Different admixtures of the various J^P states were subjected to the same fitting procedure as the data. In all cases the fitting procedure was able to reproduce the input fractions of the different J^P states very well. An example is shown in figure 4.21. In figure 4.22 the same number of events was used as the one given by the four parameter fit and was fitted with all the 8 parameters. The fit procedure can reproduce the input very well.

Also a check of possible migration between different J^P states was performed. For this purpose only one state was used as input whereas the full 8-parameter fit was applied. Figures (4.23,4.24,4.25) show the results for $J^P = 0^+$ and $2^+(J_z = 2)$ which dominate the data, as well as the $J^P = 0^-$ amplitude. In all the cases the generated amplitude was properly identified by the fit. From these tests the systematic uncertainty of the likelihood method was estimated to be less than 10%.

The over all systematic uncertainty in the measured cross sections is estimated to be $\pm 16.9\%$ for all the reactions. It is composed of the contributions from event generation and detector simulation ($\pm 11\%$), experimental luminosity

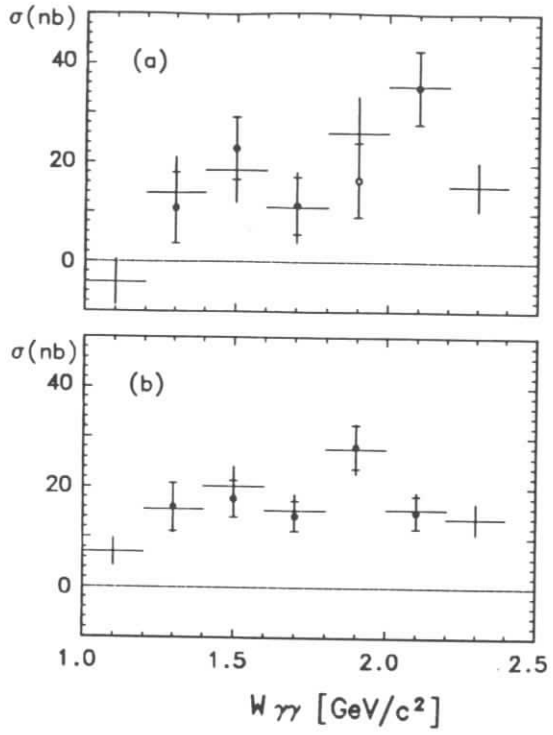

Figure 4.20: Comparison of the cross section found with the 8-parameter fit to the one found with the 3-parameter fit.

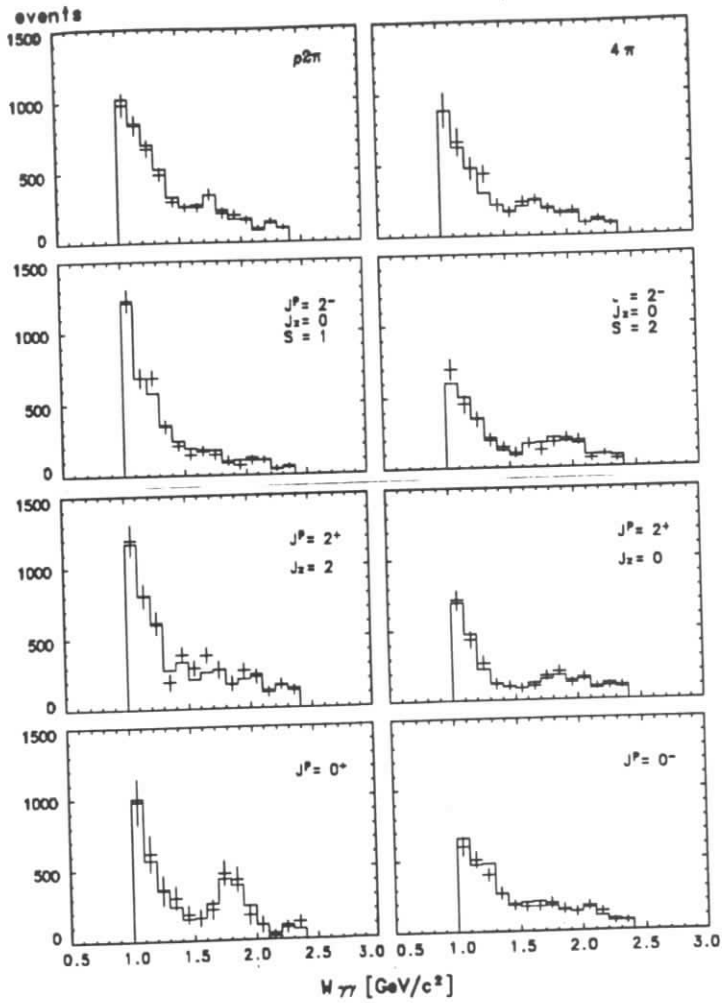

Figure 4.21: Consistency check of input and output from maximum likelihood fit. The input corresponds to Monte Carlo sample containing all the different spin-parity assignments and is presented as full histogram. The output is the presented with crosses and is the number of events found with the full 8 parameter fit.

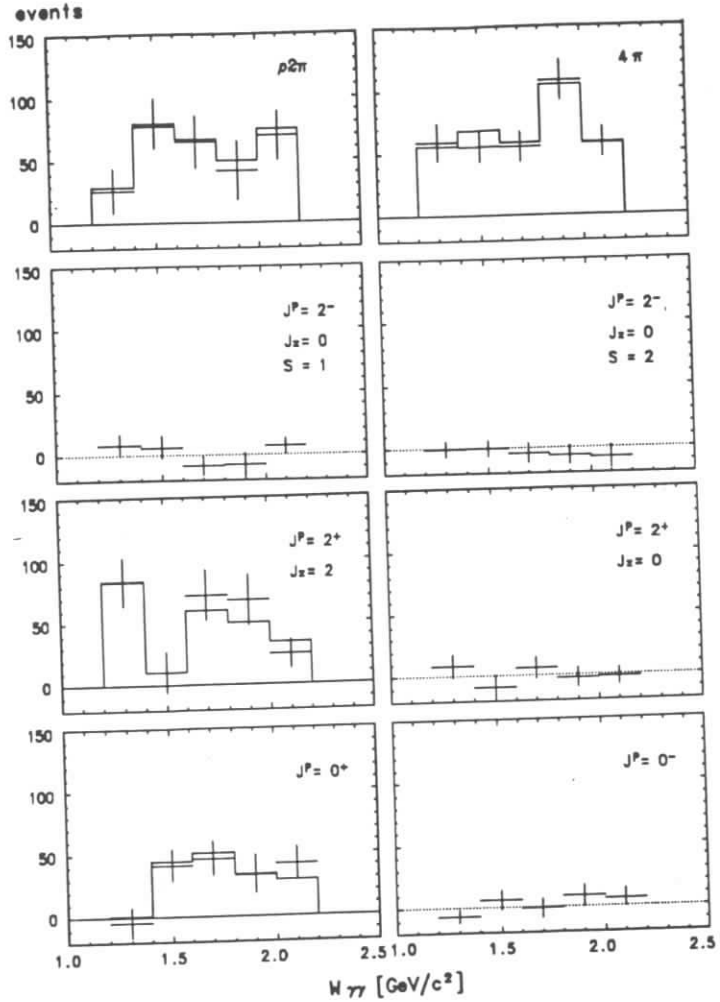

Figure 4.22: Consistency check of input and output from maximum likelihood fit. The input corresponds to Monte Carlo sample containing all the different spin-parity assignments as they were derived from the 4-parameter fit in the data and is presented as full histogram. The output is the presented with crosses and is the number of events found with the full 8 parameter fit.

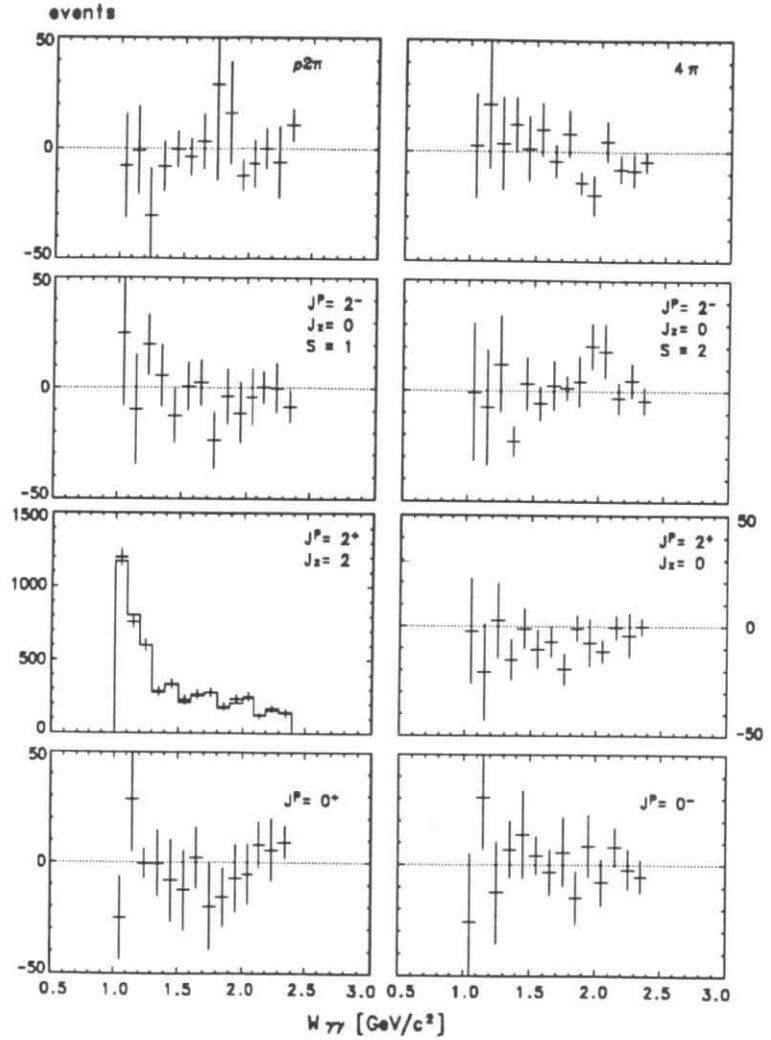

Figure 4.23: Consistency check of input and output from maximum likelihood fit. The input corresponds to Monte Carlo sample with only $J^P = 2^+$, $J_z = 2$ events and is presented as full histogram. The output is the presented with crosses and is the number of events found with the full 8 parameter fit.

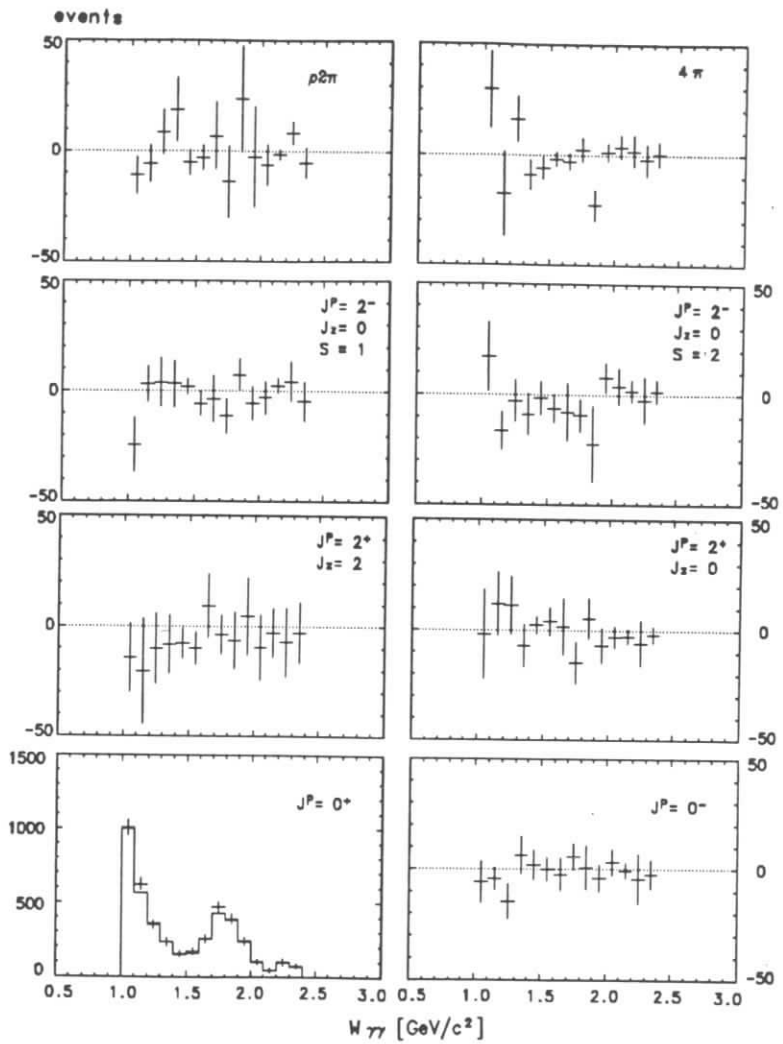

Figure 4.24: Consistency check of input and output from maximum likelihood fit. The input corresponds to Monte Carlo sample with only $J^P = 0^+$ events and is presented as full histogram. The output is the presented with crosses and is the number of events found with the full 8 parameter fit.

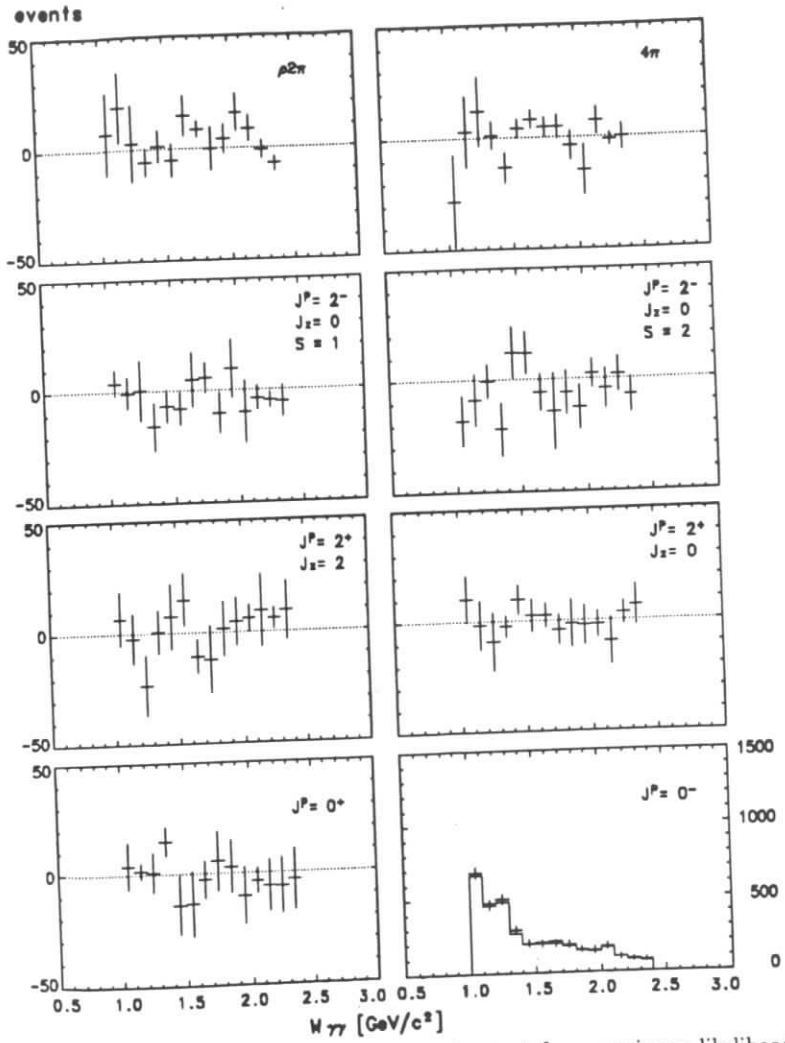

Figure 4.25: Consistency check of input and output from maximum likelihood fit. The input corresponds to Monte Carlo sample with only $J^P = 0^-$ events and is presented as full histogram. The output is the presented with crosses and is the number of events found with the full 8 parameter fit.

(±3%), trigger simulation (±5.5%), background estimation (±5%), and uncertainty from the maximum likelihood technique (±10%).

Another test was made by comparing the projections of the variables ξ, as well as the angles between the charged pions, for data and Monte Carlo. For the Monte Carlo distributions the fractions derived by the fit were used. Note that these projections do not include all the information for the correlation between the different parameters ξ since they are projections of the seven-dimensional space that these parameters represent and most of the information is integrated out. Examples of these projections are given in figure 4.26. (a) represents the polar angle of the ρ with respect to the $\gamma\gamma$ center of mass system, (b) the polar angle of the pions with respect to the ρ center of mass system. Both these angles enter in the construction of the likelihood function. (c) represents the angle between the two charged pions. The momenta of the charged pions are expressed at the center of mass system of the ρ-mesons they belong. The expectations of the different spin parity states, as well as the Monte Carlo expectations obtaines by using the fractions given by the fit, are also shown in figure 4.26.

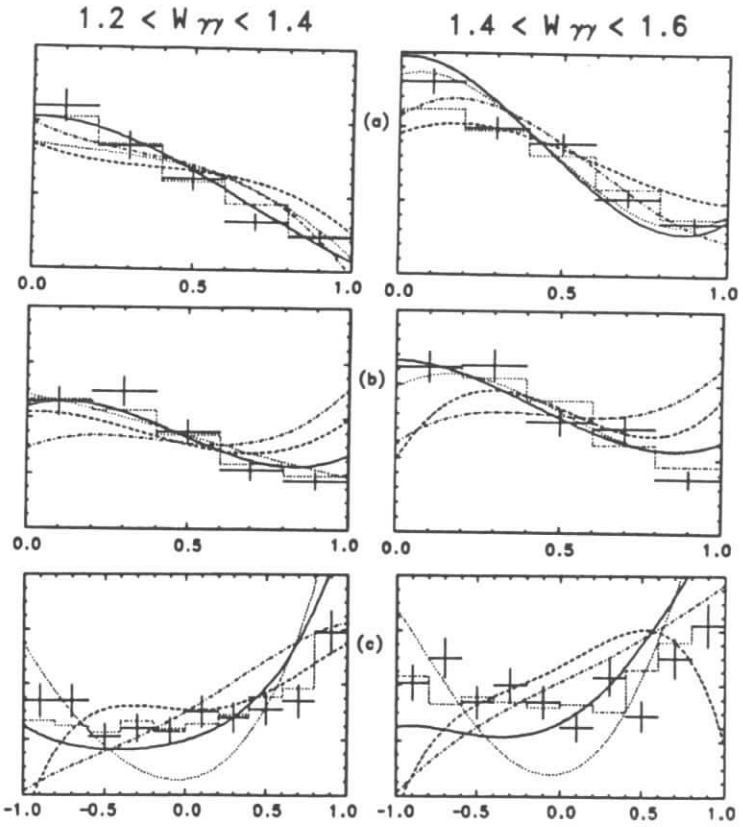

Figure 4.26: Comparison of the one dimensional projections between Data (crosses) and Monte Carlo expectations (histogram). The Monte Carlo expectations were derived by using the fractions given by the fit. The curves show the expectations for different spin parity states, 2^+ (full line), 0^+ (dotted line), 0^- (dashed line) and 2^- (dash-dotted line). The first column corresponds to $1.2 < W_{\gamma\gamma} < 1.4\ GeV/c^2$ and the second to $1.4 < W_{\gamma\gamma} < 1.6\ GeV/c^2$. a) the polar angle of the ρ with respect to $\gamma\gamma$ center of mass system, b) polar angle of the pions with respect to the ρ center of mass system c) the angle between the two charged pions.

Chapter 5

Discussion of the Experimental Results

5.1 Introduction

In chapters 3 and 4 the analysis of the reactions $\gamma\gamma \to 2\pi^+2\pi^-2\pi^0$ and $\gamma\gamma \to \pi^+\pi^-\pi^0\pi^0$ was described. In this chapter the experimental results will be discussed in the framework of the theoretical models presented in the first chapter and will also be compared to the existing upper limits and related measurements. The experimental results can be summarized for $\gamma\gamma \to 2\pi^+2\pi^-2\pi^0$ as follows:

- The topological cross section for the reaction $\gamma\gamma \to 2\pi^+2\pi^-2\pi^0$ does not show any significant structure and reaches a maximum of about 40 nb at $W_{\gamma\gamma}$ around 2.4 GeV/c^2. There are no theoretical calculations for comparison.
- The production of ω-mesons was observed in the $2\pi^+2\pi^-2\pi^0$ final state.
- The production of correlated ω-mesons was found and the reaction $\gamma\gamma \to \omega\omega$ was observed for $W_{\gamma\gamma} < 2\ GeV/c^2$. The cross section was measured to have a peak value of about 12 nb at $W_{\gamma\gamma}$ around 1.9 GeV/c^2.

- The production of events with only one ω-meson was also found, with a cross section reaching 20 nb at $W_{\gamma\gamma}$ around 2.3 GeV/c^2.

And for the $\pi^+\pi^-\pi^0\pi^0$ final state

- The topological cross section for the reaction $\gamma\gamma \to \pi^+\pi^-\pi^0\pi^0$ was found to rise steeply to about 70 nb for $W_{\gamma\gamma}$ above 1.2 GeV/c^2. Again there are no theoretical calculations to compare the measured cross section.

- The final state was decomposed in the $\rho^+\rho^-$, $\rho\pi\pi$ and non-resonant $\pi^+\pi^-\pi^0\pi^0$ contributions and the corresponding cross sections were derived.

- The $\gamma\gamma \to \rho^+\rho^-$ cross section was found to be suppressed relative to that for $\gamma\gamma \to \rho^0\rho^0$.

- A spin parity analysis of the $\rho^+\rho^-$ cross section showed that it is dominated by $J^P = 0^+$ and $J^P = 2^+$ with helicity 2.

5.2 Comparison to Model Predictions

The measured cross section for the reaction $\gamma\gamma \to \omega\omega$ is below the existing upper limits of PLUTO [28]. In figure 5.1 the measured cross section is compared to the theoretical expectations. The prediction from a t-channel factorization model [16] is shown as the shaded area. Clearly the t-channel factorization model fails to describe the data. The expectations from the four-quark model [20] are also shown in figure 5.1. The $q\bar{q}q\bar{q}$ model predicts that the two cryptoexotic isotensors $C(\mathbf{36}, \mathbf{2^+})$ and $C(\mathbf{9}, \mathbf{2^+})$ contribute to the cross section for the reaction $\gamma\gamma \to \omega\omega$. These states contribute also to the $\gamma\gamma \to \rho\rho$ cross section. Using the values found from a fit to the $\rho^0\rho^0$ cross section for the masses

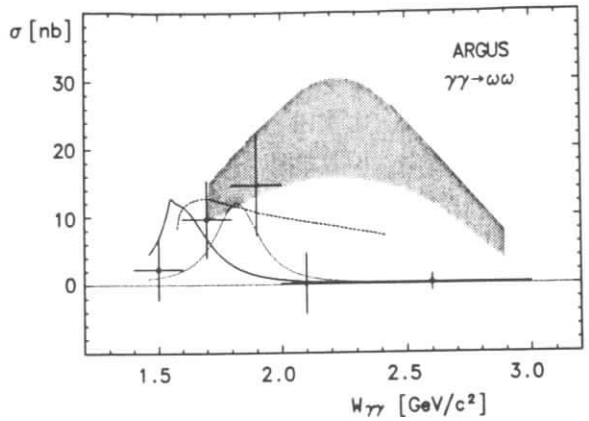

Figure 5.1: Comparison of the $\gamma\gamma \to \omega\omega$ measured cross section with the theoretical expectations. The shaded area represents the t-channel factorization model expectations, the solid line and dotted lines the $q\bar{q}q\bar{q}$ calculation for m=1.65 GeV/c^2, a=0.5 and m=1.8 GeV/c^2, a=0 and the dashed line the one pion contribution (OPE).

of these states and the free parameter a of the model (m=1.65 GeV/c^2, a=0.5), the model fails to describe the measured cross section (figure 5.1, solid line). It should be noted here that the value of 1.65 GeV/c^2 was used by the authors in their early calculations. In the later one a mass of 1.4 GeV/c^2 was used to fit the $\rho^0\rho^0$ cross section data, but this value is totally out of question in the case of the $\omega\omega$ cross section. However, using mass of 1.8 GeV/c^2 and a=0 a better fit to the data is obtained (figure 5.1, dotted line).

After the data were first shown in public Achasov *et al.* presented a calculation for the cross section of the reaction $\gamma\gamma \to \omega\omega$ using one-pion-exchange (OPE) . This calculation can explain in some qualitative way the measured

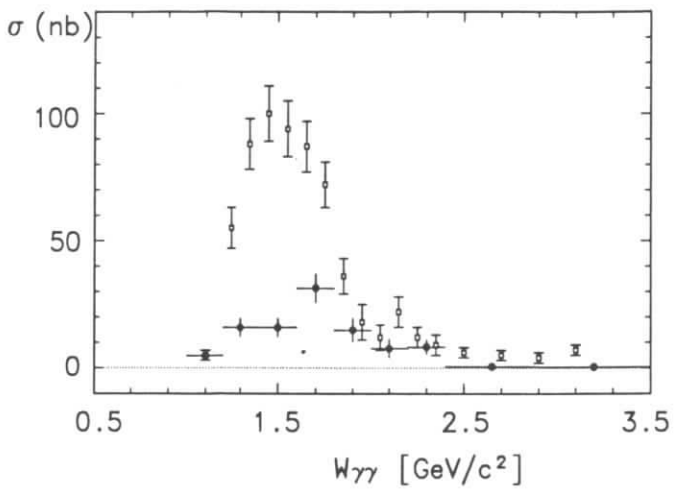

Figure 5.2: Comparison of the $\gamma\gamma \to \rho\rho$ measured cross sections. The reaction $\gamma\gamma \to \rho^0\rho^0$ is presented as squares and is the measurement by PLUTO [11] and the reaction $\gamma\gamma \to \rho^+\rho^-$ as full dots.

cross section and is also shown in figure 5.1 as dashed line. Still, it fails to describe the data. Unfortunately, with the existing statistics it is not possible to determine any spin parity of the $\omega\omega$ production. An attempt was made to make a spin parity analysis but the result was rather inconclusive due to the low statistics.

The measured cross section for the reaction $\gamma\gamma \to \rho^+\rho^-$ is about a factor 4 lower than the cross section for the reaction $\gamma\gamma \to \rho^0\rho^0$ as it can be seen in figure 5.2. In figure 5.3 a comparison of the $\gamma\gamma \to \rho^+\rho^-$ cross section assuming isotropic production of the $\rho^+\rho^-$ system to the theoretical calculations is given. The expectation of the t-channel factorization model is shown in figure 5.3 as the shaded area. The data do not favour this model at all. Using a QCD

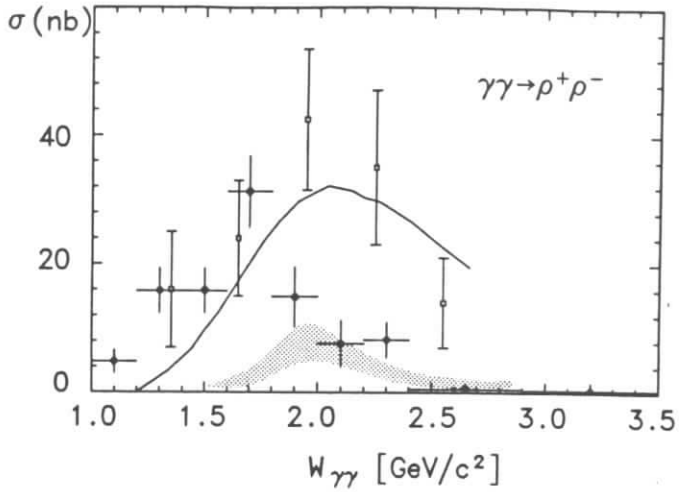

Figure 5.3: Comparison of the measured cross section for $\gamma\gamma \to \rho^+\rho^-$ assuming isotropic production of the $\rho^+\rho^-$ system (3-parameter fit, full dots) with the upper limits given by JADE [13] (squares), the QCD calculation by Brodsky *et al.* [48] and the t-channel factorization model predictions (shaded area) [16].

approach, the $\rho^+\rho^-$ cross section was calculated by Brodsky *et al.* [48] (shown as full line in figure 5.3) but, again, the model does not describe the data.

A comparison of the $\rho^+\rho^-$ cross section derived from the spin-parity analysis with the cross section for $\rho^0\rho^0$ measured by TASSO [8, (1982)] is given in figure 5.4. The $J^P = 0^+$ amplitude is about a factor 4 lower in the $\rho^+\rho^-$ than that of the $\rho^0\rho^0$ and for the $J^P = 2^+$ $J_z = 2$ about a factor 2.

In the framework of the four quark model by Achasov *et al.* [20] $\rho^+\rho^-$ production proceeds through destructive interference of the exotic isoscalar resonance, $E(\mathbf{36}, \mathbf{2^+})$, and the two cryptoexotic isotensors, $C(\mathbf{36}, \mathbf{2^+})$ and $C(\mathbf{9}, \mathbf{2^+})$. These states are expected to have mass 1.4 GeV/c^2. The parameter a from equation 1.29 was set to a=0.5 from fit to the $\rho^0\rho^0$ cross section. In addition the

authors [20] expect contribution from the $f(1270)$ while contribution from the $J^P = 0^+$ $q\bar{q}q\bar{q}$ states is negligible. The model presented by Li and Liu has in addition to the $J^P = 2^+$ states listed above, sizeable contribution from the $J^P = 0^+$ $C(\mathbf{36^*}, \mathbf{0^+})$, $E(\mathbf{36^*}, \mathbf{0^+})$ and $C(\mathbf{9^*}, \mathbf{0^+})$ states. The masses in this model were set to 1.7 and 1.45 GeV/c^2 for the 2^+ and 0^+ states respectively by fitting again the $\rho^0\rho^0$ cross section. The comparison of the data to the $q\bar{q}q\bar{q}$ models is shown in figure 5.5. It is clear that the model expectations fail in describing the data.

5.3 Conclusions

In conclusion, the reactions $\gamma\gamma \to 2\pi^+2\pi^-2\pi^0$ and $\gamma\gamma \to \pi^+\pi^-\pi^0\pi^0$ were studied. The reactions $\gamma\gamma \to \omega\omega$ and $\gamma\gamma \to \rho^+\rho^-$ were observed for the first time and their cross section was measured. The $\gamma\gamma \to \omega\omega$ cross section shows an enhancement around $W_{\gamma\gamma} \sim 1.9\ GeV/c^2$. The $\gamma\gamma \to \rho^+\rho^-$ cross section does not show threshold enhancement similar to the one for $\gamma\gamma \to \rho^0\rho^0$. It was also found that it is dominated by two amplitudes, $J^P = 0^+$ and $J^P = 2^+$ helicity $J_z = 2$. The existing models fail to describe the measured cross sections. Similar problems were also found in the other ARGUS measurements on the vector pair meson production in two photon interactions.

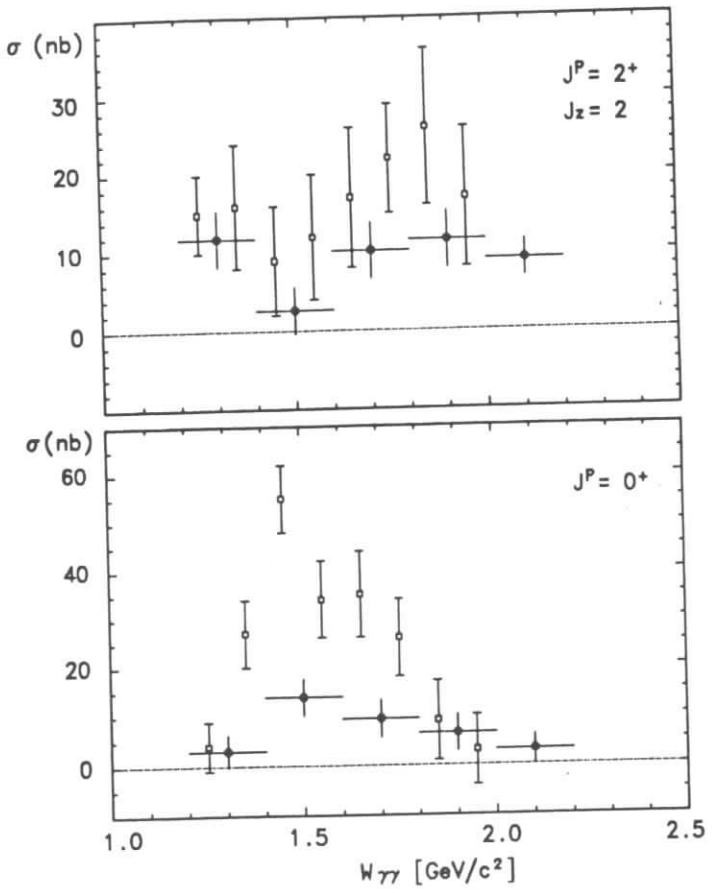

Figure 5.4: Comparison of the measured cross section for $\gamma\gamma \to \rho^+\rho^-$ (full dots) for $J^P = 2^+$, $J_z = 2$ and $J^P = 0^+$ with the measurement by TASSO [8,(1982)] (squares) for $\gamma\gamma \to \rho^0\rho^0$.

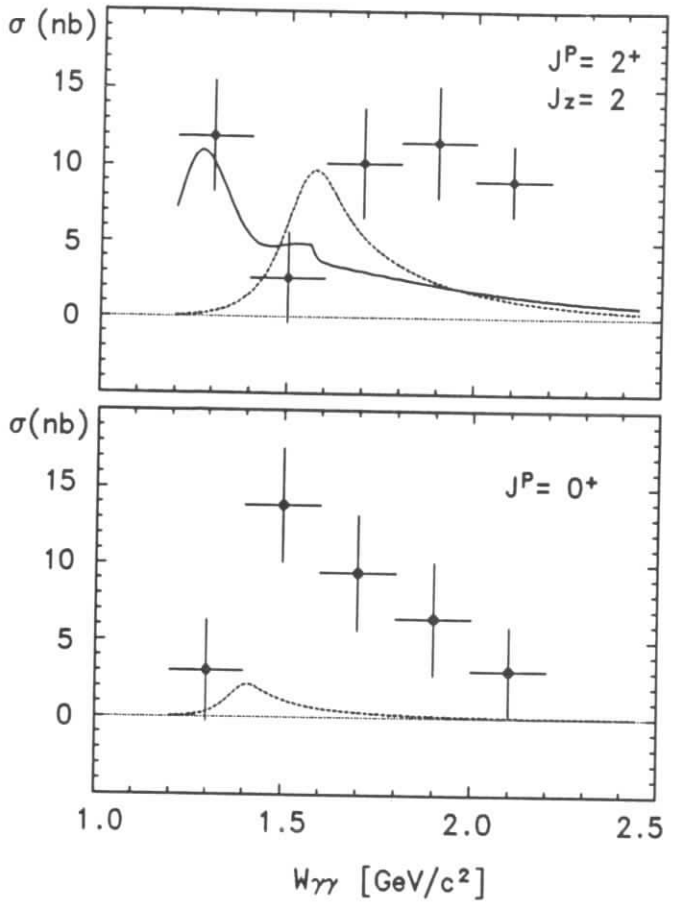

Figure 5.5: Comparison of the measured cross section for $\gamma\gamma \to \rho^+\rho^-$ for $J^P = 2^+$, $J_z = 2$ and $J^P = 0^+$ with the $q\bar{q}q\bar{q}$ model predictions. Full line by Achasov *et al.* [20] and dashed line by Li and Liu [21].

Appendix A

The Landau-Yang Theorem

Let us assume that a photon is travelling along the positive z axis with momentum k and helicity λ ($\mid k, \lambda >$). Following Yang's arguments [7] we consider transformations under $\mathbf{R}_\phi, \mathbf{R}_\mathbf{x}$ and $\mathbf{P}$, where the symbols stand for rotation around the z-axis by an angle ϕ, rotation around the x-axis by 180° and the parity transformation respectively. Therefore

$$\begin{aligned} \mathbf{R}_\phi \mid k, \lambda > &= e^{-i\lambda\phi} \mid k, \lambda > \\ \mathbf{R}_\mathbf{x} \mid k, \lambda > &= \mid -k, \lambda > \\ \mathbf{P} \mid k, \lambda > &= \mid -k, -\lambda > \end{aligned} \tag{A.1}$$

A two photon state in the rest system of a resonance is given by

$$\mid k, \lambda_1 > \mid k, \lambda_2 >$$

where the λ_i can take the values ± 1 for real photons. If we choose as basis for the four possible states

$$\psi_1 = \frac{1}{\sqrt{2}} \{ \mid k, + > \mid -k, + > + \mid k, - > \mid -k, - > \} \tag{A.2}$$

$$\psi_2 = \frac{1}{\sqrt{2}} \{ \mid k, + > \mid -k, + > - \mid k, - > \mid -k, - > \} \tag{A.3}$$

$$\psi_3 = \mid k, + > \mid -k, - > \tag{A.4}$$

$$\psi_4 = \mid k, - > \mid -k, + > \tag{A.5}$$

These states are eigenstates under $\mathbf{R}_\phi$ and $\mathbf{P}$, and ψ_1 and ψ_2 are also eigenstates under $\mathbf{R}_\mathbf{x}$. The assignment for the total helicity is $\lambda = \lambda_1 - \lambda_2 = 0$ or 2.

	ψ_1	ψ_2	ψ_3	ψ_4
$\mathbf{R}_\phi$	1	1	$e^{2i\phi}$	$e^{-2i\phi}$
$\mathbf{R}_\mathbf{x}$	1	1	-	-
$\mathbf{P}$	1	-1	1	1
λ	0	0	2	2

Table A.1: The eigenvalues of two photon states under the transformations $\mathbf{R}_\phi$, $\mathbf{R}_\mathbf{x}$ and $\mathbf{P}$.

The eigenvalues of the above states under the transformations A.1 are given in table A.1.

From the λ values and the behaviour under $\mathbf{R}_\phi$, the resonance is allowed to have $J \geq 0$ for ψ_1 and ψ_2 and $J \geq 2$ for ψ_3 and ψ_4. For $J = 1$, ψ_1, ψ_2 are even under R_x, whereas the wave function $Y_{1,0}$ of a spin 1 resonance is odd under the same transformation. Therefore $J = 1$ is not allowed for any two photon state. Note that the helicity λ=2 occurs only for even parity transformations and is therefore allowed only for $J^{PC} = 2^{++}$.

Appendix B

The ρ-meson Decay Matrix Element

The ρ-meson has $J^P = 1^-$ and decays into two π-mesons. The two π-mesons contribute a factor +1 to the total parity of the system. Therefore the spatial properties of the ρ-meson decay matrix element must correspond to $J^P = 1^-$ (i.e. it must be proportional to a vector). Since the ρ-meson is at rest, there is only one independent vector available. In the case of $\rho^\pm \rightarrow \pi^\pm\pi^0$, it is convenient to choose the momentum $\vec{p}_\pi$ of the charged pion. Then the matrix element for the ρ can be written as :

$$\mathcal{M}(\rho) = constant \cdot \vec{p}_\pi \tag{B.1}$$

The different spin states of the ρ are projected out by the ρ polarization vector. Using the helicity basis, the polarization vector can be constructed from the basis vectors

$$\vec{\epsilon}_+ = \begin{pmatrix} 1 \\ i \\ 0 \end{pmatrix} \quad \vec{\epsilon}_- = \begin{pmatrix} 1 \\ -i \\ 0 \end{pmatrix} \quad \vec{\epsilon}_0 = \begin{pmatrix} 0 \\ 0 \\ 1 \end{pmatrix} \tag{B.2}$$

In polar coordinates the $\vec{p}_\pi$ can be written as:

$$\vec{p}_\pi = \mid \vec{p}_\pi \mid \cdot \begin{pmatrix} sin\theta_\pi cos\phi_\pi \\ sin\theta_\pi sin\phi_\pi \\ cos\theta_\pi \end{pmatrix} \tag{B.3}$$

Then the matrix elements for the decay of a ρ-meson with spin components $s_z = 0, \pm 1$ is

$$\begin{aligned} \mathcal{M}_+(\rho) \sim \vec{p}_\pi \cdot \vec{e}_+ &= \mid \vec{p}_\pi \mid \cdot \sin\theta_\pi (\cos\phi_\pi + i \sin\phi_\pi) \\ \mathcal{M}_-(\rho) \sim \vec{p}_\pi \cdot \vec{e}_- &= \mid \vec{p}_\pi \mid \cdot \sin\theta_\pi (\cos\phi_\pi - i \sin\phi_\pi) \\ \mathcal{M}_0(\rho) \sim \vec{p}_\pi \cdot \vec{e}_0 &= \mid \vec{p}_\pi \mid \cdot (\cos\theta_\pi) \end{aligned} \tag{B.4}$$

which can be rewritten in terms of spherical harmonics as:

$$\begin{aligned} \mathcal{M}_+(\rho) &\sim \mid \vec{p}_\pi \mid \cdot Y_1^1(\theta_\pi \phi_\pi) \\ \mathcal{M}_-(\rho) &\sim \mid \vec{p}_\pi \mid \cdot Y_1^{-1}(\theta_\pi \phi_\pi) \\ \mathcal{M}_0(\rho) &\sim \mid \vec{p}_\pi \mid \cdot Y_1^0(\theta_\pi \phi_\pi) \end{aligned} \tag{B.5}$$

Appendix C

Trigger Simulation - User Routines

In the following the subroutines that allow the user to supply his instructions to the trigger simulation program are briefly described for the sake of completeness, and for use by members of the collaboration. All these subroutines can be found on the DESY IBM in a library under the name 'F15YOR.TRIGGER.USER'. The user can supply his requirements to the trigger simulation program through the subroutines UASIGN, UCUTRN, UCUTTR, UENG.

UASIGN allows the user to normalize and mix different Monte Carlo data sets and in this way to simulate different periods (eg. runs with or without VDC)

UCUTRN allows the user to make the data quality cuts he used in the analysis of the real data. This is essential for the trigger program in order to calculate the luminosity of each trigger period.

UCUTTR can be used to make cuts on the trigger logic. For example it can ask the program to simulate only the trigger periods with a minimum LTF threshold excluding the HESH trigger.

UENG the user can make energy dependent corrections. For example in two photon interactions a correction is applied for the energy dependence of the two photon luminosity.

Appendix D

The ARGUS Collaboration

H. Albrecht, R. Gläser, G. Harder, A. Krüger, A. Nippe, T. Oest, M. Reidenbach, M. Schäfer, W. Schmidt-Parzefall, H. Schröder, H. D. Schulz, F. Sefkow, R. Wurth

DESY, Hamburg, Germany

R. D.Appuhn, A. Drescher, C. Hast, G. Herrera, H. Kolanoski, A. Lange, A. Lindner, R. Mankel, H. Scheck, G. Schweda, B. Spaan, A. Walther, D. Wegener

Institut für Physik, Universität Dortmund, Germany

M. Paulini, K. Reim, U. Volland, H. Wegener

Physikalisches Institut, Universität Erlangen-Nürnberg, Germany

W. Funk, J. Stiewe, S. Werner

Institut für Hochenergiephysik, Universität Heidelberg, Germany

S. Ball, J. C. Gabriel, C. Geyer, A. Hölscher, W. Hofmann, B. Holzer, S. Khan, J. Spengler

Max-Planck-Institut für Kernphysik, Heidelberg, Germany

C. E. K. Charlesworth[1], K. W. Edwards[2], W. R. Frisken[3], H. Kapitza[2], P. Krieger[1], R. Kutschke[1], D. B. MacFarlane[4], K. W. McLean[4], A. W. Nilsson[4], R. S. Orr[1], J. A. Parsons[1], P. M. Patel[4], J. D. Prentice[1], S. C. Seidel[1], J. D. Swain[1], G. Tsipolitis[4], K. Tzamariudaki[4], T.-S. Yoon[1]
Institute of Particle Physics, Canada

R. Davis
University of Kansas, Lawrence, KS, USA

T. Ruf, S. Schael, K. R. Schubert, K. Strahl, R. Waldi, S. Weseler
Institut für Experimentelle Kernphysik, Universität Karlsruhe, Germany

B. Boštjančič, G. Kernel, P. Križan, E. Križnič, M. Pleško
Institut J. Stefan and Oddelek za fiziko, Univerza v Ljubljani, Ljubljana, Yugoslavia

H. I. Cronström, L. Jönsson
Institute of Physics, University of Lund, Sweden

A. Babaev, M. Danilov, B. Fominykh, A. Golutvin, I. Gorelov, V. Lubimov, A. Rostovtsev, A. Semenov, S. Semenov, V. Shevchenko, V. Soloshenko, V. Tchistilin, I. Tichomirov, Yu. Zaitsev
Institute of Theoretical and Experimental Physics, Moscow, USSR

R. Childers, C. W. Darden
University of South Carolina, Columbia, SC, USA

[1]University of Toronto, Toronto, Ontario, Canada.
[2]Carleton University, Ottawa, Ontario, Canada.
[3]York University, Downsview, Ontario, Canada.
[4]McGill University, Montreal, Quebec, Canada.

Appendix E

The Author's Personal Contribution to the ARGUS Experiment

I have been an active member of the ARGUS experiment since the fall 1986. I spent two years in Hamburg. During my stay in Hamburg I, like all collaboration members, worked shifts while data was being taken in the experiment. Running shifts requires those present to monitor and record all aspects of the detector performance and to correct problems as they occur.

In addition, I had the responsibility for two-photon Monte Carlo program which was used for the two photon results and for the τ-lepton results for background studies. The ARGUS Trigger simulation program was also under my responsibility. This is a very useful tool for studies with low multiplicity events, like two photon interaction and the τ-lepton studies, where accurate knowledge of the trigger efficiencies is needed. I was also responsible for the selection of two prong events from the original ARGUS data sets.

The experiment is sited at DESY and all the analysis is done with the IBM. However, many of the collaborating institutions have VAX computers and the software has to be converted from IBM format to VAX format. I developed the code to transfer the ARGUS runfile to the VAX.

During the last one and a half years, spent at McGill, I installed KAL and I made the KAL-GEP interface working on the VAX. KAL, the Kinematical Analysis Language program, is used extensively in the analysis. I kept it up to date, matching the latest version used in Hamburg on the IBM.

I also participated in the electrostatic tests and the cathode plane stabilization problem of the new micro-vertex chamber which will be installed in ARGUS by the end of this year. This was valuable for boosting my hardware experience.

My contributions to the physics analysis are the first observations of the reactions $\gamma\gamma \to \omega\omega$ and $\gamma\gamma \to \rho^+\rho^-$ which are described in this thesis. In addition, I was actively involved in all the vector meson pair production in two photon interactions analyses published by ARGUS.

Bibliography

[1] F. Low, Phys.Rev. **120**(1960)582.

[2] F. Calogero and C. Zemach, Phys.Rev. **120**(1960)1860.

[3] H. Kolanoski,"*Two-Photon Physics at e^+e^- Storage Rings*", Springer Tracts in Modern Physics, **105**(1984);
M. Poppe,"*Exclusive Hadron Production in Two-Photon Reactions*", International Journal of Modern Physics **A1**(1986)545;
Ch. Berger and W. Wagner, "*Photon Photon Reactions*, Phys.Rep. **146**(1987)1;
S. Cooper, "*Meson Production in Two-Photon Collisions*", Annual Reviews of Nuclear and Particle Science **38**(1988)705-749;
H. Kolanoski and P. Zerwas, "*Two-Photon Physics*", Advanced Series on Directions in High Energy Physics, Vol. 1, ed. A. Ali and P. Söding. World Scientific.

[4] G. Bonneau, M. Gourdin and F. Martin, Nuc.Phys. **B54**(1973)573.

[5] V.M. Budnev, I.F. Ginzburg, G.V. Meledin and V.G. Serbo, Phys.Rep. **15**(1975)181-282.

[6] J.H. Field, Nuc.Phys. **B168**(1980)477 and Nuc.Phys. **B176**(1980)545 Erratum.

[7] L.D. Landau, Soviet Physics *Doclady* **60**(1948)207 ;
C.N. Yang, Phys.Rev. **77**(1950)242.

[8] (TASSO) R. Brandelik *et al.*, Phys. Lett. **97B** (1980) 448 ;
(TASSO) M. Althoff *et al.*, Z. Phys. **C16** (1982) 13.

[9] (MARK II) D.L. Burke *et al.*, Phys. Lett. **103B** (1981) 153.

[10] (CELLO) H.-J. Behrend *et al.*, Z. Phys. **C21** (1984) 205.

[11] (PLUTO) Ch. Berger *et al.*, Z.Phys.**C37**(1988)329.

[12] (TPC/Two-Gamma) H. Aihara *et al.*, Phys. Rev. **D37**(1988)28.

[13] (JADE) in Proc. of the 5th Int. Workshop on $\gamma\gamma$ Collisions, Aachen (1983) 175, ed. Ch. Berger, presented by H. Kolanoski.

[14] J.J. Sakurai, Ann.Phys. **11**(1960)1;
J.J. Sakurai, Phys.Rev.Lett **22**(1969)981;
J.J. Sakurai and D. Schildknecht, Phys.Lett.**40B**(1972)121

[15] W. Wagner, " Photon Photon Interactions", Habilitationsschrift, Aachen preprint PITHA 83/03 (1983)

[16] G. Alexander, U. Maor and P.G. Williams, Phys.Rev.**D26**(1982)1198;
G. Alexander, A. Levy and U. Maor, Z.Phys.**C30**(1986)65.

[17] H. Kolanoski, Z.Phys.**C39**(1988)543.

[18] R.J. Jaffe, "*Multiquark Hadrons. I. Phenomenology of $Q^2\overline{Q^2}$ Mesons*", Phys.Rev.**D15**(1977)267;
R.J. Jaffe, "*Multiquark Hadrons. II. Methods*", Phys.Rev.**D15**(1977)281.

[19] F.E. Close, "*An Introduction to Quarks and Partons*", Academic Press 1979.

[20] N.N. Achasov, S. A. Devyanin, and G. N. Shestakov, Phys. Lett. **108B**(1982)134;
N.N. Achasov, S. A. Devyanin, and G. N. Shestakov, Z. Phys. **C16**(1982)55;
N.N. Achasov, S. A. Devyanin, and G. N. Shestakov, JETP Lett **40**(1984)1173;
N.N. Achasov, S. A. Devyanin, and G. N. Shestakov, Z. Phys. **C27**(1985)99.

[21] B.A. Li and K.F. Liu, Phys. Lett. **118B**(1982)435 and **124B**(1983)550 (Erratum);
B.A. Li and K.F. Liu, Phys. Rev. Lett.**51**(1983)1510;
B.A. Li and K.F. Liu, Phys. Rev. **D30**(1984)613;
B.A. Li, "*Production of $Q^2\overline{Q}^2$ States*", SLAC-PUB-5007(June 1989).

[22] R.J. Jaffe and K. Johnson, Phys.lett. **60B**(1976)201.

[23] M.S. Chanowitz, "*Resonances in Photon Photon Scattering*", Proceedings of the VIth International Workshop on Photon-Photon Collisions, Lake Tahoe 1984, ed. R. Lander;
M.S. Chanowitz "*Progress Toward Identification of Gluonic States*", Proceedings of the Second International Conference on Hadron Spectroscopy, KEK report 87-7 (1987);
M.S. Chanowitz, "*Resonances in Photon-Photon Scattering*", preprint LBL-25433 (1988).

[24] (MARK III) D.L. Burke *et al.*, Phys.Rev.Lett. **49**(1982)632;
(MARK III) R.M. Baltrusaitis *et al.*, Phys.Rev. **D33**(1986)1222;

(DM2) D. Bisello *et al.*, "*First Observation of Three Pseudoscalar States in the $J/\Psi \to \gamma\rho\rho$ Decay*", Preprint LAL 88-12

[25] (MARK III) R.M. Baltrusaitis *et al.*, Phys.Rev.Lett. **55**(1985)1723;
(DM2) D. Bisello *et al.*, Phys.Lett. **192B**(1987)239.

[26] L. Köpke and N. Wermes, "*J/Ψ Decays*", CERN preprint CERN-EP/88-93 (1988)

[27] (TASSO) M. Althoff *et al.*, Z.Phys. **C32**(1986)11.

[28] (PLUTO) Ch. Berger *et al.*, Z.Phys. **C29**(1985)183.

[29] (ARGUS) H. Albrecht *et al.*, Phys.Lett. **196B** (1987) 101-106.

[30] (ARGUS) H. Albrecht *et al.*, Phys.Lett. **198B** (1987) 255-260.

[31] (ARGUS) H. Albrecht *et al.*, Phys.Lett. **210B** (1988) 273-277.

[32] (ARGUS) H. Albrecht *et al.*, Phys.Lett. **212B** (1988) 528-532.

[33] H. Nesemann, "*Status and Limitations of DORIS II*", Proceedings of the International Symposium on Production and Decay of Heavy Hadrons, Heidelberg 1986, ed. K.R. Schubert and R. Waldi.

[34] (ARGUS) H. Albrecht *et al.*, "*ARGUS : A Universal Detector at DORIS II*", Nucl.Inst.Methods **A275**(1989)1.

[35] H. Hasemann *et al.*, "*ARGUS, A New Detector for DORIS*", DESY Internal Report F15-Pro 148, October 1978.

[36] M. Danilov *et al.*, Nucl. Instr. Methods **217** (1983) 153;
M. Danilov *et al.*, "*Study of Drift Chamber Ageing with Propane*", preprint DESY 88-090.

[37] K.W. Edwards *et al.*, Nucl.Instr.Meth. **A252**(1986)384;
Jae-Chul Yun, "*A Vertex Chamber for ARGUS*", M. Sc. thesis, Carleton University, Ottawa, 1984.

[38] R. Heller *et al.*, Nucl. Instr. Methods **A235** (1985) 26;
R. Heller *et al.*, "*Test Measurements with the ARGUS Time-Of-Flight Counters*, Heidelberg preprint, IHEP-HD/ARGUS/81-02, unpublished.

[39] A. Drescher *et al.*, Nucl.Instr.Methods **205**(1983)125, **216**(1983)35, **237**(1985)464;
A. Drescher *et al.*, **A249**(1986)277.

[40] A. Arefiev *et al.*, DESY 83-025 and Instr.Exp.Tech.**29**(1986)333.

[41] H.D. Schulz and H.J. Stuckenberg, Proc.Topical Conference on the Application of Microprocessors in High Energy Physics Experiments, CERN, Geneva, Yellow report CERN 81-07.

[42] PDG, "*Review of Particle Properties*, Phys.Lett. **B204**(1988)1.

[43] H. Gennow, "*SIMARG*", DESY Internal Report F15-85-02, August 1985.

[44] R. Brun *et al.*, "*GEANT*", CERN-DD/78/2(1978).

[45] R. L. Ford and W. R. Nelson, "*The EGS Code System*", Version 3, SLAC-210,UC-32(1978).

[46] H. Fesefeldt, RWTH Aachen Report PITHA 85/02, 1985.

[47] J.D. Jackson, Nuovo Cimento **34**(1964)1644.

[48] S. J. Brodsky, G. Köpp and P. M. Zerwas, Phys.Rev.Lett.**58**(1987)443.